Ternary representation of contextual information along the CA1 transverse axis

Ya-Li Duan[1,3,4], Shu-Yi Hu[1,3,4], Xiao-Fan Ge[1,2], Jia-Li Long[1,3], Chu Deng[1,3], Yu-Ming Sun[1,3], Cheng-Ji Li[1,2], Rong Zhang[1,2], Xing Cai[1,2], Li Lu[1,2,5]

1. Key Laboratory of Genetic Evolution & Animal Models, and Key Laboratory of Animal Models & Human Disease Mechanisms of Yunnan Province, Kunming Institute of Zoology, Chinese Academy of Sciences, Kunming, Yunnan 650201, China

2. National Research Facility for Phenotypic & Genetic Analysis of Model Animals (Primate Facility), Kunming Institute of Zoology, Chinese Academy of Sciences, Kunming, Yunnan 650107, China

3. Kunming College of Life Science, University of Chinese Academy of Sciences, Kunming, Yunnan 650204, China

4. Equal contribution

5. Corresponding author

Abstract

The function of CA1 region in the rat hippocampus is transversely organized, aligning with input profiles from the entorhinal cortex and the CA3-CA2 region. We asked how CA1 neurons respond diversely to various contextual changes along the transverse axis, and how it may be influenced by selective inputs from upstream brain regions. Neuronal activity across the entire proximo-distal extent of CA1 in Long-Evans rats was monitored under manipulations of spatial or non-spatial environmental cues. Our results identified three distinct patterns of cue representation that varied from the proximal to the distal end of CA1: a descending gradient in spatial information processing, an ascending gradient in representation of local object features, and a reverse J-shaped pattern in response to non-spatial cue manipulation. This heterogeneity is closely linked to the nature of information altered in the environment, suggesting an involvement of upstream cue-selective neurons in shaping CA1 function.

Key words:

CA1, transverse axis, remapping, spatial context, non-spatial cues, object

Introduction

The hippocampus plays a pivotal role in spatial navigation and episodic memory. In rodents, the collective localized firing of hippocampal neurons, known as place cells, generates a cognitive map of the spatial environment and provides a framework for associating episodic memories (Sugar et al. 2019). The hippocampus in rodents creates distinct representations within populations of place cells to reflect changes in the animal's internal state or the external environment (Colgin et al. 2008). The place cell system employs discrete population codes to orthogonalize the pattern of activity in response to significant alterations in spatial context, known as global remapping. Conversely, it maintains the same population code for a given space but redistributes firing rates to distinguish non-spatial differences such as color, odor, and motivation, a process termed rate remapping (Latuske et al. 2017). The activity of place cells is modulated by inputs from surrounding brain regions (the para-hippocampal region), particularly the entorhinal cortex (EC), which interconnects with various cortical and subcortical regions, integrates incoming multimodal sensory information, and conveys highly processed signals to the hippocampus (Canto et al. 2008). The medial division of the entorhinal cortex (MEC) contains several specialized cell types, including grid cells (Hafting et al. 2005), aperiodic spatial cells (Fyhn et al. 2004), head direction cells (Sargolini et al. 2006), border cells (Solstad et al. 2008), and speed cells (Kropff et al. 2015), which together form a dynamic representation of the animal's location in space (Long et al. 2022, Tukker et al. 2022). In contrast, the lateral division of the entorhinal cortex (LEC) exhibits minimal spatial selectivity in open fields (Hargreaves et al. 2005, Huang et al. 2023). Most neurons in LEC represent non-spatial features of the animal's ongoing experience, such as object (Deshmukh et al. 2011, Tsao et al. 2013), odor (Igarashi et al. 2014, Leitner et al. 2016), time (Tsao et al. 2018), and animal’s egocentric position relative to landmarks (Wang et al. 2018), supplying the hippocampus with a temporal progression of events (Sugar et al. 2019). Spatial and non-spatial information is processed separately within the medial and lateral divisions of EC (Knierim et al. 2014), thus

potentially influencing the activity of hippocampal neurons in distinct pathways through MEC and LEC inputs.

The divergent information from EC converges at both early and later stages of the hippocampal circuit through different pathways. In dentate gyrus (DG), the distal portion of CA3 (dCA3, near CA2), and CA2, projections from layer II of MEC and LEC terminate on distinct dendritic segments of the same neuron. In CA1 and subiculum, medial and lateral fibers from layer III of EC predominantly terminate on separate cell populations at different positions along the transverse axis. MEC neurons preferentially project to the proximal portion of CA1 (pCA1), near CA2, and the distal part of subiculum, away from CA1, whereas LEC neurons primarily terminate their axons in the distal portion of CA1 (dCA1) and the adjacent proximal part of subiculum (Cappaert et al. 2015, Nilssen et al. 2019). Additionally, MEC axons innervate a greater number of neurons in the deep CA1 pyramidal cell layer, while LEC fibers predominantly excite superficial pyramidal neurons in CA1 (Masurkar et al. 2017). Within the hippocampus, mossy fiber inputs from DG decrease, and recurrent excitatory connections increase in parallel along the CA3-to-CA2 axis. The proximal portion of CA3 (pCA3, engulfed by DG) preferentially projects to dCA1, while dCA3/CA2 fibers primarily terminate at neighboring pCA1. Pyramidal neurons in pCA1 and dCA1, in turn, send their axons to the distal and proximal subiculum, respectively. Ultimately, CA1 and subiculum, as the major output regions of the hippocampus, send reciprocal projections to the deep layers of EC (Cappaert et al. 2015).

The distinct signals from medial and lateral divisions of EC (Knierim et al. 2014), in conjunction with the topographically organized intrinsic and extrinsic hippocampal connections (Cappaert et al. 2015), result in functional segregation along the proximo-distal axis within the hippocampus. Examinations of the expression pattern of immediate-early genes have identified sub-networks with distinct mnemonic functions along the transverse axis. The pCA3-dCA1 network preferentially processes non-spatial information, such as time, odor, and object, across a variety of behavioral tasks, while the dCA3-pCA1 network is more engaged in tasks requiring spatial memory (Ito et al. 2012, Hartzell et al. 2013, Nakamura et al. 2013, Nakazawa et al.

2016, Beer et al. 2018, Flasbeck et al. 2018). Electrophysiological recordings reveal a graded spatial representation along the transverse axis of the hippocampus proper, with stronger spatial tuning observed in pCA3 and pCA1 compared with dCA3/CA2 and dCA1 (Henriksen et al. 2010, Lee et al. 2015, Lu et al. 2015, Oliva et al. 2016), a more coherent spatial representation to conflicting local and global cues in dCA1 than in pCA1 (Deshmukh 2021), as well as a decreased sensitivity to contextual changes or conflicting cues along the CA3-to-CA2 axis (Lee et al. 2015, Lu et al. 2015). Furthermore, recordings from multiple brain regions also highlight the importance of coordinated ensemble activity between LEC and dCA1 in odor-associated memory (Igarashi et al. 2014, Li et al. 2017). However, the specific manner in which CA1 neurons respond to contextual changes along the transverse axis and the degree to which selective inputs from upstream brain regions determine their activity remain unclear. To investigate this, we manipulated spatial, color, and object cues in the recording environment and compared changes in place cell ensemble activity across the entire proximo-distal extent of CA1.

Methods

Subjects

The experiments were conducted at the Kunming Institute of Zoology, Chinese Academy of Sciences (Kunming, China) in compliance with the guidelines for the care and use of laboratory animals. The study received approval from the Institutional Animal Care and Use Committee of the Kunming Institute of Zoology (KIZ-IACUC-RE-2021-06-019). Data were collected from twenty male Long-Evans rats (3–4 months old, 500–600 g at the time of implantation). Five rats (IDs: 17899, 18547, 18548, 18549, 19326) from a previous study (Lu et al. 2015) contributed data from proximal half of CA1. The remaining fifteen rats (IDs: R0087, R0088, R0089, R0092, R0172, R0175, R0388, R0389, R0390, R0391, R0621, R0769, R0836, R1026, R1028) were implanted with a multi-tetrode "hyperdrive" targeting the right hippocampus. The animals were maintained on a reversed 12-hour light/dark cycle (lights off from 9 am to 9 pm) under standard laboratory conditions (temperature: 20–23°C, relative humidity: 40–60%). Following surgery, the rats were housed individually, and experimental procedures were

conducted during the dark phase. During the experimental period, the animals were mildly food restricted to maintain their weight at 85%–90% of free-feeding body weight.

Electrode preparation

The multi-tetrode "hyperdrive" which consisted of 18 independently movable tetrodes made of 17-μm polyimide-coated platinum-iridium (90–10%) wire (California Fine Wires, USA) was prepared as previously described (Lu et al. 2018). The electrode tips were plated to reduce impedance to 150–250 kΩ at 1 kHz (Biomega, Bio-Signal Technologies, China) and sterilized with ethylene oxide (Sanqiang Medical, China) within 48 hours before implantation.

Surgery

Rats were anesthetized with isoflurane (air flow: 0.8–1.0 L/min, 0.5–3% isoflurane vol/vol mixed with oxygen), with the concentration adjusted based on physiological monitoring (RWD Life Science, China). Upon induction of anesthesia, Metacam (2 mg/mL, 1 mg/kg body weight), Baytril (50 mg/mL, 5 mg/kg) and atropine (0.5 mg/mL, 0.1 mg/kg) were administered subcutaneously. The animal's head was then fixed in a stereotaxic frame (RWD Life Science, China). Local anesthetic (2% Lidocaine, 200 μL) was applied under the skin before making the incision. After removing the skull and dura, the rats were immediately implanted with the hyperdrive. Tetrodes were inserted into the cortical surface above the right hippocampus (antero-posterior (AP) from 3.2 to 5.6 mm, medio-lateral (ML) from 1.0 to 4.5 mm relative to bregma). The hyperdrive was secured to the skull with jewelers' screws and dental cement. Two screws above the cerebellum were connected to the hyperdrive ground, and two reference tetrodes were left in a quiet area of the cortex for differential recording.

Electrophysiological recordings

For the initial 3–4 weeks post-surgery, the tetrodes were advanced daily until the dorsal CA1 pyramidal cell layer was reached, where large-amplitude theta-modulated complex-spike activity was observed. The electrodes remained stationary on the recording day to ensure stable recordings. Broadband neural signals were recorded from hyperdrive using a multichannel data acquisition system (Zeus, Bio-Signal Technologies, China). Unit activity was amplified (× 192)

and band-pass filtered (300 to 7,500 Hz). Spike waveforms exceeding the −50 μV threshold were time-stamped and digitized at 30 kHz for 1 ms. Local field potential (LFP) signals, one per tetrode, were recorded in the 0.3–300 Hz frequency band at a sampling rate of 1,000 Hz. Light-emitting diodes (LEDs) on the headstage were tracked simultaneously at a 50 Hz to monitor the animal's position, using a real-time video tracking system (Cyclops, Bio-Signal Technologies, China).

Behavioral paradigms

Each task comprised four 10-minute exploration trials within the recording box, and five 5-minute rest periods in a flower pot placed on a pedestal outside the box (Figure S1A). Exploration trials were designed in an A-B-B-A configuration, with A and B representing distinct test conditions. Animals were motivated to explore the recording box by randomly scattered cookie crumbs. One week after surgery, mildly food-restricted rats were trained daily in the color-reversal task in two separate rooms until they could cover the entire arena within 10 minutes across all trials. Once the tetrodes reached the CA1 cell layer, the animal underwent sequential testing and recording in the color-reversal task, the two-room task and three object-related tasks.

Test environments

Recording boxes measured 100 cm × 100 cm, featuring a metal frame and four individually exchangeable plastic walls (black on one side, white on the other; 100 cm × 50 cm). Cue cards (white cue card for black walls and vice versa; 50 cm high and 30 cm wide) were placed at the center of one wall. Distal background cues were obscured by curtains encircling the recording box (120 cm × 120 cm in size) for the color-reversal task and object-related tasks but not for the two-room task. The pedestal with a flower pot was positioned between the test box and the experimenter, outside the curtains. The recording rooms for the two-room task were similar in size but featured different spatial arrangements.

The color-reversal task

As detailed previously, this task was designed to elicit rate remapping in the hippocampus

(Leutgeb et al. 2005, Lu et al. 2013, Lu et al. 2015). Fifteen rats were trained/tested in the recording box at a fixed location for four trials daily, with trials 1 and 4 conducted with black walls and trials 2 and 3 with white walls (Figures S1B–C). The floor of the recording box was cleaned and wiped with 75% ethanol after each trial.

The two-room task

This task was designed to evoke global remapping in the hippocampus (Leutgeb et al. 2005, Lu et al. 2015). Fifteen rats were tested in similar recording boxes with black walls located at fixed locations in two separate recording rooms, with trials 1 and 4 in room A and trials 2 and 3 in room B (Figure S1D). The floor of the recording box was cleaned and wiped with 75% ethanol after each trial.

Tasks with objects

The object-related tasks were designed to induce local firing changes in the hippocampus (Vandrey et al. 2021, Nagelhus et al. 2023). Fourteen rats (excluding R0087) were sequentially tested in the object-placement task, the object-relocation task, and the novel-object task following the two-room task.

<u>The object-placement task:</u> Animals were tested in the black recording box at a constant location for four trials, with two identical familiar objects (glass bottles filled with white stones) placed in quadrants 3 and 4 of the box for trials 2 and 3 (Figures S1E–F). The floor of the recording box was cleaned, and the objects were thoroughly wiped with 75% ethanol before each trial.

<u>The object-relocation task:</u> Animals were tested in the black box containing two familiar objects for four trials, with the object in quadrant 4 relocated to quadrant 1 for trials 2 and 3 (Figures S1G–H). The floor of the recording box was cleaned, and the objects were thoroughly wiped with 75% ethanol before each trial.

<u>The novel-object task:</u> Animals were tested in the black box containing two objects for four

trials, with the familiar object in quadrant 4 replaced by a novel object in trials 2 and 3 (Figures S1I–J). The floor of the recording box was cleaned, and the objects were thoroughly wiped with 75% ethanol before each trial.

Occupation time and discrimination index

Occupation time (OT) and discrimination index (DI) were employed to quantify the rat's preference for objects in the object-placement task and for the relocated/novel object in the object-relocation and novel-object tasks. OT was defined as the proportion of time spent around the objects relative to the total time in the recording box, and DI was calculated as:

$$DI = \frac{T_r - T_u}{T_r + T_u};$$

where T_r is the time rat spent around the relocated/replaced object, and T_u is the time rat spent around the unchanged object. A higher DI value indicates a greater preference for the relocated/novel object.

Histology and recording sites

Following the completion of electrophysiological recordings, the electrodes were maintained in their positions. The rats were subsequently euthanized, perfused with formalin, and their brains were extracted. Frozen sections, 40 μm in thickness, were prepared and stained using cresyl-violet. The location of each tetrode tip was then identified and recorded. The subregions of the hippocampal proper were delineated based on established criteria (Henriksen et al. 2010, Cappaert et al. 2015). The software ImageJ was utilized to estimate the normalized position along the proximo-distal axis of the CA1 region for each recording site. Hand-drawn lines tracing the CA1 pyramidal cell layer were extended from the CA2/CA1 border to the CA1/subiculum border, passing through the recording site on each section. The distance from the CA2/CA1 border to the recording site was measured and normalized by the total length of the CA1 region on the same section. Based on these normalized positions, recording sites were categorized into proximal (pCA1, 0–0.33), middle (mCA1, 0.33–0.67), and distal (dCA1, 0.67–1) subregions.

LFP power

Local field potential (LFP) signals, collected within a 15 cm radius around each object during trials 1 and 2, were extracted and concatenated for analysis. The Chronux Toolbox in Matlab (version 2.12, http://chronux.org/) was employed to estimate the absolute power spectra for consecutive 5-second time windows of the LFP, spanning frequencies from 0 to 100 Hz (Bokil et al. 2010). The time-bandwidth product (TW) was set to 3, and the number of tapers (K) was 5. The normalized change in LFP power at each frequency (1 Hz bins) surrounding each object was calculated using the following formula:

$$LFP\ power\ change = \frac{P_2 - P_1}{P_2 + P_1};$$

Where P_2 and P_1 represent the absolute LFP power at a specific frequency near the object in trials 2 and 1, respectively. Experiments with subpar recording quality were excluded from further analysis.

Spike sorting and cell classification

Spike sorting was conducted manually using the MClust graphical cluster-cutting tool in Matlab (version 4.4, A.D. Redish) in two-dimensional projections of the multidimensional parameter space (consisting of waveform amplitudes, waveform energies, and waveform peak-valley differences). Waveform and autocorrelation functions were also utilized as tools for separation and classification. Clustering was performed on the entire data set of each experiment, and then the spikes were subsequently divided into four exploration trials.

Putative excitatory cells were distinguished from putative interneurons and bypassing axons based on spike width (peak-to-trough waveform durations greater than 250 μs), average rate (less than 5 Hz), and the occasional presence of bursts. Only cells classified as putative excitatory neurons were included in the subsequent analyses. Cells that were recorded repeatedly in the same task were excluded from analyses.

Rate maps and place fields

Position estimates were based on tracking of the LEDs on the headstage connected to the

hyperdrive. Data were filtered for speed, including only epochs with instantaneous running speeds between 2.5 and 100 cm/s. The mean firing rate for each cell was calculated by summing the total number of spikes and dividing by the time the animal spent in that trial. Place field analyses were conducted exclusively for cells with a mean firing rate of 0.10 Hz or higher (defined as active cells). Spatial firing rate distributions (place fields) for each well-isolated neuron were generated by summing the spikes within a specific location bin (5 cm × 5 cm), dividing by the duration of time the rat occupied that location, and applying Gaussian smoothing centered on each bin, as previously described (Lu et al. 2015). A place field was defined as a contiguous region of at least 225 cm^2 (nine or more 5 × 5 cm bins) where the firing rate exceeded 20% of the peak rate and the peak firing rate of the area was 1 Hz or greater. The number of non-overlapping place fields was estimated for each cell.

Theta modulation and phase locking

The theta modulation index (TMI) was computed as described (Cacucci et al. 2004) to assess the temporal modulation of firing within the theta frequency range (7–10 Hz) of each cell. A temporal autocorrelogram was constructed by tallying the occurrences of a spike within each 5-ms bin, ranging from 0 to 500 ms, given a spike of the cell at time 0, and then dividing by the total trial length to determine the rate of occurrence for each bin. TMI was calculated as:

$$TMI = \frac{P-T}{P+T};$$

where P and T represent the theta modulation peak (mean of bins 100–140 ms) and trough (mean of time bins 50–70 ms), respectively.

Theta phase locking was quantified to measure the coupling of CA1 cells to hippocampal theta oscillations. LFP recordings were bandpass-filtered within the theta range (7–10 Hz), and theta phases for each time point were estimated using the Hilbert transform function from the Signal Processing Toolbox in Matlab. Theta phases for CA1 place cell spikes were collected and sorted into 10° bins. The mean vector length (MVL) was calculated using the Circular Statistics Toolbox in Matlab (version 1.21, P. Berens):

$$MVL = \left|\frac{1}{n}\sum_i (a_i \cos(\theta_i) + j a_i \sin(\theta_i))\right|;$$

where j is the imaginary number, n is the number of circular bins ($n = 36$), θ_i and a_i are the theta phase and the response for the i-th bin, respectively.

Spatial information, coherence and stability

The spatial information rate in bit per second (SI_r) and the spatial information content in bit per spike (SI_c) were calculated as described (Skaggs et al. 1996):

$$SI_r = \sum_i p_{i\lambda_i} \log_2 \frac{\lambda_i}{\lambda};\ SI_c = \sum_i p_i \frac{\lambda_i}{\lambda} \log_2 \frac{\lambda_i}{\lambda};$$

where λ_i is the mean firing rate of a unit in the i-th bin, λ is the overall mean firing rate and p_i is the probability of the animal being in the i-th bin (occupancy in the i-th bin / total recording time).

Spatial coherence was estimated as the first-order spatial autocorrelation of the unsmoothed place field map, that is, the mean correlation between the firing rate of each bin and the averaged firing rate in the eight adjacent bins.

Spatial stability was determined by comparing the firing pattern in the first half of each trial to the second half. The rate map for each half was smoothed and binned into 5 cm × 5 cm matrices, and the firing rates in the bins of the two half-trial maps were then correlated for each trial.

Spatial correlation

Firing patterns were compared across trials using a spatial correlation procedure. Each map was smoothed and binned into 5 × 5 cm matrices, and the firing rates in the pixels of the two maps were correlated for each cell. Spatial correlation between two inactive trials (firing rates both below 0.1 Hz) was excluded to avoid artifacts. For the two-room task, rate maps were rotated in 90° steps to identify the maximum spatial correlation score when compared across rooms. For the color-reversal task and the two-room task, firing patterns were compared between trials 1 and 3, and trials 2 and 4 for different conditions to minimize the effect of elapsed time, while trials 1 and 4, and trials 2 and 3 were compared for matching conditions. For object-related tasks, firing patterns were compared between trials 1 and 2 for different conditions, and between

trials 2 and 3 for matching conditions to avoid the effect of hysteresis in trial 4.

Rate difference and rate difference by field

The change in overall firing rate across trials was calculated as rate difference (RD):

$$RD = \left|\frac{FR_1 - FR_2}{FR_1 + FR_2}\right|;$$

where FR_1 is the mean firing rate of a cell in one trial; FR_2 is the mean firing rate of the same cell in a second trial. RD = 1 means that the cell was active in one trial only; RD = 0 means that the firing rates in the two trials were the same.

Rate difference by field (RD_f) was computed to mitigate the neutralization effect across individual place fields from the same cell:

$$RD_f = \sum_i w_i RD_i \ ;$$

where RD_i is the rate difference of the i-th place field, and w_i is the weight of the i-th place field estimated from its firing rate. RD_f was not computed when changes in firing location occurred.

Population vector correlation

For the entire population of cells recorded under each condition, including those with firing rates below 0.1 Hz and spatial information content below 0.9586 bit/spike, rate vectors were constructed. This process involved arranging all rate maps for all cells in an x-y-z stack, where x and y denoted the two spatial dimensions (20 × 20 bins), and z represented the cell-identity index (Leutgeb et al. 2005). For the two-room task, rate maps were rotated analogously to the spatial correlation analyses performed for each cell. The distribution of bin rates along the z axis for a specific x-y location represented the composite population vector for that location. Population vectors from corresponding positions were then correlated across pairs of trials.

Shuffling

Shuffling of spatial information content was conducted on a cell-by-cell basis as previously described (Henriksen et al. 2010). Each CA1 cell recorded from the color-reversal task underwent 100 permutations. In each permutation, the complete sequence of spikes fired by the

cell was time-shifted along the animal's path by a random interval ranging from 20 seconds to the total trial length minus 20 seconds. The trial's end was wrapped back to the beginning to allow for circular displacements. A rate map was generated for each permutation, and the distribution of spatial information content values across all permutations for all CA1 cells was determined. A putative excitatory neuron was considered a place cell if its spatial information content exceeded the 95th percentile of the shuffled distribution (0.9586 bit/spike).

For each CA1 band, a control distribution for spatial correlation analyses was established through a random permutation procedure. This procedure utilized all active maps (with mean firing rates higher than 0.10 Hz) from all cells recorded within that band (Lu et al. 2015). For each permutation, two distinct active maps from different cells were randomly selected and correlated in 90° rotation steps to achieve the highest correlation score. Ten thousand permutations were executed for each CA1 band. This method preserves the rate maps from each band within the shuffled data while eliminating the connections between maps. The distribution of random correlations from all 10,000 permutations was calculated, and the 95th percentile was determined.

Bayesian decoding

A Bayesian decoding algorithm was employed to convert ensemble spiking activity into positional information for each experiment. Decoding utilized a 2000 ms sliding time window that advanced by 200 ms with each step. The probability of a rat being at position x, given the number of spikes n from each unit recorded within a given time window, was estimated using Bayes' rule (Glaser et al. 2020):

$$P(x \mid n) = \frac{P(n|x)P(x)}{P(n)};$$

Here, the probabilistic likelihood $P(n|x)$ used the probability mass function of the Poisson distribution to calculate the likelihood of the observed number of spikes for a given neuron's activity pattern:

$$P(n \mid x) = \frac{e^{-\lambda}\lambda^{n}}{n!};$$

where λ is the expected number of spikes based on the tuning curve, and n is the actual observed

number of spikes within the given time window. The prior knowledge probability of position $P(x)$ was set to the frequency of the animal's presence in each state within the training data. The normalizing constant $P(n)$ ensured that the posterior probability $P(x|n)$, was summed to 1. For the visualization of decoding and the estimation of maximum decoding performance, only experiments with over 30 simultaneously recorded place cells in both CA1 bands were considered. Downsampling was applied to equalize cell numbers, and this process was repeated three times to determine the mean decoding accuracy value. For position decoding, 90% of the 4-trial data served as the training set, and the remaining 10% as the test set. This cross-validation procedure was repeated ten times (10-fold validation). For context decoding, data from trials 2 and 3 formed the training set, and 90% of trial 1 data served as the test set. This procedure was also repeated ten times. Decoding accuracy was expressed as:

$$R^2 = 1 - \frac{\Sigma_i(\hat{y}_i - y_i)^2}{\Sigma_i(y_i - \bar{y})^2};$$

Where $\hat{y}_i$ and y_i are the predicted and true position of the i-th time bin, respectively, and $\bar{y}$ is the mean position value.

Fitting

The EzyFit Toolbox in Matlab (version 2.44) was used to compute curve fitting for the average data from tetrodes. The explained variance was calculated as:

$$R^2 = \frac{\Sigma_i(\hat{y}_i - \bar{y})^2}{\Sigma_i(y_i - \bar{y})^2};$$

where $\hat{y}_i$ is the predicted value based on the curve fitting and normalized position of each tetrode; y_i is the averaged tetrode data; and $\bar{y}$ is the mean value across all tetrodes.

Statistical Procedures

Results are presented as median and interquartile range (IQR) due to the non-normal distribution of most data. The Kruskal-Wallis test was utilized to compare the firing properties of cells across CA1 bands. The Mann-Whitney U test and paired t-test were employed to compare two groups of unrelated and related measures, respectively. One-way repeated-measures ANOVA was applied to analyze running speed across trials. Regional differences in remapping between two conditions were assessed using two-way repeated-measures ANOVA

with a 3 × 2 factor design, considering condition pairs (matching or different) as a within-subject factor and CA1 bands as a between-subjects factor. Pearson's chi-square test was used to compare frequency distribution across groups, and Pearson correlation was calculated to measure the linear correlation between two variables. Holm-Bonferroni post-hoc tests identified significant differences between pairs, and the Benjamini and Hochberg method corrected for false discovery rate (FDR) in multiple hypothesis testing. The significance level was set at $P < 0.05$ for two-tailed tests. All statistical analyses were conducted using SPSS statistics software version 25 (IBM).

Results

Recording Positions

A total of fifteen rats were implanted with tetrodes targeting the right hippocampus. An additional five rats from a prior study (Lu et al. 2015) contributed data from the proximal half of CA1 for both the color-reversal task and the two-room task. The majority of recording sites were concentrated in the dorsal one-third of the hippocampus, with the collective dataset covering the entire proximo-distal extent of the CA1 region (Figure 1A). To facilitate cross-animal comparisons, recording positions were normalized for each tetrode, and the CA1 region was divided into three equal sized bands, with the distribution as follows: 39 tetrodes in the proximal band (pCA1), 43 in the middle band (mCA1), and 31 in the distal band (dCA1) (Figure S2).

Decreased spatial tuning from pCA1 to dCA1

The animals were initially trained and tested in the color-reversal task, which involved navigating a square box with alternating black or white walls to chase scattered cookie crumbles (Figures S1A–C). A total of 178 experiments were recorded from twenty animals, with mean running speed decreased gradually across four trials (Figure S3A), in line with previous observations (Leutgeb et al. 2004, Tsao et al. 2013). Analysis of the data yielded 4,218 well-isolated, putative CA1 pyramidal neurons across 113 tetrodes, with 3,034 neurons demonstrating activity within the recording box (mean firing rate exceeding 0.1 Hz). The

proportion of active cells diminished along the transverse axis of the CA1 region (Figure S3B). A total of 2,622 neurons with spatial information content scores above the 95th percentile of shuffled distribution were classified as place cells (Figure S3C–D) and were selected for further analysis. While the majority of active cells in CA1 displayed localized firing, a significantly higher proportion of place cells was observed in the proximal two-thirds of CA1 relative to dCA1 (Figure S3B).

We initiated our analyses by confirming the variance in place coding among CA1 subregions. Examination of place cell activity maps revealed that pCA1 contained cells with sharper and fewer place fields (Figure 1B). A significant divergence in peak firing rates was noted across subcompartments (median (25%–75% percentile), pCA1, 5.327 (3.103–8.262) Hz, mCA1, 4.948 (3.065–7.411) Hz, dCA1, 4.660 (2.854–7.407) Hz; Kruskal-Wallis test, 2,622 cells, H = 11.566, P = 0.003, Figure 1C), although mean firing rates remained consistent (Figure S3E). Place cells in dCA1 contained significantly more place fields compared to cells in the proximal two-thirds of CA1 (pCA1, 1.00 (1.00–1.50), mCA1, 1.00 (1.00–1.50), dCA1, 1.25 (1.00–1.75); H = 28.040, P < 0.001, Figure 1D), yet the overall size of firing fields was unchanged across subregions (Figure S3F). Place cells in pCA1 showed enhanced theta modulation (pCA1: 0.434 (0.333–0.540); mCA1: 0.410 (0.318–0.516); dCA1: 0.390 (0.290–0.494); H = 28.301, P < 0.001, Figure 1E) and a greater degree of phase locking to theta oscillations (Figure S3G) than cells located more distally. Furthermore, pCA1 cells exhibited a higher spatial information content (pCA1: 2.037 (1.565–2.560) bit/spike; mCA1: 1.995 (1.508–2.540) bit/spike; dCA1: 1.877 (1.454–2.429) bit/spike; H = 13.350, P = 0.001, Figure 1F), spatial information rate (Figure S3H), coherence (pCA1: 0.656 (0.546–0.757); mCA1: 0.664 (0.553–0.758); dCA1: 0.630 (0.507–0.715); H = 34.163, P < 0.001, Figure 1G), and stability (pCA1: 0.741 (0.590–0.836); mCA1: 0.711 (0.583–0.814); dCA1: 0.659 (0.521–0.769); H = 69.309, P < 0.001, Figure 1H) than dCA1 cells. The observed variations in spatial tuning were not attributed to the dorso-ventral distribution of recording sites, as cells recorded from the same transverse block of CA1 displayed a similar trend along the proximo-distal axis (Figure S3I). To confirm the proximo-distal gradient in spatial tuning, we trained a naive Bayes decoder to predict the rat's location based on population activity of place cells (Figure S3J). Decoding accuracy was

ensured by analyzing only experiments with over 30 place cells in each subregion. Proximally located cells demonstrated superior prediction accuracy compared to simultaneously recorded distal cells (Figure S3K), indicating stronger position coding at the proximal end of CA1.

To chart the decline in spatial tuning across the CA1 transverse axis, we plotted mean values for each measure against tetrode location. For all activity measures that varied across CA1 subregions, except the number of place fields, a significant monotonic decline was observed from the proximal to the distal end of CA1. This was substantiated by strong Pearson correlations between parameters and normalized recording position (all $P \leq 0.002$, 113 tetrodes). This decrease was primarily linear, with minimal improvement in explained variance from quadratic polynomial curve fitting (Figures 1I–N, and S3L–M). These results collectively demonstrate a gradual decline in spatial tuning from pCA1 to dCA1, consistent with previous reports (Henriksen et al. 2010, Oliva et al. 2016), and aligned with the selective spatial and non-spatial inputs from MEC and LEC (Nilssen et al. 2019).

Reverse J-shaped rate remapping along the transverse axis

Utilizing the same dataset, we next investigated whether CA1 place cells displayed similar heterogeneity in response to non-spatial changes along the transverse axis. Rate remapping, characterized by the alteration of firing rates within place fields while maintaining consistent firing locations (Latuske et al. 2017), is indicative of sensitivity to contextual changes. As anticipated from prior work (Leutgeb et al. 2005, Lu et al. 2013, Lu et al. 2015), rate remapping was induced in all twenty rats subjected to the color-reversal task (Figure S3N).

To assess the consistency of place field location across trials, we calculated the spatial correlation (SC) of rate maps, which quantifies the similarity in activity patterns from the same cell. SC scores were high for matching conditions but varied significantly across CA1 subregions (Figure 2A left panel, two-way repeated measures ANOVA, band: $F(2, 2619) = 26.679$, $P < 0.001$). SC moderately decreased between color-reversed conditions compared to matching conditions (color: $F(1, 2619) = 262.113$, $P < 0.001$), indicating adjustments in firing patterns in response to different colors. A significant band × color interaction was observed in

SC (F (2, 2619) = 28.724, $P < 0.001$). The reduction in SC due to color change differed significantly across subregions (pCA1: 0.032 (−0.003–0.106), mCA1: 0.010 (−0.020–0.049), dCA1: 0.025 (−0.011–0.091); Kruskal-Wallis test, 2,622 cells, H = 68.492, $P < 0.001$), with post hoc analysis revealing a nonlinear change in firing patterns along the proximo-distal axis, with larger differences in both pCA1 and dCA1 compared to mCA1 (Figure 2A right panel, Holm-Bonferroni post hoc tests, both $P < 0.001$). Separate analyses for tetrodes located in the proximal or distal half of the axis showed significant correlations in both halves for SC (proximal: r = −0.375, P = 0.002, Pearson correlation, 63 tetrodes; distal: r = 0.374, P = 0.007, 50 tetrodes). The changes in activity measures along the entire CA1 transverse extent were better explained by quadratic polynomial curve fitting (Figure 2B).

To quantify the extent of rate remapping, we computed the rate difference (RD), representing the normalized overall change in firing rate for each cell. Consistent with the pattern observed in SC, mCA1 contained the smallest proportion of strongly rate remapped place cells between different colors (Figure S3O). RD significantly differed between condition pairs and across CA1 subregions (Figure 2C left panel, color: F (1, 2619) = 288.514, $P < 0.001$; band: F (2, 2619) = 20.373, $P < 0.001$). A significant interaction between CA1 band and color in RD was observed (F (2, 2619) = 41.298, $P < 0.001$), along with regional variations in elevated RD between condition pairs (Figure 2C right panel, pCA1: 0.012 (−0.005–0.140), mCA1: 0.001 (−0.006–0.047), dCA1: 0.001 (−0.010–0.048); H = 38.540, $P < 0.001$). Cells in both pCA1 and dCA1 exhibited more pronounced rate redistribution than those in mCA1 when the wall color was reversed, with pCA1 showed a significant greater increase in RD between condition pairs (post hoc tests, both $P < 0.001$). Mean changes in RD for individual tetrodes were significantly correlated with recording position in both proximal and distal halves of the CA1 transverse axis (proximal: r = −0.452, $P < 0.001$; distal: r = 0.314, $P = 0.029$, Figure 2D). A similar result was obtained when rate difference for individual place fields were computed and summed according to their weight (Figures S3P–S), indicating that the lower rate changes in middle-to-distal CA1 were not due to neutralization of individually remapped place fields.

To compare activity changes for cell assemblies across CA1 subregions, we computed the

population vector correlation (PVC), which is sensitive to the composite distribution of firing location and rate, for all recorded pyramidal neurons, including non-place cells and inactive cells (Leutgeb et al. 2005). Population vectors from corresponding locations in the box were strongly correlated between matching conditions in all CA1 subregions. The correlations were weaker between black and white configurations (Figures 2E–F). The difference in PVC between conditions with reversed wall colors and conditions with matching wall colors was significant across subregions (color: $F(1, 1197) = 3336.027$, $P < 0.001$; band: $F(2, 1197) = 396.174$, $P < 0.001$; color × band: $F(2, 1197) = 448.356$, $P < 0.001$, Figure 2E left panel). mCA1 exhibited the smallest change in PVC between condition pairs (pCA1: 0.108 (0.085–0.147), mCA1: 0.031 (0.005–0.054), dCA1: 0.052 (0.022–0.094); $H = 541.211$, $P < 0.001$, 1,200 bins, post hoc tests, all $P < 0.001$, Figure 2E right panel).

A pronounced effect of hysteresis was observed in all subregions of CA1 in the color-reversal task. Activity patterns were more similar between trials 3 and 4, compared to trials 1 and 2, despite both involving black and white configurations (Figure S3T). To avoid the carryover effect in the analyses, data from the 1-2 trial pair (different color) and the 2-3 trial pair (same color) were compared, yielding similar results (data not shown). To verify the reverse J-shaped pattern of rate remapping along the CA1 transverse axis, a Bayesian decoder was trained with collective activities of place cells in trials 2 and 3 (white walls), predicting the rat's location in trial 1 (black walls). For the three experiments with over 30 simultaneously recorded place cells in both subregions, decoding accuracy was higher in mCA1 than in the other two CA1 subregions (Figure S3U), indicating a minimal activity change in mCA1 between black and white configurations. In summary, in the color-reversal task, which evoked rate remapping in the rat hippocampus, the shift in rate distribution varied significantly along the transverse axis of CA1, with robust redistribution of firing rates in pCA1, moderate redistribution in dCA1, and minimal redistribution in mCA1.

Graded global remapping along the proximo-distal axis

We further investigated whether the gradient in spatial tuning along the CA1 proximo-distal axis would exhibit a similarly monotonic decrease in global remapping. In a second set of

experiments, pyramidal neurons were recorded from the same twenty rats as they were tested in similar square boxes situated in two distinct rooms (Figures S1B&D), a paradigm known to trigger global remapping in hippocampal neurons (Leutgeb et al. 2005, Lu et al. 2015). Out of the nineteen rats from which valid place cell data were obtained, thirteen displayed clear global remapping, characterized by minimal correlation in firing fields between rooms, while the remaining six exhibited extensive rate remapping (Figure S4A). Similar individual differences have been observed in previous studies (Lu et al. 2013, Lu et al. 2015). The results from the six rate remapped animals were consistent with findings in the color-reversal task (Figures S4B–G). Further analysis was concentrated on the thirteen globally remapped rats, which displayed comparable behavior in the two-room task to that in the color-reversal task (Figure S4H). A total of 1,145 pyramidal neurons were recorded from 54 tetrodes, with 761 identified as place cells. As anticipated, a similar decrease in activity measures along the CA1 transverse axis was observed in these animals (Figures S4I–R).

Global remapping, characterized by the engagement of a second population of place cells to represent an distinct spatial map in the hippocampus (Latuske et al. 2017), is evident at the individual cell level by significant changes in firing location and rate within the recording box (Figure 3A). The degree of population overlap was consistent across CA1 subregions (Figure S4S). SC of individual place cells between repeated trials in the same room remained high for all CA1 subregions and decreased markedly between rooms (two-way repeated measures ANOVA, room: $F(1, 758) = 1175.415$, $P < 0.001$, Figure 3B, left panel), indicating substantial shifts in firing location across different rooms. Between-room SC showed a tendency to be higher in both middle and distal CA1 (band: $F(2, 758) = 13.538$, $P < 0.001$, Figure S4T). A pronounced room × band interaction in SC was observed ($F(2, 758) = 27.266$, $P < 0.001$). The reduction in SC in response to room change decreased progressively along the proximo-distal axis of CA1 (pCA1, 0.455 (0.256–0.747), mCA1, 0.354 (0.151–0.527), dCA1, 0.287 (0.095–0.504); Kruskal-Wallis test, 761 cells, $H = 41.735$, $P < 0.001$), with the most significant changes in pCA1 (Holm-Bonferroni post hoc tests, pCA1 vs mCA1, pCA1 vs dCA1, both $P < 0.001$), suggesting the largest shift in place field location in this subregion. The difference in SC decrease was not attributed to variations in sample size (Figure S4U). The decline in SC for

each tetrode was strongly correlated with its position along the CA1 transverse axis (Figure 3C).

The overall firing rate within the room is indicative of the activity level of individual neurons. A similar monotonic decrease in firing rate change was observed along the proximo-distal axis. RD was low for repeated trials in the same room for all subregions and increased markedly between trials across rooms (room: F (1, 758) = 410.559, $P < 0.001$; band: F (2, 758) = 0.380, $P = 0.684$). The enhancement in RD between condition pairs was strongly dependent on the subregion (room × band: F (2, 758) = 23.136, $P < 0.001$), with the greatest increase in pCA1 (pCA1, 0.261 (0.034–0.484), mCA1, 0.082 (0–0.352), dCA1, 0.073 (−0.003–0.274); H = 39.143, $P < 0.001$; post hoc tests, pCA1 vs mCA1, pCA1 vs dCA1, both $P < 0.001$, Figure 3D), suggesting a more interdependent activity in the distal two-thirds of CA1 across different rooms. The varied increase in RD was not attributed to variations in sample size (Figure S4V). A significant correlation was also observed between the change in RD and recording position (Figure 4E).

Lastly, ensemble coding across CA1 subregions was compared. Unlike the color-reversal task, the effect of hysteresis was minimal in the two-room task (Figure S4W). Correlations between corresponding population vectors were high between trials in the same room for all subregions and decreased substantially between trials in different rooms (room: F (1, 1197) = 28489.675, $P < 0.001$; band: F (2, 1197) = 83.437, $P < 0.001$). The reduction in PVC was region-dependent (room × band: F (2, 1197) = 800.992, $P < 0.001$): pCA1 showed the greatest decrease (0.678 (0.609–0.731)), mCA1 showed a moderate decrease (0.452 (0.367–0.535)), and dCA1 showed the smallest amount of decrease (0.388 (0.334–0.441); H = 679.871, $P < 0.001$, 1200 bins; post hoc tests, all $P < 0.001$, Figures 3F–G). In summary, when global remapping was induced in the hippocampus by distinct spatial environments, the representations of place cells were most orthogonal in proximal CA1, with the degree of orthogonalization decreasing monotonically along the transverse axis.

Reorganized CA1 population activity in the object-placement task

Hippocampal place cell activity is influenced by discrete objects within an open arena, as previously reported (Burke et al. 2011, Deshmukh et al. 2013, Vandrey et al. 2021, Nagelhus et al. 2023). In a third series of experiments, we examined if the response to familiar objects in CA1 varied by region. Place cell activity was recorded from fourteen rats as they were tested in the object-placement task, where two identical familiar objects were introduced into the recording box during trials 2 and 3 of the 4-trial experiment (Figures S1E–F and S5A). Despite no significant change in the rats' overall behavior due to the objects, alterations in theta and low-beta power were noted, potentially linked to exploratory behavior (Figures S5B–D). A total of 1,759 active place cells were identified from 2,711 putative pyramidal neurons recorded across 72 tetrodes in 65 experiments (Figure S5E). A substantial subset of place cells responded to the object placement, primarily by redistributing firing rates around the objects (Figure 4A). dCA1 had the highest proportion of cells that increased or decreased their number of receptive fields (pCA1, 40.88%, mCA1, 41.42%, dCA1, 49.93%; chi-square test, $\chi^2 = 12.777$, $P = 0.002$; post hoc tests, mCA1 vs dCA1, $P = 0.004$; pCA1 vs dCA1, $P = 0.019$), while mCA1 had the highest proportion of stable cells (Figures 4B and S5G). A pronounced hysteresis effect was observed in trial 4 of the object-placement task (Figure S5F), prompting the exclusion of trial 4 data from analyses to prevent carryover effects. The focus of analyses was on activity changes between trials 1 and 2 (before and after object placement) and between trials 2 and 3 (both with objects).

Since hippocampal place cells express the presence of objects on a population level (Nagelhus et al. 2023), all active place cells were included in the analyses. SC of these cells decreased uniformly across subregions with the introduction of familiar objects (Figure S5H, left panel). RD analyses indicated a slight overall increase in rate redistribution after object placement, with region-dependent changes and the most significant increase in pCA1 (Figure S5H, right panel). Unlike in previous experiments, no correlation was found between changes in SC or RD and recording position (SC, $r = 0.213$, $P = 0.072$, RD, $r = 0.049$, $P = 0.681$, Pearson correlations, 72 tetrodes). The overall PVCs were high for trials in matching conditions and decreased significantly with object introduction (two-way repeated measures ANOVA, object: $F(1, 1197) = 2475.217$, $P < 0.001$; band: $F(2, 1197) = 182.697$, $P < 0.001$), with the drop in PVC being

strongly dependent on the CA1 subregion (object × band: F (2, 1197) = 11.762, $P < 0.001$), and the most pronounced decrease observed in pCA1 (pCA1, 0.121 (0.070–0.183), mCA1, 0.084 (0.037–0.157), dCA1, 0.095 (0.050–0.158), Kruskal-Wallis test, 1,200 bins, H = 38.042, $P < 0.001$; Holm-Bonferroni post hoc tests, pCA1 vs mCA1, pCA1 vs dCA1, both $P < 0.001$, Figures 4C–D). Bayesian decoding showed significantly better prediction in mCA1 than in dCA1 (Figure S5I). Correlation of population vectors in each spatial bin revealed that most PVC decreases were localized around the objects, diminishing with distance, consistent with a previous report (Nagelhus et al. 2023). Dispersed activity changes away from the objects were also noted in pCA1 and dCA1, likely not a direct response to the objects.

To further characterize the activity changes due to object placement, we defined an object region, which contained the area within 20 cm around the center of each object. This allowed for the comparison of direct and indirect object responses by quantifying spatial bins inside and outside the target region. Although dCA1 place cells showed lowest SC and highest RD scores within the object region after object placement, changes in SC and RD between trial pairs were not significantly different across CA1 subregions (SC: object, F (1, 1196) = 271.560, $P < 0.001$; band, F (2, 1196) = 12.690, $P < 0.001$; object × band, F (2, 1196) = 1.599, $P = 0.203$. RD: object, F (1, 1756) = 198.557, $P < 0.001$; band, F (2, 1756) = 17.791, $P < 0.001$; object × band, F (2, 1756) = 0.210, $P = 0.811$). Population analysis for bins within in the object regions showed a significant regional difference across CA1 subregions (object: F (1, 237) = 2262.040, $P < 0.001$; band: F (2, 237) = 96.016, $P < 0.001$; object × band: F (2, 237) = 4.720, $P = 0.010$), with a slightly higher PVC decrease in mCA1 than in dCA1 (pCA1, 0.199 (0.171–0.228), mCA1, 0.215 (0.174–0.285), dCA1, 0.185 (0.154–0.239); H = 7.232, $P = 0.027$, 240 bins, post hoc tests, mCA1 vs dCA1, $P = 0.034$; Figure 4E).

Outside the object region, CA1 place cells exhibited a constant decrease in SC across subregions between trial pairs (object, F (1, 1439) = 216.332, $P < 0.001$; band, F (2, 1439) = 31.664, $P < 0.001$; object × band, F (2, 1439) = 2.032, $P = 0.131$; Figure 4F top). mCA1 cells displayed minimal firing rate change after object placement, akin to rate remapping (RD: object, F (1, 1756) = 168.577, $P < 0.001$; band, F (2, 1756) = 12.823, $P < 0.001$; object × band, F (2,

1756) = 4.189, $P = 0.015$). The increase in RD between conditions varied significantly across CA1 subregions (pCA1, 0.080 (−0.037–0.275), mCA1, 0.033 (−0.059–0.192), dCA1, 0.062 (−0.087–0.244); H = 9.868, $P = 0.007$, 1759 cells, post hoc tests, pCA1 vs dCA1, $P = 0.064$, pCA1 vs mCA1, $P = 0.005$; Figure 4F middle). The change in RD was not related to sample size or exploratory behavior around objects (Figures S5J–K). Population analysis revealed a PVC distribution pattern resembling rate remapping after object placement along the CA1 transverse axis (object: F (1, 957) = 2043.235, $P < 0.001$; band: F (2, 957) = 221.229, $P < 0.001$; object × band: F (2, 957) = 32.592, $P < 0.001$), and a reverse J-shaped change in PVC between trial pairs (pCA1, 0.096 (0.065–0.150), mCA1, 0.063 (0.026–0.107), dCA1, 0.075 (0.042–0.130), H = 66.740, $P < 0.001$, 960 bins; post hoc tests, all $P \leq 0.004$; Figure 4F bottom).

In summary, the introduction of familiar objects into the open box elicited both direct and indirect responses in CA1. The direct response led to changes in population activity mainly around the objects, while the indirect response was more evident away from the objects. Neurons in mCA1 showed the strongest local response to the objects but the weakest overall reorganization of population activity, possibly due to greater out-region rate redistributions in pCA1 and dCA1.

Ascendant response to the translocated object from pCA1 to dCA1

Given the critical role of the hippocampus and MEC in object-location memory, evidenced by deficits following damage to these areas (Aggleton et al. 2020), we investigated whether the presentation of object location in CA1 exhibited a gradient along the proximo-distal axis, similar to spatial tuning. In a fourth set of experiments, the same fourteen rats participated in the object-relocation task, where a familiar object was moved from its original location in quadrant 4 to quadrant 1 of the recording box (Figures S1G–H and S6A–B). Despite variations in individual responses to object translocation, the overall discrimination index remained unchanged (Figure S6C). Exploration around the displaced object was accompanied by minor fluctuations in theta and low-beta power, with regional differences observed at 8–9 and 14–15 Hz (Figure S6D). A total of 2,367 putative pyramidal neurons were recorded across 69 tetrodes in 59 experiments, of which 1,486 were identified as active place cells (Figure S6E). A

substantial subset of CA1 place cells altered their firing patterns, primarily through changes in firing rate around the displaced object (Figure 5A). Contrary to expectations, dCA1, not pCA1, had the highest proportion of cells responsive to the translocation (pCA1, 63.88%, mCA1, 71.81%, dCA1, 78.66%; chi-square test, $\chi^2 = 20.691$, $P < 0.001$; post hoc tests, pCA1 vs mCA1, $P = 0.081$; mCA1 vs dCA1, $P = 0.015$; pCA1 vs dCA1, $P < 0.001$; Figure 5B). Due to hysteresis (Figure S6F), the analyses focused on activity changes between trials 1 and 2 (before and after relocation) and between trials 2 and 3 (under matching condition).

SC for individual place cells was high in matching trials and slightly reduced after object relocation across all CA1 subregions (two-way repeated measures ANOVA, relocation: F (1, 1483) = 153.986, $P < 0.001$; band: F (2, 1483) = 21.400, $P < 0.001$). The extent of SC reduction varied significantly by subregions (relocation × band: F (2, 1483) = 4.917, $P = 0.007$), with the least decrease in pCA1 (0.024 (−0.026–0.121)), a moderate reduction in mCA1 (0.049 (−0.021–0.175)), and the most in dCA1 (0.069 (−0.027–0.233), Kruskal-Wallis test, 1,486 cells, H = 10.123, $P = 0.006$; Holm-Bonferroni post hoc tests, pCA1 vs dCA1, $P = 0.005$, Figure 5C). A significant correlation was observed between change in SC and tetrode location (r = 0.347, $P = 0.004$, Pearson correlation, 69 tetrodes, Figure 5D). The increase in RD between trial pairs across CA1 subregions mirrored the SC decrease (relocation: F (1, 1483) = 147.858, $P < 0.001$; band: F (2, 1483) = 20.702, $P < 0.001$), with a near-significant interaction between relocation and band (F (2, 1483) = 2.609, $P = 0.074$). The elevation in RD between trial pairs increased progressively from pCA1 to dCA1 (pCA1, 0.044 (−0.073–0.205), mCA1, 0.057 (−0.057–0.221), dCA1, 0.112 (−0.056–0.308), H = 9.346, $P = 0.009$, 1,486 cells; post hoc tests, pCA1 vs dCA1, mCA1 vs dCA1, both $P < 0.05$, Figure 5E). The shift in RD for individual tetrodes correlated significantly with recording position (r = 0.243, $P = 0.044$, Pearson correlation, 69 tetrodes, Figure 5F). The graded changes in SC and RD were unrelated to exploratory behavior around objects or sample size (Figures S6G–I), and similar results were obtained when rate changes were computed for individual place fields (Figures S6J–K).

Correlations between corresponding population vectors in each spatial bin altered similarly to SC (relocation: F (1, 1197) = 1097.785, $P < 0.001$; band: F (2, 1197) = 20.565, $P < 0.001$;

740 relocation × band: F (2, 1197) = 26.839, $P < 0.001$). The decline in PVC between trial pairs
741 expanded from pCA1 to dCA1 (pCA1, 0.055 (0.014–0.111), mCA1, 0.068 (0.030–0.127),
742 dCA1, 0.077 (0.043–0.138), H = 44.493, P < 0.001, 1,200 bins; post hoc tests, pCA1 vs dCA1,
743 pCA1 vs mCA1, both $P < 0.001$; mCA1 vs dCA1, $P = 0.063$, Figure 5G). Bayesian decoding
744 of context showed significantly improved predictions in more proximally located regions along
745 the CA1 transverse axis (Figure S6L). Similar to the object-placement task, a substantial
746 decrease in PVC was observed for bins around the right object before and after object
747 displacement (Figure 5H left). However, pCA1 exhibited the least degree of reorganization in
748 activity pattern within the target region (pCA1, 0.081 (0.054–0.114), mCA1, 0.212 (0.147–
749 0.269), dCA1, 0.225 (0.155–0.303), H = 125.736, $P < 0.001$, 240 bins; post hoc tests, pCA1 vs
750 dCA1, pCA1 vs mCA1, both $P < 0.001$; Figures 5H and S6M left). For spatial bins outside the
751 target region, the change in PVC was minimal, and its linear proximo-distal distribution differed
752 from the reverse J-shaped distribution observed in the object-placement task (pCA1, 0.043
753 (0.009–0.106), mCA1, 0.049 (0.026–0.091), dCA1, 0.063 (0.038–0.101), H = 17.077, $P <$
754 0.001, 960 bins; post hoc tests, pCA1 vs dCA1, mCA1 vs dCA1, both $P < 0.05$, Figures 5H,
755 S5L and S6M right), suggesting that translocation of a pre-existing object did not trigger rate
756 remapping in CA1. In summary, translocation of a single familiar object within the open arena
757 induced more pronounced ensemble activity changes around the object in distal two-thirds of
758 CA1, with minimal change outside the target region.
759
760 **Enhanced rate redistribution to the novel object from pCA1 to dCA1**
761 Unlike object-location memory, object-recognition memory is significantly dependent on the
762 perirhinal cortex (PER), which projects to LEC and dCA1 (Cappaert et al. 2015, Aggleton et al.
763 2020), highlighting the importance of the PER/LEC-dCA1 network in discriminating object
764 identity. We investigated whether this selective PER/LEC input to dCA1 leads to a proximo-
765 distal gradient in place cell activity in response to the novel object. The same fourteen rats were
766 tested in the novel-object task, where the familiar object on the right was replaced by a novel
767 object during trials 2 and 3 (Figures S1I–J and S7A–B). Across all rats, the total exploration
768 time around the novel object was comparable to that of the familiar object, and theta and low-
769 beta power remained largely unchanged (Figures S7C–D). A total of 1,451 active place cells

770 were identified from 2,207 putative pyramidal neurons recorded across 67 tetrodes in 54
771 experiments. Unlike previous tasks, which showed lower recruitment of place cells in dCA1
772 compared to pCA1, the novel-object task exhibited a similar activation of place cells across
773 subcompartments of CA1 (Figure S7E), consistent with findings that more dCA1 neurons are
774 engaged upon exposure to a novel object (Ito et al. 2012). A considerable subset of place cells
775 adjusted their firing rates in response to the novel object (Figure 6A). As expected, dCA1 had
776 the highest proportion of novelty-response cells (pCA1, 53.38%, mCA1, 63.02%, dCA1,
777 73.58%; chi-square test, $\chi^2 = 37.366$, $P < 0.001$; post hoc tests, all $P \leq 0.021$; Figure 6B). Given
778 the minimal changes in ensemble activity between trials 3 and 4 for all subregions (Figure S7F),
779 the analyses focused on shifts in firing rate between trials 1 and 2 (object identity switched) and
780 between trials 2 and 3 (unchanged).
781
782 SC scores of individual place cells were high for all subregions under matching conditions and
783 only slightly decreased after object replacement (two-way repeated measures ANOVA, novelty
784 F (1, 1448) = 69.447, $P < 0.001$; band: F (2, 1448) = 21.964, $P < 0.001$). There was no
785 interaction between CA1 band and novelty (F (2, 1448) = 0.528, $P = 0.590$), indicating no
786 regional difference in SC change between trial pairs (Figure 6C). The overall changes in firing
787 rate for individual place cells were marginally but significantly enhanced in trials pairs before
788 and after object replacement (novelty F (1, 1448) = 58.170, $P < 0.001$; band: F (2, 1448) =
789 10.527, $P < 0.001$), with the degree of enhancement strongly dependent on place cell location
790 (novelty × band: F (2, 1448) = 6.169, $P = 0.002$). Neurons in pCA1 displayed the least increase
791 in RD (0.008 (−0.101–0.120)), compared with cells in mCA1 (0.036 (−0.064–0.162)) and
792 dCA1 (0.054 (−0.085–0.225), Kruskal-Wallis test, 1,451 cells, H = 13.604, $P = 0.001$; Holm-
793 Bonferroni post hoc tests, both $P < 0.05$, Figure 6D). The enhancement in RD correlated
794 significantly with recording positions (r = 0.356, $P = 0.003$, Pearson correlation, 67 tetrodes,
795 Figure 6E). The graded changes in RD were not related to exploratory behavior around objects
796 or sample size (Figures S7G–I). Similar results were obtained for rate difference scores
797 calculated from individual place fields (Figures S7J–K).
798
799 Ensemble activity of all pyramidal neurons, as measured by PVC, showed a marginal decrease

after object replacement (novelty: F (1, 1197) = 1388.100, $P < 0.001$; band: F (2, 1197) = 261.805, $P < 0.001$), with a significant interaction between novelty and CA1 band (F (2, 1197) = 12.330, $P < 0.001$). Cell assemblies in pCA1 exhibited the smallest change in activity pattern to the novel object (pCA1, 0.031 (0.006–0.065), mCA1, 0.040 (0.023–0.061), dCA1, 0.047 (0.014–0.079), H = 19.995, $P < 0.001$, 1,200 bins; post hoc tests, pCA1 vs. dCA1, pCA1 vs. mCA1, both $P \leq 0.007$, Figure 6F). Bayesian decoding of context showed a better prediction for cells located in mCA1 than in dCA1 (Figure S7L). Compared to the other two object-related tasks, reorganization of population activity to the novel object was less pronounced and less focused for all CA1 subdivisions (Figure 6G left panel). However, the regional variance in response to the novel object was primarily attributed to the subtle difference in activity change around the object (bins around the novel object: pCA1, 0.005 (−0.014–0.028), mCA1, 0.034 (0.021–0.046), dCA1, 0.070 (0.053–0.082), H = 61.612, $P < 0.001$, 120 bins; post hoc tests, all $P \leq 0.001$), as ensemble activity changes outside the object region remained largely constant across CA1 subregions (bins outside the object region: pCA1, 0.035 (0.009–0.069), mCA1, 0.041 (0.023–0.064), dCA1, 0.044 (0.012–0.078), H = 5.689, $P = 0.058$, 1,080 bins; Figures 6G and S7M). To conclude, place cells located more distally along the CA1 transverse axis displayed greater firing rate redistribution around the novel object, likely due to preferential inputs from object-identity cells from LEC and PER (Deshmukh et al. 2011, Burke et al. 2012, Deshmukh et al. 2012, Huang et al. 2023).

Discussion

Our study provides a detailed characterization of how CA1 subcompartments respond to various spatial and non-spatial modifications in the rat hippocampus. We uncovered three distinct patterns of cue representation along the proximo-distal axis in CA1 that may affect the overall output of hippocampal function: a gradient of decreasing spatial information processing, an increase in the representation of local object features, and most intriguingly, a reverse J-shaped response to non-spatial environmental changes (Figure S8). These patterns in population response are largely attributed to the distinct nature of contextual cues, and their association with selective inputs from particular neuron populations, predominately locating in the

entorhinal cortex (Deshmukh et al. 2011, Tsao et al. 2013, Wang et al. 2018, Tukker et al. 2022, Huang et al. 2023).

Direct entorhinal inputs shape rate and global remapping patterns in CA1

The entorhinal and CA3-CA2 projections are the primary afferent pathways to the CA1 region in rats. Our findings corroborate the established view that the spatial tuning and global remapping in the CA1 region of rats exhibit a gradient that decreases from the proximal to the distal end (Figures 1&3), aligning with previous findings (Henriksen et al. 2010, Oliva et al. 2016, Deshmukh 2021). Global remapping in the rat hippocampus is accompanied by a realignment of activity patterns in grid cells, head direction cells, and border cells within the MEC (Fyhn et al. 2007, Solstad et al. 2008). This reorganization of activity appears to reduce the spatial information overlap, potentially enhancing distinct spatial representations in pCA1. In contrast, LEC neurons, which encode shared non-spatial features, may sustain their activity levels, contributing to a more generalized ensemble activity in dCA1 (Leutgeb et al. 2004, Hartzell et al. 2013). The observed gradients in spatial selectivity and global remapping can thus be attributed to differential inputs from MEC and LEC, with pCA1 predominantly receiving spatial signals from MEC, and dCA1 receiving more non-spatial signals from LEC (Knierim et al. 2014).

A notable discovery in our research is the identification of a reverse J-shaped rate remapping pattern within CA1 (Figures 2&4). The elevated rate redistribution in both pCA1 and dCA1 may suggest contributions from both MEC and LEC to hippocampal rate coding. Certain LEC neurons are known to remap in response to contextual changes in the environment, and disrupting LEC function through lesions has been shown to partially impair rate coding in CA3 (Lu et al. 2013, Huang et al. 2023). This supports the hypothesis that LEC provides modulated non-spatial inputs critical for hippocampal rate remapping (Renno-Costa et al. 2010). Conversely, MEC grid cells maintain consistent firing locations in the same spatial context but exhibit reliable rate redistribution in response to color manipulations (Marozzi et al. 2015, Diehl et al. 2017, Ismakov et al. 2017). Precise modulation of MEC activity has been linked to hippocampal remapping (Miao et al. 2015, Rueckemann et al. 2016, Kanter et al. 2017),

implying that rate redistribution in MEC cells could influence the firing rates of place cells. The weak rate remapping observed in mCA1 may have two sets of causes: first, the signal integration process in mCA1 differs from that in neighboring pCA1 and dCA1 (Masurkar et al. 2020), yet the linear gradients observed in other tasks seem to speak against this possibility; second, rate redistribution signals from MEC and LEC are mutually exclusive, suggesting a dynamic interplay between these inputs could influence neuronal outputs in CA1. We thus propose that the degree of rate remapping in CA1 is determined by the relative dominance of MEC and LEC inputs in a winner-take-all manner along the transverse axis. Neurons in pCA1 or dCA1, which predominantly receive input from either MEC or LEC, follow the strong input and exhibit pronounced rate remapping. In contrast, mCA1 neurons, which receive balanced MEC and LEC inputs, follow either input and thus display weak rate remapping.

LEC and PER inputs enhance representation of object location and identity in dCA1

The introduction of familiar objects in our experiments triggered a robust direct response in all CA1 subcompartments (Figure 4). Notably, the observed local changes in firing rate were not linked to exploratory behaviors around the objects (Figure S5K), suggesting a limited involvement of investigatory intention-modulated hippocampal neurons (Zeng et al. 2024). Both MEC and LEC include neurons that respond to the presence of discrete objects in the environment, albeit in different reference frames (Deshmukh et al. 2011, Wang et al. 2018, Hoydal et al. 2019). Additionally, PER, which projects to LEC and dCA1, contains object-responsive cells that are similar to those found in LEC (Burke et al. 2012, Deshmukh et al. 2012, Cappaert et al. 2015). Collectively, these observations suggest that CA1 neurons may integrate signals from MEC object-vector cells and LEC/PER object cells in their response to objects. For the novel-object task, while the role of PER in object-recognition memory is well-established, the contribution of the hippocampus and LEC to this process has been debated (Aggleton et al. 2020). Our results suggest that the enhanced local response to the novel object in dCA1 (Figure 6) could be attributed to modified inputs from neurons in LEC and PER that are specific to object identity (Deshmukh et al. 2011, Burke et al. 2012, Deshmukh et al. 2012, Huang et al. 2023). Although further research is needed to determine whether PER input alone is sufficient for novel object representation in CA1, our findings underscore a potential role for

dCA1 in object identity discrimination.

The object-relocation task, integral to spatial memory in rodents, prompted our hypothesis of enhanced neural activity in pCA1. Contrary to our expectations, the ensemble activity in response to object displacement was notably more pronounced in dCA1 (Figure 5). Moreover, neurons in mCA1 and dCA1 displayed a much stronger local response to the moved object than those in pCA1, echoing a prior finding (Vandrey et al. 2021). This robust local response in middle-to-distal CA1 suggests the influence of additional signals beyond those from MEC object-vector cells and LEC/PER object cells, which are known to respond to objects irrespective of their locations (Deshmukh et al. 2011, Burke et al. 2012, Deshmukh et al. 2012, Wang et al. 2018, Hoydal et al. 2019). Two potential sources of these signals include the object-trace cells within LEC, theorized to provide dCA1 with additional object-place information (Tsao et al. 2013), and the dCA1-projecting neurons in the subiculum, postulated to modulate place cell activity in response to object displacement (Sun et al. 2019). The recently identified subicular corner cells, which can generalize their firing to small objects placed in the arena regardless of location (Sun et al. 2024), may also play a role. Whether corner cells are the dCA1-projecting neurons in the subiculum remains to be determined, however.

Minimal contribution of CA3-CA2 inputs to transverse heterogeneity in CA1 function

While the entorhinal cortex significantly influences the transverse organization of CA1 function, the CA3 and CA2 regions also project substantially to hippocampal CA1. However, unlike the entorhinal inputs, the functional gradients within CA1 do not mirror the patterns observed along the CA3-CA2 axis. Neurons in pCA3 are characterized by sharp and confined place fields, strong rate remapping, and orthogonalized global remapping, in contrast to neurons in dCA3 and CA2, which exhibit reduced spatial modulation and lower sensitivity to environmental changes (Lee et al. 2015, Lu et al. 2015, Oliva et al. 2016, Deshmukh 2021). Interestingly, axons from dCA3 and CA2 preferentially innervate pCA1 neurons with enhanced spatial content and pronounced contextual responsiveness, while pCA3 heavily projects to dCA1, which is less spatially selective and less cue-sensitive (Cappaert et al. 2015). The discrepancy between the functional segregation and projection patterns of CA3-CA2 and CA1 calls for

further exploration. It is conceivable that the less differentiated signals from CA3 and CA2 may be overshadowed by the markedly distinct spatial and non-spatial inputs originating from the entorhinal cortex (Masurkar et al. 2017).

Limitations of the study

This study encountered two significant potential limitations. First, we recorded the neural activity of CA1 neurons using a hyperdrive with movable tetrodes, which limited our ability to monitor a substantial number of active neurons from various CA1 subregions simultaneously within individual rats. This constraint may have led to inter-animal variability, potentially confounding the interpretation of our results. Second, the complexity in CA1 extends to its radial organization into superficial and deep sublayers, each with distinct characteristics and functions (Soltesz et al. 2018). Our methodology, relying on tetrode recordings, did not allow us to differentiate between these sublayers. Future studies might take the advantage of two-photon calcium imaging and multi-shank probe recording to more extensively monitor neural activity within specific sublayers. Employing these advanced techniques could provide further insights into how laminar differences contribute to the heterogeneous functions observed along the CA1 proximo-distal axis.

Conclusion

The present study has delineated three distinct patterns of cue representation that are variably expressed from the proximal to the distal end of CA1. These findings prompt further inquiry into the causal dynamics linking selective inputs from specific upstream neuron populations and downstream representation of various information. Future theoretical and experimental endeavors should be directed towards understanding the precise mechanisms that govern these interactions, which are crucial for elucidating the neural basis of spatial navigation, episodic memory, and broader cognitive functions of the hippocampus.

Acknowledgements

The authors express gratitude to Yi-Qing Hui, Yi-Fan Ye, Chang-Lin Shen and Yi-Ling Shi for

their technical assistance in animal care, single-unit isolation and Matlab coding. They also thank Edvard Moser and May-Britt Moser for providing the Behavioral Neurology Toolbox and data from five animals, and Cheng Wang, Xin-Jian Li, Dun Mao, Hai-bing Xu, and Yong-Gang Yao, for their valuable suggestions on the manuscript.

Author Contributions

LL designed the experiments and analyses; YLD, SYH, XFG, JLL, CD, CJL, RZ, and XC performed the experiments; YLD, SYH, and LL conducted the analyses; YMS carried out the Bayesian decoding. YLD, LL, XC and BLS wrote the manuscript. All authors contributed to discussion and interpretation of the results.

Funding

This research was supported by the Science and Technology Innovation (STI) 2030-Major Projects (2022ZD0205000, to LL), the National Natural Science Foundation of China (31970963, to LL), Yunnan Province (202305AH340006, to LL) and the Yunnan Fundamental Research Projects (202101AT070289, to XC).

Conflict of interest statement

The authors declare no competing financial interests.

Code accessibility

All custom-written codes used in the analyses are available upon request.

Data availability

The data supporting the findings of this study are available from the corresponding author upon reasonable request.

Supplementary material

Supplementary material is accessible in the online version of this paper.

Figure legends

Figure 1. Recording sites and graded spatial modulation along the CA1 transverse axis

A. Left: schematic region of major recording sites, shown in red. Right: distribution of recording sites in CA1 along the proximo-distal axis. Red dots represent location of tetrode tips. Solid lines indicate borders between hippocampal regions; dashed lines separate proximal, middle, and distal bands of CA1. Numbers indicate normalized positions in CA1 along the transverse axis. FC: fasciola cinereum; SUB: subiculum. For a detailed view of recording sites per animal, refer to Figure S2.

B. Representative firing rate distribution maps (rate maps) from simultaneously recorded CA1 neurons in two separate experiments. Top: rate maps of pCA1 and mCA1 place cells from rat R0388. Gray lines indicate trajectories of the animal in each trial. Each cell's rate maps are arranged in rows, with the cell ID and peak firing rate for each trial indicated. Color is scaled to the maximum peak rate of four trials. B, black; W, white version of the same box. Bottom: rate maps of mCA1 and dCA1 place cells recorded from rat R0175. Note the confined firing fields in more proximally located place cells and the profound rate remapping in pCA1.

C–H. Violin plots displaying distributions of peak rate (**C**), number of place fields (**D**), theta modulation index (**E**), spatial information content (**F**), spatial coherence (**G**), and spatial stability (**H**) of place cells recorded in each CA1 band. Horizontal line indicates median, and thick vertical bar indicates interquartile range (IQR, 25%–75% percentile) of each subregion. *: $P < 0.05$; **: $P < 0.01$; ***: $P < 0.001$.

I–N. Scatter plots showing correlations between normalized recording position and peak rate (**I**), place field number (**J**), theta modulation (**K**), spatial information (**L**), coherence (**M**), and stability (**N**). Each cross represents averaged data of one single tetrode. Blue curve, linear regression; red curve, quadratic polynomial regression. Explained variances (R^2) are indicated with the same color code, with Pearson correlation coefficients and *P* values provided. pro., proximal end; dis., distal end.

1005 **Figure 2. Reverse J-shaped rate remapping to reversed wall color across CA1 subdivisions**

1006 **A.** Left: distributions of spatial correlation in CA1 subregions between matching (Same, mean
1007 of 2-3 trial pair and 1-4 trial pair) and color reversed (B vs W, mean of 1-3 trial pair and 2-4
1008 trial pair) conditions in the color-reversal task. Horizontal line indicates median, and thick
1009 vertical bar indicates IQR of each subregion. Right: box plots representing changes in SC
1010 between condition pairs, with outliers omitted. Place cells in mCA1 exhibited the least
1011 activity change. *: $P < 0.05$; ***: $P < 0.001$.

1012 **B.** Changes in spatial correlation between condition pairs as a function of tetrode position. Each
1013 cross corresponds to averaged data of one single tetrode. Blue curve, linear regression; red
1014 curve, quadratic polynomial regression. Explained variances (R^2) are indicated with the same
1015 color code. pro., proximal end; dis., distal end. p, proximal half; d, distal half.

1016 **C.** Similar to **A**, but shows change in rate difference across CA1 subdivisions. ***: $P < 0.001$.

1017 **D.** Similar to **B**, but illustrates the correlation between tetrode position and change in rate
1018 difference between condition pairs.

1019 **E.** Similar to **A**, but represents change in population vector correlation across CA1 bands. ***:
1020 $P < 0.001$.

1021 **F.** Heat maps showing population vector correlations (PVC) of all place cells recorded from
1022 each CA1 subregion between color conditions (top two rows), and changes of PVC between
1023 condition pairs (bottom row) in the color-reversal task. Bins in the heat map correspond to
1024 spatial bins in the rate maps. Color scales are indicated on the right of each row. Note that
1025 mCA1 exhibited the least activity changes. The reduction in PVC is stronger for spatial bins
1026 away from arena walls, where the color was manipulated.

1027

1028 **Figure 3. Graded global remapping along the proximo-distal axis in CA1**

1029 **A.** Simultaneously recorded CA1 neurons in two rats that exhibited global remapping in the
1030 two-room task. Left: rate maps of pCA1 and mCA1 place cells from rat R0172. Gray lines
1031 indicate trajectories of the animal in each trial. Each cell's rate maps are arranged in rows,
1032 with the cell ID and peak firing rate for each trial indicated. Color is scaled to the
1033 maximum peak rate of four trials. A, room A; B, room B. Right: rate maps of mCA1 and dCA1
1034 place cells recorded from rat R0175. Note the redistribution of firing locations between

1035 different rooms.

1036 **B.** Left: distribution of spatial correlation in CA1 subdivisions in the same room (Same, mean
1037 of 2-3 trial pair and 1-4 trial pair) and in different rooms (Rm A vs B, mean of 1-3 trial pair and
1038 2-4 trial pair) in the two-room task. Horizontal line indicates median, and thick vertical bar
1039 indicates IQR of each subregion. Right: change in SC between condition pairs, with outliers
1040 omitted. Place cells in pCA1 exhibited the strongest activity change. ***: $P < 0.001$.

1041 **C.** Correlation between tetrode position and change in SC between condition pairs. Each cross
1042 corresponds to averaged data of one single tetrode. Blue curve, linear regression; red curve,
1043 quadratic polynomial regression. Explained variance (R^2) is indicated with the same color code,
1044 with Pearson correlation coefficient and *P* value provided (54 tetrodes). pro., proximal
1045 end; dis., distal end.

1046 **D.** Similar to **B**, but shows change in rate difference across CA1 subdivisions. ***: $P < 0.001$.

1047 **E.** Similar to **C**, but illustrates the correlation between tetrode position and change in rate
1048 difference between condition pairs.

1049 **F.** Population vector correlations of all place cells recorded from each subregion in the same
1050 room (top row), between rooms (middle row), and changes in PVC between room pairs (bottom
1051 row) in the two-room task. Bins in the heat map correspond to spatial bins in the rate maps.
1052 Color scale is indicated at bottom right. Changes in PVC declined gradually from pCA1 to
1053 dCA1.

1054 **G.** Similar to **B**, but represents change in population vector correlation across CA1 bands. ***:
1055 $P < 0.001$.

1056

1057 **Figure 4. Reorganized CA1 population activity to familiar objects**

1058 **A.** Representative neurons from proximal, middle and distal bands of CA1, showing
1059 responses to familiar objects placed in the recording box. Maps for the same cell across
1060 four trials are arranged in rows, with animal and cell IDs indicated on the left. Color is
1061 scaled to the maximum peak rate of four trials. Text above each map indicates peak rate of that
1062 trial. Circles represent objects. Obj−, trial without objects; Obj+, trial with two familiar objects.
1063 Many neurons reorganized their firing activity in response to familiar objects. Note that
1064 in pCA1, neuron R0388-T09C1 showed rate redistribution in receptive field away from

1065 the familiar objects.

1066 **B.** Distribution of cells in response to object placement across three CA1 bands. Place cells
1067 with receptive fields relocated or appeared/disappeared were first identified, and then the
1068 remaining cells were grouped according to their rate difference scores: stable, RD ≤ 0.2, rate
1069 remapped, RD > 0.2. Numbers indicate active place cells in each category. Proportion of rate
1070 remapped cells: chi-square test, $\chi^2 = 1.512$, $P = 0.474$. Proportion of cells with receptive field
1071 appeared/disappeared: *: $P < 0.05$; **: $P < 0.01$.

1072 **C.** Distribution of population vector correlation in CA1 bands between trials with familiar
1073 objects (Same, trial 2 vs trial 3) and trials before and after object placement (+/− obj, trial 1 vs
1074 trial 2) for all spatial bins. Horizontal line indicates median, and thick vertical bar indicates IQR
1075 of each subregion. Boxplots on the right show changes in PVC between condition pairs, with
1076 outliers omitted. ***: $P < 0.001$.

1077 **D.** Population vector correlations of all place cells recorded from each subregion between trials
1078 with or without objects (top two rows), as well as changes in PVC between condition pairs
1079 (bottom row). Bins in the heat map correspond to spatial bins in the rate maps. Color scales are
1080 indicated on the right of each row. Small circles represent objects, large circles indicate the
1081 object region. Population activity reorganized most robustly in response to the object on the
1082 right (bins around left vs right object, Mann-Whitney U tests, all $P < 0.001$), likely due to
1083 frequent alterations to this object in the other two object-related tasks.

1084 **E–F.** Distributions of spatial correlation (top), rate difference (middle), and population vector
1085 correlation (bottom) within (**E**), and outside (**F**) the object region in CA1 bands between trials
1086 with familiar objects (Same) and trials before and after object placement (+/− obj). Horizontal
1087 line indicates median, and thick vertical bar indicates IQR of each subregion. Box plots show
1088 changes in activity measures between condition pairs, with outliers omitted. *: $P < 0.05$; **:
1089 $P < 0.01$; ***: $P < 0.001$.

1090

1091 **Figure 5. Minimum activity change to object relocation in pCA1**

1092 **A.** Representative neurons in the proximal, middle and distal bands of CA1 that responded to
1093 object displacement. Maps for the same cell across four trials are arranged in rows, with
1094 animal and cell IDs indicated on the left. Color is scaled to the maximum peak rate of four

trials. Text above each map indicates peak rate of that trial. Circles represent objects. Fam, objects in familiar locations; Reloc, right object relocated. New receptive fields emerged around the translocated object in many place cells.

B. Distribution of neurons in response to object translocation across three CA1 bands. Place cells with receptive fields relocated or appeared/disappeared were first identified, and then the remaining cells were grouped according to their rate difference scores: stable, RD ≤ 0.2, rate remapped, RD > 0.2. Numbers indicate active place cells in each category. Proportion of rate remapped cells: chi-square test, $\chi^2 = 3.624$, $P = 0.162$. Proportion of cells with receptive field appeared/disappeared: $\chi^2 = 14.257$, $P = 0.001$; post hoc tests, *: $P < 0.05$; ***: $P < 0.001$.

C. Left: distribution of spatial correlation in CA1 subregions between trials with relocated objects (Same, trial 2 vs trial 3) and trials before and after object relocation (Moved, trial 1 vs trial 2). Horizontal line indicates median, and thick vertical bar indicates IQR of each subregion. Right: change in SC between condition pairs, with outliers omitted. **: $P < 0.01$.

D. Correlation between recording position and changes in SC between condition pairs. Each cross corresponds to averaged data of one single tetrode. Blue curve, linear regression; red curve, quadratic polynomial regression. Explained variance (R^2) is indicated with the same color code, with Pearson correlation coefficient and P value provided. pro., proximal end; dis., distal end.

E. Similar to **C**, but shows changes in rate difference across CA1 subdivisions. *: $P < 0.05$.

F. Similar to **D**, but illustrates correlation between tetrode position and change in rate difference between condition pairs.

G. Similar to **C**, but represents change in population vector correlation across CA1 bands. ***: $P < 0.001$.

H. Left panel: population vector correlations of all place cells recorded from each subregion between trials (top two rows), as well as changes in PVC between trial pairs (bottom row) in the object-relocation task. Bins in the heat map correspond to spatial bins in the rate maps. Color scales are indicated on the right of each row. Small circles represent objects, large circles indicate the target region. Right panel: changes in PVC inside and outside the target region between trial pairs across CA1 bands, with outliers omitted. *: $P < 0.05$; ***: $P < 0.001$.

Figure 6. Elevated sensitivity to the novel object in dCA1

A. Representative neurons in the proximal, middle and distal bands of CA1 that remapped to the novel object. Maps of the same cell across four trials are arranged in rows, with animal and cell IDs indicated on the left. Color is scaled to the maximum peak rate of four trials. Text above each map indicates peak rate of that trial. Circle and star represent the familiar and novel object, respectively. Fam, trial with two familiar objects; Nov, trial with the right object replaced with a novel object. Some neurons exhibited local changes in firing rate around the novel object.

B. Distribution of neurons in response to the novel object across three CA1 bands. Place cells with receptive fields relocated or appeared/disappeared were first identified, and then the remaining cells were grouped according to their rate difference scores: stable, RD ≤ 0.2, rate remapped, RD > 0.2. Numbers indicate active place cells in each category. Proportion of rate remapped cells: chi-square test, $\chi^2 = 0.752$, $P = 0.685$. Proportion of cells with receptive field appeared/disappeared: $\chi^2 = 24.973$, $P < 0.001$; post hoc tests, *: $P < 0.05$; ***: $P < 0.001$.

C–**D.** Left: distributions of spatial correlation (**C**) and rate difference (**D**) in CA1 subregions between trials with a novel object (Same, trial 2 vs trial 3) and trials before and after object replacement (F/N obj, trial 1 vs trial 2) in the task. Horizontal line indicates median, and thick vertical bar indicates IQR of each subregion. Right: changes in activity measures between condition pairs, with outliers omitted. *: $P < 0.05$; ***: $P < 0.001$.

E. Correlation between tetrode position and change in rate difference between condition pairs. Each cross corresponds to averaged data of one single tetrode. Blue curve, linear regression; red curve, quadratic polynomial regression. Explained variance (R^2) is indicated with the same color code, with Pearson correlation coefficient and P value provided. pro., proximal end; dis., distal end.

F. Similar to **C**, but represents changes in population vector correlation across CA1 bands. **: $P < 0.01$; ***: $P < 0.001$.

G. Left panel: population vector correlations of all place cells recorded from each subregion between trials (top two rows), as well as changes in PVC between trial pairs (bottom row) in the novel-object task. Bins in the heat map correspond to spatial bins in the rate maps. Color scales are indicated on the right of each row. Small circle and star represent the familiar and novel object, respectively; large circle indicates region of the novel object. Right panel: changes

in PVC inside and outside region of interest between trial pairs across CA1 bands, with outliers omitted. n.s. not significant; ***: $P \leq 0.001$.

Figure S1, related to Methods. Design of behavioral paradigms and test environment.

A. Timeline of behavioral experiments.

B. Standard test environment in room A, with a black recording box and a white cue card. Decorations on the wall provide distal visual cues.

C. Test environment in room A, with the white recording box and a black cue card.

D. Standard test environment in room B, with a black recording box and a white cue card. The cue card in room B is positioned 90 degrees counterclockwise relative to room A, and the wall decorations exhibit a distinct pattern from those in room A.

E. Locations of the two familiar objects (black circles) in the object-placement task.

F. Objects (transparent glass bottles filled with white stones) in trials 2 and 3 of the object-placement task.

G. Design of the object-relocation task. Object on the right (dashed circle) was moved from quadrant 4 to quadrant 1 in trials 2 and 3.

H. Location of objects in trials 2 and 3 of the object-relocation task.

I. Design of the novel-object task. Object on the right (dashed circle) was replaced by a novel object (star) in trials 2 and 3.

J. Objects in trials 2 and 3 of the novel-object task. Note that in each experiment the object on the right was replaced by an object novel to the animal.

Figure S2, related to Figure 1. Recording sites in hippocampal CA1.

A. Schematic distribution of estimated recording region in each rat, with color code shown on the right. A, anterior; P, posterior; M: medial; L: lateral.

B–**P.** Nissl-stained coronal sections show recording sites from the fifteen animals recorded in this study. Red dots indicate recording sites. Numbers indicate normalized recording positions. Black and green arrowheads indicate CA1/subiculum and CA2/CA1 borders, respectively. Some tetrodes in R0089 and R0391 were lifted after recording thus recording sites were estimated by the extension of tetrode track. Scale bar: 1 mm.

1185 **Q–U.** Nissl-stained sagittal sections represent CA1 recording sites from the five animals
1186 reported previously (Lu et al. 2015).
1187
1188 **Figure S3, related to Figure 2 and 3. Extended analyses for the color-reversal task.**
1189 **A.** Rats' running speed in the color-reversal task. Trial 1: 14.86 (12.62–16.57) cm/s, trial 2:
1190 13.86 (11.12–15.35) cm/s, trial 3: 13.37 (10.78–14.90) cm/s, trial 4: 12.69 (10.58–14.44) cm/s.
1191 One-way repeated measures ANOVA, 178 experiments, trial: F (3) = 126.677, $P < 0.001$. **:
1192 $P < 0.01$; ***: $P < 0.001$.
1193 **B.** Distribution of pyramidal neurons across three CA1 bands. Inactive cells had firing rates
1194 lower than 0.1 Hz. Non-place cells refer to active cells with spatial information scores below
1195 the threshold of 0.9586 bit/spike. Numbers indicate cells in each category. Proportions of
1196 active cells: pCA1, 75.40%, mCA1, 72.12%, dCA1: 68.12%; chi-square test, $\chi^2 = 17.744$, $P <$
1197 0.001; Holm-Bonferroni post hoc tests, pCA1 vs mCA1, $P = 0.141$; mCA1 vs dCA1, $P = 0.064$;
1198 pCA1 vs dCA1, $P < 0.001$. Proportion of place cells: pCA1, 65.72%, mCA1, 63.94%, dCA1,
1199 56.44%, $\chi^2 = 27.893$, $P < 0.001$; post hoc tests, ***: $P < 0.001$.
1200 **C.** i. Distribution of shuffled spatial information content based on 100 permutations per cell for
1201 all CA1 pyramidal neurons. ii – iv. Distribution of spatial information content in pCA1 (ii),
1202 mCA1 (iii) and dCA1 (iv). Red line indicates the 95th percentile value (0.9586 bit/spike) for the
1203 distribution based on all permutations.
1204 **D.** Example of active cells, aligned according to their spatial information scores. Gray lines
1205 indicate trajectories of the animal. Red dots represent individual spikes of each example
1206 cell. Color of the rate map is scaled to the peak rate. Spatial information scores are indicated
1207 on the top. Red line indicates the threshold for place cells.
1208 **E–H.** Distributions of mean firing rate (**E**), size of place field (**F**), Phase locking to theta (**G**),
1209 and spatial information rate (**H**) of place cells recorded in each CA1 band. Horizontal line
1210 indicates median, and thick vertical bar indicates IQR of each subregion. Mean firing rate:
1211 pCA1: 0.360 (0.175–0.706) Hz, mCA1: 0.360 (0.183–0.671) Hz, dCA1: 0.328 (0.155–0.634)
1212 Hz; Kruskal-Wallis test, 2,622 cells, H = 3.695, $P = 0.158$. Place field size: pCA1: 0.126 (0.083–
1213 0.189) m^2, mCA1: 0.128 (0.084–0.191) m^2, dCA1: 0.131 (0.085–0.199) m^2; H = 0.476, $P =$
1214 0.788, 2,622 cells. Theta phase locking: pCA1: 0.170 (0.122–0.232), mCA1: 0.148 (0.105–

0.205), dCA1: 0.154 (0.113–0.203); H = 25.867, $P < 0.001$, 2,254 cells. Spatial information rate: pCA1: 0.798 (0.476–1.393) bit/second, mCA1: 0.770 (0.453–1.265) bit/second, dCA1: 0.706 (0.406–1.190) bit/second; H = 14.646, $P = 0.001$, 2,622 cells. Holm-Bonferroni post hoc tests, n.s.: not significant; **: $P < 0.01$; ***: $P < 0.001$.

I. Spatial tuning of place cells recorded from distant proximo-distal locations (normalized distance > 0.1) on the same coronal section. This subset of data compares place cells from disto-anterior (daCA1), central (cCA1), and proximo-posterior portions (ppCA1) of a CA1 transverse block, and exhibits the same trend as the pooled data. Top row: comparison of place cells from ppCA1 and cCA1. Peak firing rate: ppCA1, 4.137 (2.504–6.338) Hz, cCA1, 2.887 (1.839–5.289) Hz; Mann-Whitney U test, 77 cells, z = 918, $P = 0.066$. Place field number: ppCA1, 1.00 (1.00–1.33), cCA1, 1.00 (1.00–1.50); z = 764, $P = 0.774$. Spatial information rate: ppCA1, 0.608 (0.441–1.142) bit/second, cCA1, 0.399 (0.253–0.713) bit/second; z = 972, $P = 0.017$. Coherence: ppCA1, 0.584 (0.476–0.683), cCA1, 0.555 (0.397–0.624); z = 876, $P = 0.159$. Stability: ppCA1, 0.668 (0.589–0.761), cCA1, 0.623 (0.401–0.710); z = 957, $P = 0.025$. Bottom row: comparison of cCA1 and daCA1 place cells. Peak firing rate: cCA1, 3.825 (3.009–5.443) Hz, daCA1, 3.465 (2.101–6.585) Hz; Mann-Whitney U test, 113 cells, z = 1730, $P = 0.421$. Place field number: cCA1, 1.00 (1.00–1.25), daCA1, 1.25 (1.00–1.50); z = 1178, $P = 0.010$. Spatial information rate: cCA1, 0.652 (0.469–0.978) bit/second, daCA1, 0.470 (0.291–1.069) bit/second; z = 1885, $P = 0.090$. Coherence: cCA1, 0.650 (0.562–0.725), daCA1, 0.593 (0.428–0.682); z = 1989, $P = 0.022$. Stability: cCA1, 0.711 (0.618–0.798), daCA1, 0.582 (0.394–0.739); z = 2137, $P = 0.001$.

J. Decoding accuracy of animal's position as a function of number of cells (N) included in calculation. Data were generated by taking a random subset of N cells from a total population of over 60 simultaneously recorded place cells (rat R0391). The mean accuracy values averaged from 10-fold cross-validations for the 60 loops are represented. The decoding accuracy reached 0.8 when 30 cells were included.

K. Position decoding accuracy (mean ± SEM) for simultaneously recorded pCA1/mCA1 and mCA1/dCA1 data sets. Black dots represent data from individual predictions. The three experiments with more than 30 simultaneously recorded place cells in both bands are shown. Downsampling was applied to equalize cell numbers. R0388: pCA1: 0.880 ± 0.026; mCA1:

1245 0.821 ± 0.035; paired t-test, t = 3.131, P = 0.012, 10 calculations. R0391-1: mCA1: 0.828 ±
1246 0.031; dCA1: 0.617 ± 0.069; t = 4.587, P = 0.001. R0391-2: mCA1: 0.841 ± 0.026; dCA1:
1247 0.782 ± 0.030; t = 2.149, P = 0.060. *: $P < 0.05$; ***: $P \leq 0.001$.

1248 **L–M.** Correlations between normalized recording position and mean vector length of theta
1249 phase locking (**L**), and spatial information rate (**M**). Data from 110 and 113 tetrodes were
1250 included for analysis of theta phase locking and spatial information rate, respectively. Each
1251 cross corresponds to averaged data of one single tetrode. Blue curve, linear regression; red
1252 curve, quadratic polynomial regression. Explained variances (R^2) are indicated with the same
1253 color code, with Pearson correlation coefficients and P values provided. pro., proximal
1254 end; dis., distal end.

1255 **N.** Spatial correlations of CA1 place maps between test conditions recorded from each rat in
1256 the color-reversal task. Black box, correlation between matching conditions (Same, mean of 2-
1257 3 trial pair and 1-4 trial pair); green box, correlation between black and white colors (B vs W,
1258 mean of 1-3 trial pair and 2-4 trial pair). Numbers on the top indicate place cells recorded from
1259 each animal. All the animals exhibited rate remapping as the medians of their correlation scores
1260 were above 0.5, indicated by the horizontal dashed line.

1261 **O.** Distribution of rate remapped cells between black and white color conditions across three
1262 CA1 bands. Stable cells had rate difference scores no higher than 0.2. Moderately remapped
1263 cells had rate difference scores between 0.2 and 0.5. Strongly remapped cells had rate difference
1264 scores higher than 0.5. Numbers indicate active place cells in each category. Proportions of
1265 stable cells: pCA1, 32.89%, mCA1, 43.71%, dCA1: 37.52%; chi-square test, $\chi^2 = 23.409$, $P <$
1266 0.001; Holm-Bonferroni post hoc tests, pCA1 vs mCA1, $P < 0.001$; mCA1 vs dCA1, $P = 0.030$;
1267 pCA1 vs dCA1, $P = 0.166$. Proportion of moderately remapped cells: pCA1, 43.08%, mCA1,
1268 43.71%, dCA1, 43.79%, $\chi^2 = 0.109$, $P = 0.951$. Proportion of strongly remapped cells: pCA1,
1269 24.03%, mCA1, 12.58%, dCA1, 18.69%, $\chi^2 = 41.214$, $P < 0.001$; post hoc tests, *: $P < 0.05$,
1270 **: $P < 0.01$, ***: $P < 0.001$.

1271 **P.** Representative rate maps from a place cell (T08C1 of R0175 in Figure 1B) with two
1272 individually remapped firing fields in black (top) and white (bottom) conditions. Numbers on
1273 top indicate overall firing rate in the trial. The two fields remapped independently in reverse
1274 directions so that the changes in firing rate were neutralized with the measure of rate difference

(RD) but not with rate difference by field (RD_f).

Q. Comparison of RD and RD_f across CA1 subregions. Although RD_f were significantly higher than RD between conditions (Same: two-way repeated measures ANOVA, measure: F (1, 2619) = 388.282, $P < 0.001$; band: F (2, 2619) = 14.263, $P < 0.001$; measure × band: F (2, 2619) = 6.952, $P = 0.001$; B vs W: measure: F (1, 2619) = 533.091, $P < 0.001$; band: F (2, 2619) = 37.929, $P < 0.001$; measure × band: F (2, 2619) = 5.481, $P = 0.004$), elevations in RD_f between black and white conditions were marginal (measure: F (1, 2619) = 36.765, $P < 0.001$; band: F (2, 2619) = 63.833, $P < 0.001$; measure × band: F (2, 2619) = 11.101, $P < 0.001$).

R. Left: distributions of rate difference by field in CA1 subregions between matching (Same) and color reversed (B vs W) conditions in the color-reversal task. Horizontal line indicates median, and thick vertical bar indicates IQR of each subregion. A pattern similar to change in overall rate difference was observed with the measure of RD_f (two-way repeated measures ANOVA, color: F (1, 2619) = 397.067, P < 0.001; band: F (2, 2619) = 23.230, P < 0.001; color × band: F (2, 2619) = 67.922, P < 0.001). Right: changes in RD_f between condition pairs, with outliers omitted. pCA1: 0.028 (−0.003–0.166), mCA1: 0.003 (−0.008–0.056), dCA1: 0.006 (−0.006–0.067); Kruskal-Wallis test, 2,622 cells, H = 65.433, $P < 0.001$, Holm-Bonferroni post hoc tests, ***: $P < 0.001$.

S. Changes in rate difference by field between condition pairs as a function of tetrode position. Each cross corresponds to averaged data of one single tetrode. Blue curve, linear regression; red curve, quadratic polynomial regression. Explained variances (R^2) are indicated with the same color code. pro., proximal end; dis., distal end. p, proximal half; d, distal half. Change in RD_f was significantly correlated with tetrode location in the proximal half of CA1, but not in the distal half (proximal: r = −0.435, $P < 0.001$; distal: r = 0.106, $P = 0.462$).

T. Left panel: PVCs of CA1 subregions between neighboring trials in the color-reversal task. A notable effect of hysteresis was observed between trials 3 and 4. Right panel: degrees of hysteresis reflected by changes in PVC between trial pairs with reversed colors, with outliers omitted. pCA1, 0.096 (0.069–0.121), mCA1, 0.058 (0.043–0.075), dCA1, 0.082 (0.063–0.107); Kruskal-Wallis test, 1,200 bins, H = 221.582, $P < 0.001$. Holm-Bonferroni post hoc tests, ***: $P < 0.001$.

U. Context decoding accuracy (mean ± SEM) for simultaneously recorded pCA1/mCA1 and

mCA1/dCA1 data sets. Black dots represent data from individual predictions. The three experiments with more than 30 simultaneously recorded place cells in both bands are shown. Downsampling was applied to equalize cell numbers. R0388: pCA1, 0.744 ± 0.007, mCA1, 0.797 ± 0.006; paired t-test, t = 6.714, $P < 0.001$, 10 calculations. R0391-1: mCA1, 0.699 ± 0.006, dCA1, 0.508 ± 0.014; t = 14.98, $P < 0.001$. R0391-2: mCA1, 0.834 ± 0.003, dCA1, 0.678 ± 0.008); t = 27.95, $P < 0.001$. ***: $P < 0.001$.

Figure S4, related to Figure 4. Extended analyses for the two-room task.

A. Spatial correlations of CA1 place maps between test conditions recorded from each rat in the two-room task. Black box, correlation in the same room (Same, mean of 2-3 trial pair and 1-4 trial pair); cyan and rose box, correlation in different rooms (Rm A vs B, mean of 1-3 trial pair and 2-4 trial pair). Numbers on the top indicate place cells recorded from each animal. Thirteen (cyan) and six (rose) animals exhibited global and rate remapping, as the medians of their spatial correlation scores were below and above the threshold of 0.5, respectively.

B–C. Representative rate maps of simultaneously recorded CA1 neurons in two rats that exhibited rate remapping in the two-room task. **B**: rate maps of pCA1 and mCA1 place cells from rat R0388. Gray lines indicate trajectories of the animal in each trial. Each cell's rate maps are arranged in rows, with the cell ID and peak firing rate for each trial indicated. Color is scaled to the maximum peak rate of four trials. A, room A; B, room B. **C**: rate maps of mCA1 and dCA1 place cells from rat R0391.

D–G. Left: distributions of spatial correlation (**D**), rate difference (**E**), rate difference by field (**F**), and population vector correlation (**G**) in CA1 subregions in the same room (Same) and different rooms (Rm A vs B) in the two-room task. A total of 158, 248 and 67 place cells were recorded from proximal, middle and distal CA1, respectively. Horizontal line indicates median, and thick vertical bar indicates IQR of each subregion. Right: changes in activity measures between condition pairs, with outliers omitted. These results aligned with findings in the color-reversal task. SC: two-way repeated measures ANOVA, room, F (1, 470) = 107.984, $P < 0.001$; band, F (2, 470) = 14.731, $P < 0.001$; room × band, F (2, 470) = 6.736, $P = 0.001$; decrease in SC: Kruskal-Wallis test, 463 cells, H = 9.459, $P = 0.009$. RD: room, F (1, 470) = 94.727, $P < 0.001$; band, F (2, 470) = 17.948, $P < 0.001$; room × band, F (2, 470) = 13.614, P

< 0.001; increase in RD: H = 26.795, $P < 0.001$. RD_f: room, F (1, 470) = 105.158, $P < 0.001$; band, F (2, 470) = 25.979, $P < 0.001$; room × band, F (2, 470) = 7.123, $P = 0.001$; increase in RD_f: H = 8.305, $P = 0.016$. PVC: room, F (1, 1197) = 3370.376, $P < 0.001$; band, F (2, 1197) = 140.276, $P < 0.001$; room × band, F (2, 1197) = 373.718, $P < 0.001$; decrease in PVC: H = 430.146, $P < 0.001$, 1,200 bins. Place cells in proximal CA1 exhibited the strongest activity change (Holm-Bonferroni post hoc tests). *: $P < 0.05$; ***: $P < 0.001$.

H. Running speed for the thirteen rats exhibiting global remapping in the two-room task. Trial 1: 15.14 (11.46–17.85) cm/s, trial 2: 13.17 (11.12–16.38) cm/s, trial 3: 13.64 (11.61–16.17) cm/s, trial 4: 13.67 (11.35–15.91) cm/s. One-way repeated measures ANOVA, 28 experiments, F (3) = 8.540, $P < 0.001$. *: $P < 0.05$; ***: $P < 0.001$.

I. Distribution of pyramidal neurons across three CA1 bands, from the thirteen rats exhibiting global remapping in the two-room task. Inactive cells had firing rates lower than 0.1 Hz. Non-place cells refer to active cells with spatial information scores below the threshold of 0.9586 bit/spike. Numbers indicate cells in each category. Proportions of active cells: pCA1, 80.00%, mCA1, 80.00%, dCA1: 77.54%; chi-square test, $\chi^2 = 1.033$, $P = 0.598$. Proportion of place cells: pCA1, 73.53%, mCA1, 67.66%, dCA1, 61.75%, $\chi^2 = 13.437$, $P = 0.001$; Holm-Bonferroni post hoc tests, ***, $P < 0.001$.

J–O. Distributions of mean firing rate (**J**), peak firing rate (**K**), theta modulation (**L**), spatial information rate (**M**), coherence (**N**), and stability (**O**) of place cells recorded in each CA1 subregion. Horizontal line indicates median, and thick vertical bar indicates IQR of each subregion. Mean rate: pCA1, 0.365 (0.190–0.688) Hz, mCA1, 0.276 (0.138–0.577) Hz, dCA1, 0.241 (0.122–0.464) Hz; Kruskal-Wallis test, H = 19.564, $P < 0.001$, 761 cells. Peak rate: pCA1, 6.409 (3.641–9.652) Hz, mCA1, 4.885 (3.226–7.503) Hz, dCA1, 4.173 (2.667–6.725) Hz; H = 36.510, $P < 0.001$. Theta modulation: pCA1, 0.497 (0.419–0.601), mCA1, 0.436 (0.315–0.567), dCA1, 0.433 (0.312–0.547); H = 28.744, $P < 0.001$. Spatial information rate: pCA1, 1.005 (0.586–1.567) bit/second, mCA1, 0.709 (0.449–1.231) bit/second, dCA1, 0.632 (0.390–1.022) bit/second; H = 43.428, $P < 0.001$. Coherence: pCA1, 0.682 (0.583–0.764), mCA1, 0.634 (0.528–0.731), dCA1, 0.602 (0.487–0.700); H = 43.056, $P < 0.001$. Stability: pCA1, 0.771 (0.640–0.860), mCA1, 0.652 (0.520–0.788), dCA1, 0.616 (0.485–0.765); H = 71.884, $P < 0.001$. Holm-Bonferroni post hoc tests, *: $P < 0.05$; **: $P < 0.01$; ***: $P < 0.001$.

P–R. Correlations between normalized recording position and spatial information rate (**P**), coherence (**Q**), and stability (**R**). Data from 54 tetrodes. Each cross corresponds to averaged data of one single tetrode. Blue curve, linear regression; red curve, quadratic polynomial regression. Explained variances (R^2) are indicated with the same color code, with Pearson correlation coefficients and *P* values provided. pro., proximal end; dis., distal end.

S. Distribution of active place cells in the two-room task, with cell numbers indicated. Proportions of cells that were active in both rooms: pCA1, 62.80%; mCA1, 66.04%; dCA1, 63.64%, chi-square test, $\chi^2 = 0.456$, $P = 0.796$.

T. i. Distributions of spatial correlation between rate maps for the same cell in different rooms (solid curve) and randomly selected rate maps from different cells (10,000 permutations, dashed curve). ii – iv. Same distributions as in (i), but for individual CA1 subregions. Colored bars show the distribution of spatial correlation between rooms; black trace represents the distribution of permutations. Dashed vertical line indicates the 95th percentile value of the latter distribution (chance level). Inter-room correlations tended to skew toward higher values than expected from the chance distribution from pCA1 to dCA1. The proportion of observations above the chance level is indicated on the right. pCA1, 10.21%, mCA1, 12.74%, dCA1, 17.01%, all significantly higher than chance (5%, all $P \leq 0.001$, binomial tests). There is a considerable trend toward significance from pCA1 to dCA1, chi-square test, $\chi^2 = 5.595$, $P = 0.063$.

U–V. Left: distributions of spatial correlation (**U**) and rate difference (**V**) in CA1 subregions in the same room (Same) and different rooms (Rm A vs B) in the two-room task. Horizontal line indicates median, and thick vertical bar indicates IQR of each subregion. Numbers on top indicate cell number after downsampling. Similar results were obtained with downsampled data. SC: two-way repeated measures ANOVA, room: F (1, 457) = 770.784, $P < 0.001$; band: F (2, 457) = 5.549, $P = 0.005$; room × band: F (2, 457) = 13.179, $P < 0.001$. RD: room: F (1, 457) = 288.640, $P < 0.001$; band: F (2, 457) = 0.785, $P = 0.457$; room × band: F (2, 457) = 15.156, $P < 0.001$. Right: changes in activity measures between condition pairs, with outliers omitted. SC: pCA1, 0.473 (0.260–0.724), mCA1, 0.354 (0.153–0.526), dCA1, 0.283 (0.078–0.552); Kruskal-Wallis test, 460 cells, H = 22.741, $P < 0.001$. RD: pCA1, 0.273 (0.062–0.519), mCA1, 0.082 (0–0.351), dCA1, 0.092 (0–0.274); H = 25.854, $P < 0.001$. Holm-Bonferroni post hoc tests, ***: $P \leq 0.001$.

W. Left panel: population vector correlations of CA1 subregions between neighboring trials in the two-room task. Right panel: hysteresis between trial pairs in different rooms, with outliers omitted. Carry over effect was minimum across rooms: pCA1, 0.020 (−0.018–0.056), mCA1, 0.030 (−0.039–0.076), dCA1, −0.012 (−0.046–0.042). H = 35.139, $P < 0.001$, Kruskal-Wallis test, 1,200 bins. Holm-Bonferroni post hoc tests, ***: $P < 0.001$.

Figure S5, related to Figure 5. Extended analyses for the object-placement task.

A. Spatial correlations of CA1 place maps between different trial pairs recorded from each rat in the object-placement task. Black box, correlation between trials with familiar objects (Same, trial 2 vs trial 3); dark green box, correlation between trials before and after object placement (+/− obj, trial 1 vs trial 2). Numbers on the top indicate place cells recorded from each animal. Most of the animals showed changes in spatial correlation between trial pairs.

B. Rats' running speed in the object-placement task. Trial 1: 14.24 (11.63–16.10) cm/s, trial 2: 13.21 (11.20–15.03) cm/s, trial 3: 12.46 (10.73–14.26) cm/s, trial 4: 12.79 (10.78–14.61) cm/s. One-way repeated measures ANOVA, 65 experiments, F (3) = 30.283, $P < 0.001$. ***: $P < 0.001$.

C. Occupation time (OT) in the object region before and after object placement for each rat. The mean OT was close to an unbiased distribution of 0.2 (proportional to region size) and remained unchanged (before: 0.205 ± 0.003; after: 0.204 ± 0.007), paired t-test, 14 rats, t = 0.222, $P = 0.828$). n.s., not significant.

D. Normalized changes in LFP power in object region after object placement. LFP power fluctuated in theta (7–10 Hz) and low-beta (12–20 Hz) range, which might reflect animals' exploratory behavior. Vertical dashed line indicates 8.5 Hz. No difference is observed across CA1 subregions (Kruskal-Wallis tests with multi-comparison corrected, all $Q > 0.05$). n.s., not significant.

E. Distribution of pyramidal neurons across three CA1 bands, based on data from fourteen rats tested in the task. Inactive cells had firing rates lower than 0.1 Hz. Non-place cells refer to active cells with spatial information scores below the threshold of 0.9586 bit/spike. Numbers indicate cells in each category. Proportions of active cells: pCA1, 76.83%, mCA1, 71.61%, dCA1: 70.74%; chi-square test, $\chi^2 = 6.449$, $P = 0.040$; Holm-Bonferroni post hoc tests, pCA1

vs mCA1, $P = 0.096$; mCA1 vs dCA1, $P = 1.000$; pCA1 vs dCA1, $P = 0.041$. Proportion of place cells: pCA1, 70.98%, mCA1, 63.72%, dCA1, 63.43%, $\chi^2 = 9.514$, $P = 0.009$; post hoc tests, *, $P < 0.05$.

F. Population vector correlations of CA1 subregions between neighboring trials in the object-placement task. A notable effect of hysteresis was observed between trials 3 and 4.

G. Distribution of cells in response to object placement across three CA1 bands, using a similar criterion to the color-reversal task. Stable cells had rate difference scores no higher than 0.2. Moderately remapped cells had rate difference scores between 0.2 and 0.5. Strongly remapped cells had rate difference scores higher than 0.5. Numbers indicate active place cells in each category. Proportions of stable cells: pCA1, 41.47%, mCA1, 49.46%, dCA1: 38.98%; chi-square test, $\chi^2 = 16.752$, $P < 0.001$; Holm-Bonferroni post hoc tests, pCA1 vs mCA1, $P = 0.045$; mCA1 vs dCA1, $P < 0.001$; pCA1 vs dCA1, $P = 1.000$ (*: $P < 0.05$; ***: $P < 0.001$). Proportion of moderately remapped cells: pCA1, 36.47%, mCA1, 32.56%, dCA1, 34.74%, $\chi^2 = 1.745$, $P = 0.417$. Proportion of strongly remapped cells: pCA1, 20.00%, mCA1, 17.17%, dCA1, 24.67%, $\chi^2 = 12.291$, $P = 0.002$; post hoc tests, pCA1 vs mCA1, $P = 0.805$; mCA1 vs dCA1, $P = 0.002$; pCA1 vs dCA1, $P = 0.297$. Proportion of cells with relocated field(s): pCA1, 2.06%, mCA1, 0.82%, dCA1, 1.61%, Fisher's exact test, FI = 3.357, $P = 0.186$.

H. Distribution of spatial correlation (left panel), and rate difference (right panel) in CA1 bands between trials with familiar objects (Same) and trials before and after object placement (+/− obj) for all spatial bins. Horizontal line indicates median, and thick vertical bar indicates IQR of each subregion. Box plots on the right show changes in SC and RD between condition pairs, with outliers omitted. SC: left: two-way repeated measures ANOVA, object: F (1, 1756) = 301.628, $P < 0.001$; band: F (2, 1756) = 47.330, $P < 0.001$; object × band: F (2, 1756) = 0.513, $P = 0.599$. RD: left: object: F (1, 1756) = 211.814, $P < 0.001$; band: F (2, 1756) = 16.119, $P < 0.001$; object × band: F (2, 1756) = 3.875, $P = 0.021$; right: pCA1, 0.081 (−0.019–0.259), mCA1, 0.054 (−0.065–0.227), dCA1, 0.053 (−0.084–0.267), Kruskal-Wallis test, 1,759 cells, H = 7.088, $P = 0.029$; Holm-Bonferroni post hoc tests, *: $P < 0.05$.

I. Context decoding accuracy (mean ± SEM) for simultaneously recorded pCA1/mCA1 and mCA1/dCA1 data sets. Black dots represent data from individual predictions. The three experiments with more than 30 simultaneously recorded place cells in both bands are shown.

Downsampling was applied to equalize cell numbers. R0388: pCA1, 0.905 ± 0.004, mCA1, 0.910 ± 0.004; paired t-test, t = 1.043, $P = 0.324$, 10 calculations. R0175: mCA1, 0.850 ± 0.002, dCA1, 0.597 ± 0.010; t = 23.75, $P < 0.001$. R0391: mCA1, 0.487 ± 0.014, dCA1, 0.258 ± 0.011; t = 14.29, $P < 0.001$. n.s., not significant; ***: $P < 0.001$.

J. Similar to **H**, but show changes outside the object region for rate difference across CA1 subdivisions. Numbers on top indicate cell number after downsampling. Similar results were obtained with downsampled data. Two-way repeated measures ANOVA, object: F (1, 1047) = 97.502, $P < 0.001$; band: F (2, 1047) = 9.498, $P < 0.001$; object × band: F (2, 1047) = 5.863, $P = 0.003$; changes in RD: pCA1, 0.080 (−0.037–0.275), mCA1, 0.033 (−0.056–0.171), dCA1, 0.063 (−0.110–0. 226); Kruskal-Wallis test, 1,050 cells, H = 10.359, $P = 0.006$. Holm-Bonferroni post hoc tests, *: $P < 0.05$.

K. Out-region changes in rate difference between trial pairs, analyzed separately according to OT change in the object region, with outliers omitted. Low Δ OT: below median of OT change (OT_{trial2} - OT_{trial1}); High Δ OT: above median of OT change. No difference was observed in each CA1 subregion. Mann-Whitney U tests, all $P > 0.05$.

L. Changes in population vector correlation for bins outside the target region in the three object related tasks, with outliers omitted. Patterns of PVC change along the proximo-distal axis were different across tasks. The novel-object task displayed the minimum activity change. The object-placement task showed a reverse J-shaped activity change whereas the object-relocation task exhibited a gradual increase in activity change along the transverse axis. Two-way ANOVA, task: F (2, 2991) = 173.446, $P < 0.001$; band: F (2, 2991) = 10.196, $P < 0.001$; task × band: F (4, 2991) = 21.331, $P < 0.001$.

Figure S6, related to Figure 6. Extended analyses for the object-relocation task.

A. Spatial correlations of CA1 place maps between different trial pairs recorded from each rat in the object-relocation task. Black box, correlation between trials with objects in familiar locations (Same, trial 2 vs trial 3); dark blue box, correlation between trials before and after object relocation (Moved, trial 1 vs trial 2). Numbers on the top indicate place cells recorded from each animal. Most of the animals showed changes in spatial correlation between trial pairs.

B. Rats' running speed in the object-relocation task. Trial 1: 12.72 (11.57–15.60) cm/s, trial 2:

12.86 (10.43–14.84) cm/s, trial 3: 11.85 (10.22–14.36) cm/s, trial 4: 11.23 (10.42–13.61) cm/s. One-way repeated measures ANOVA, 59 experiments, F (3) = 29.795, $P < 0.001$. **: $P < 0.01$; ***: $P < 0.001$.

C. Discrimination index (DI) between the two objects before and after object relocation for each rat. The mean DI was close to unbiased exploration and remained largely unchanged (before: −0.007 ± 0.015; after: 0.014 ± 0.027, paired t-test, 14 rats, t = −0.716, $P = 0.487$). n.s., not significant.

D. Normalized changes in LFP power around the target object after object relocation. LFP power fluctuated slightly in theta (7–10 Hz) and low-beta (12–20 Hz) range, which might align with animals' exploratory behavior. Vertical dashed line indicates 8.5 Hz. Short horizontal bars indicate significant regional differences (Kruskal-Wallis tests with multi-comparison corrected, 8–9 Hz, 14–15 Hz, both $Q < 0.001$).

E. Distribution of pyramidal neurons across three CA1 bands, based on data from fourteen rats tested in the task. Inactive cells had firing rates lower than 0.1 Hz. Non-place cells refer to active cells with spatial information scores below the threshold of 0.9586 bit/spike. Numbers indicate cells in each category. Proportions of active cells: pCA1, 75.61%, mCA1, 71.02%, dCA1: 65.16%; chi-square test, $\chi^2 = 16.157$, $P < 0.001$; Holm-Bonferroni post hoc tests, pCA1 vs mCA1, $P = 0.343$; mCA1 vs dCA1, $P = 0.015$; pCA1 vs dCA1, $P = 0.001$. Proportion of place cells: pCA1, 69.21%, mCA1, 66.19%, dCA1, 58.16%, $\chi^2 = 20.656$, $P < 0.001$; post hoc tests, ***, $P < 0.001$.

F. Population vector correlations of CA1 subregions between neighboring trials in the object-relocation task. A notable effect of hysteresis was observed between trials 3 and 4.

G. Changes in spatial correlation (left panel) and rate difference (right panel) between trial pairs, analyzed separately according to DI change in the object region, with outliers omitted. Low Δ DI: below median of DI change (DI_{trial2} - DI_{trial1}); High Δ DI: above median of DI change. No difference was observed in each CA1 subregion. Mann-Whitney U tests, all $P > 0.05$.

H–I. Left: distributions of spatial correlation (**H**) and rate difference (**I**) in CA1 subregions between trials with translocated objects (Same) and trials before and after object translocation (Moved) in the task. Horizontal line indicates median, and thick vertical bar indicates IQR of each subregion. Numbers on top indicate cell number after downsampling. Similar results were

obtained with downsampled data. SC: two-way repeated measures ANOVA, relocation: F (1, 644) = 98.022, $P < 0.001$; band: F (2, 644) = 17.428, $P < 0.001$; relocation × band: F (2, 644) = 6.236, $P = 0.002$. RD: relocation: F (1, 644) = 108.721, $P < 0.001$; band: F (2, 644) = 14.763, $P < 0.001$; relocation × band: F (2, 644) = 3.018, $P = 0.050$. Right: changes in activity measures between condition pairs, with outliers omitted. SC: pCA1, 0.024 (−0.0260.121), mCA1, 0.033 (−0.030–0.144), dCA1, 0.085 (−0.021–0.232); Kruskal-Wallis test, 647 cells, H = 15.013, $P = 0.001$. RD: pCA1, 0.044 (−0.072–0.204), mCA1, 0.055 (−0.042–0.215), dCA1, 0.116 (−0.050–0. 317); H = 7.038, $P = 0.030$. Holm-Bonferroni post hoc tests, *: P < 0.05; ***, $P < 0.001$.

J. Similar to **H**, but shows changes in rate difference by field across CA1 subregions. Left: two-way repeated measures ANOVA, relocation: F (1, 1483) = 183.183, $P < 0.001$; band: F (2, 1483) = 26.108, $P < 0.001$; relocation × band: F (2, 1483) = 1.724, $P = 0.179$. Right: pCA1, 0.043 (−0.040–0.246), mCA1, 0.070 (−0.041–0.231), dCA1, 0.111 (−0.072–0.344); Kruskal-Wallis test, 1,486 cells, H = 4.467, $P = 0.107$.

K. Correlation between normalized recording position and changes in rate difference by field between condition pairs. Each cross corresponds to averaged data of one single tetrode. Blue curve, linear regression; red curve, quadratic polynomial regression. Explained variance (R^2) is indicated with the same color code, with Pearson correlation coefficient and P value provided. pro., proximal end; dis., distal end.

L. Context decoding accuracy (mean ± SEM) for simultaneously recorded pCA1/mCA1 and mCA1/dCA1 data sets. Black dots represent data from individual predictions. The three experiments with more than 30 simultaneously recorded place cells in both bands are shown. Downsampling was applied to equalize cell numbers. R0388: pCA1, 0.682 ± 0.013, mCA1, 0.623 ± 0.011; paired t-test, t = 4.731, $P = 0.001$, 10 calculations. R0391-1: mCA1, 0.631 ± 0.007, dCA1, 0.443 ± 0.006; t = 27.39, $P < 0.001$. R0391-2: mCA1, 0.439 ± 0.012, dCA1, 0.186 ± 0.022; t = 10.44, $P < 0.001$. ***: $P \leq 0.001$.

M. Correlations of population vectors within (left panel) and outside (right panel) the target region, between trials with objects in familiar locations (Same) and trials before and after object translocation (Moved). Horizontal line indicates median, and thick vertical bar indicates IQR of each subregion. PVC within object region: two-way repeated measures ANOVA, relocation:

F (1, 237) = 1556.030, $P < 0.001$; band: F (2, 237) = 13.251, $P < 0.001$; relocation × band: F (2, 237) = 108.992, $P < 0.001$. PVC outside object region: relocation: F (1, 957) = 1085.693, $P < 0.001$; band: F (2, 957) = 37.345, $P < 0.001$; relocation × band: F (2, 957) = 7.099, $P = 0.001$.

Figure S7, related to Figure 7. Extended analyses for the novel-object task.

A. Spatial correlations of CA1 place maps between different trial pairs recorded from each rat in the novel-object task. Black box, correlation between trials with familiar objects (Same, trial 2 vs trial 3); dark red box, correlation between trials before and after object replacement (F/N obj, trial 1 vs trial 2). Numbers on the top indicate place cells recorded from each animal. Changes in spatial correlation were marginal in all rats.

B. Rats' running speed in the novel-object task. Trial 1: 13.422 (11.34–15.20) cm/s, trial 2: 12.84 (10.42–14.74) cm/s, trial 3: 12.72 (10.54–14.16) cm/s, trial 4: 12.40 (10.30–13.60) cm/s. One-way repeated measures ANOVA, 54 experiments, F (3) = 28.126, $P < 0.001$. **: $P < 0.01$; ***: $P < 0.001$.

C. Discrimination index (DI) between the two objects before and after object replacement for each rat. The mean DI was close to unbiased exploration and remained unchanged (before: −0.011 ± 0.016; after: 0.004 ± 0.014, paired t-test, 14 rats, t = −1.203, $P = 0.250$). n.s., not significant.

D. Normalized changes in LFP power around the target object after object relocation. Vertical dashed line indicates 8.5 Hz. Short horizontal bars indicate significant regional differences (Kruskal-Wallis tests with multi-comparison corrected, 5-6 Hz, $Q = 0.015$; 12–13 Hz, $Q = 0.030$; 14–15 Hz, $Q = 0.040$).

E. Distribution of pyramidal neurons across three CA1 bands, based on data from fourteen rats tested in the task. Inactive cells had firing rates lower than 0.1 Hz. Non-place cells refer to active cells with spatial information scores below the threshold of 0.9586 bit/spike. Numbers indicate cells in each category. Proportions of active cells: pCA1, 76.08%, mCA1, 71.92%, dCA1: 70.75%; chi-square test, $\chi^2 = 4.279$, $P = 0.117$. Proportion of place cells: pCA1, 67.43%, mCA1, 66.28%, dCA1, 64.40%, $\chi^2 = 1.379$, $P = 0.505$. n.s., not significant.

F. Population vector correlations of CA1 subregions between neighboring trials in the novel-object task. A notable effect of hysteresis was observed between trials 3 and 4.

G. Changes in spatial correlation (left panel) and rate difference (right panel) between trial pairs, analyzed separately according to DI change in the object region, with outliers omitted. Low Δ DI: below median of DI change; High Δ DI: above median of DI change. No difference was observed in each CA1 subregion. Mann-Whitney U tests, all $P > 0.05$.

H–I. Left: distributions of spatial correlation (**H**) and rate difference (**I**) in CA1 subregions between trials with a novel object (Same) and trials before and after object replacement (F/N obj) in the task. Horizontal line indicates median, and thick vertical bar indicates IQR of each subregion. Numbers on top indicate cell number after downsampling. Similar results were obtained with downsampled data. SC: two-way repeated measures ANOVA, novelty: F (1, 871) = 62.904, $P < 0.001$; band: F (2, 871) = 7.921, $P < 0.001$; novelty × band: F (2, 871) = 2.329, $P = 0.098$. RD: novelty: F (1, 871) = 42.556, $P < 0.001$; band: F (2, 871) = 4.742, $P = 0.009$; novelty × band: F (2, 871) = 4.637, $P = 0.010$. Right: changes in activity measures between condition pairs, with outliers omitted. SC: pCA1, 0.016 (−0.034–0.076), mCA1, 0.018 (−0.041–0.102), dCA1, 0.040 (−0.018–0.178); Kruskal-Wallis test, 874 cells, H = 9.841, $P = 0.007$. RD: pCA1, 0.008 (−0.101–0.120), mCA1, 0.056 (−0.058–0.166), dCA1, 0.050 (−0.0890.212); H = 10.954, $P = 0.004$. Holm-Bonferroni post hoc tests, *: P < 0.05.

J. Similar to **H**, but shows changes in rate difference by field across CA1 subregions. Left: two-way repeated measures ANOVA, novelty: F (1, 1448) = 63.640, $P < 0.001$; band: F (2, 1448) = 28.451, $P < 0.001$; novelty × band: F (2, 1448) = 6.456, $P = 0.002$. Right: pCA1, 0.002 (−0.095–0.115), mCA1, 0.029 (−0.080–0.175), dCA1, 0.072 (−0.068–0.260); Kruskal-Wallis test, 1,451 cells, H = 18.747, $P < 0.001$. Holm-Bonferroni post hoc tests, *: P < 0.05; ***: P < 0.001.

K. Correlation between normalized recording position and changes in rate difference by field between condition pairs. Each cross corresponds to averaged data of one single tetrode. Blue curve, linear regression; red curve, quadratic polynomial regression. Explained variance (R^2) is indicated with the same color code, with Pearson correlation coefficient and P value provided. pro., proximal end; dis., distal end.

L. Context decoding accuracy (mean ± SEM) for the data set with simultaneously recorded mCA1/dCA1 neurons. Black dots represent data from individual predictions. Only one experiment had more than 30 simultaneously recorded place cells in both CA1 subregions. Downsampling was applied to equalize cell numbers. R0391: mCA1, 0.816 ± 0.003, dCA1,

0.321 ± 0.014; paired t-test, t = 38.89, $P < 0.001$, 10 calculations. ***: $P < 0.001$.

M. Correlations of population vectors within (left panel) and outside (right panel) the target region, between trials with familiar objects (Same, trial 2 vs trial 3) and trials before and after object replacement (F/N obj, trial 1 vs trial 2). Horizontal line indicates median, and thick vertical bar indicates IQR of each subregion. PVC within object region: two-way repeated measures ANOVA, novelty: F (1, 117) = 236.315, $P < 0.001$; band: F (2, 117) = 39.954, $P < 0.001$; novelty × band: F (2, 117) = 58.668, $P < 0.001$. PVC outside object region: novelty: F (1, 1077) = 1253.175, $P < 0.001$; band: F (2, 1077) = 231.473, $P < 0.001$; novelty × band: F (2, 1077) = 4.168, $P = 0.016$.

Figure S8. Summary of the findings and afferent connections that varied along the CA1 transverse axis.

Top: the three distinct patterns of cue representation that varied along the CA1 proximo-distal axis. Left, the descending gradient in spatial information processing, evidenced by a linear decrease in the sharpness and confinement of place fields in open space, and a progressive decline in the orthogonalization of place maps between distinct spatial environments, from the proximal to the distal end of CA1. Middle, the reverse J-shaped pattern in response to non-spatial context changes, such as color-reversed arena walls and the introduction of familiar objects into the recording box, expressed by a minimum change in firing rate near the midpoint of the transverse axis, with progressively enhanced overall rate redistribution towards both ends of the same axis. Right, the ascending gradient in representation of local object features, characterized by an increase in local reorganization of neuronal activity to changes in the position or identity of an object placed in the arena, from the proximal to the distal end of CA1. Bottom: projection profiles to CA1 within the hippocampal region. Neurons in layer III of medial and lateral divisions of the entorhinal cortex (MEC and LEC) selectively terminate their axons onto cells in proximal and distal portions of CA1, respectively. These two parts of CA1 also receive preferential inputs from distal and proximal CA3. Moreover, CA2 fibers innervate more neurons in proximal CA1, and the subiculum (SUB) contains neurons that back-project to distal CA1. The perirhinal cortex (PER) receives inputs from SUB and projects to LEC and distal CA1.

References

Aggleton J. P., Nelson A. J. D. (2020). "Distributed interactive brain circuits for object-in-place memory: A place for time?"[J] *Brain Neurosci Adv* **4**: 2398212820933471.

Beer Z., Vavra P., Atucha E., Rentzing K., Heinze H. J., Sauvage M. M. (2018). "The memory for time and space differentially engages the proximal and distal parts of the hippocampal subfields CA1 and CA3."[J] *PLoS Biol* **16**(8): e2006100.

Bokil H., Andrews P., Kulkarni J. E., Mehta S., Mitra P. P. (2010). "Chronux: a platform for analyzing neural signals."[J] *J Neurosci Methods* **192**(1): 146-151.

Burke S. N., Maurer A. P., Hartzell A. L., Nematollahi S., Uprety A., Wallace J. L., Barnes C. A. (2012). "Representation of three-dimensional objects by the rat perirhinal cortex."[J] *Hippocampus* **22**(10): 2032-2044.

Burke S. N., Maurer A. P., Nematollahi S., Uprety A. R., Wallace J. L., Barnes C. A. (2011). "The influence of objects on place field expression and size in distal hippocampal CA1."[J] *Hippocampus* **21**(7): 783-801.

Cacucci F., Lever C., Wills T. J., Burgess N., O'Keefe J. (2004). "Theta-modulated place-by-direction cells in the hippocampal formation in the rat."[J] *J Neurosci* **24**(38): 8265-8277.

Canto C. B., Wouterlood F. G., Witter M. P. (2008). "What does the anatomical organization of the entorhinal cortex tell us?"[J] *Neural Plast* **2008**: 381243.

Cappaert N. L., van Strien N. M., Witter M. P. (2015). Hippocampal Formation. *The Rat Nervous System*[M]. G. Paxinos, Academic Press,**:** 511-573.

Colgin L. L., Moser E. I., Moser M. B. (2008). "Understanding memory through hippocampal remapping."[J] *Trends Neurosci* **31**(9): 469-477.

Deshmukh S. S. (2021). "Distal CA1 Maintains a More Coherent Spatial Representation than Proximal CA1 When Local and Global Cues Conflict."[J] *J Neurosci* **41**(47): 9767-9781.

Deshmukh S. S., Johnson J. L., Knierim J. J. (2012). "Perirhinal cortex represents nonspatial, but not spatial, information in rats foraging in the presence of objects: comparison with lateral entorhinal cortex."[J] *Hippocampus* **22**(10): 2045-2058.

Deshmukh S. S., Knierim J. J. (2011). "Representation of non-spatial and spatial information

in the lateral entorhinal cortex."[J] *Front Behav Neurosci* **5**: 69.

Deshmukh S. S., Knierim J. J. (2013). "Influence of local objects on hippocampal representations: Landmark vectors and memory."[J] *Hippocampus* **23**(4): 253-267.

Diehl G. W., Hon O. J., Leutgeb S., Leutgeb J. K. (2017). "Grid and Nongrid Cells in Medial Entorhinal Cortex Represent Spatial Location and Environmental Features with Complementary Coding Schemes."[J] *Neuron* **94**(1): 83-92 e86.

Flasbeck V., Atucha E., Nakamura N. H., Yoshida M., Sauvage M. M. (2018). "Spatial information is preferentially processed by the distal part of CA3: Implication for memory retrieval."[J] *Behav Brain Res* **354**: 31-38.

Fyhn M., Hafting T., Treves A., Moser M. B., Moser E. I. (2007). "Hippocampal remapping and grid realignment in entorhinal cortex."[J] *Nature* **446**(7132): 190-194.

Fyhn M., Molden S., Witter M. P., Moser E. I., Moser M. B. (2004). "Spatial representation in the entorhinal cortex."[J] *Science* **305**(5688): 1258-1264.

Glaser J. I., Benjamin A. S., Chowdhury R. H., Perich M. G., Miller L. E., Kording K. P. (2020). "Machine Learning for Neural Decoding."[J] *eNeuro* **7**(4).

Hafting T., Fyhn M., Molden S., Moser M. B., Moser E. I. (2005). "Microstructure of a spatial map in the entorhinal cortex."[J] *Nature* **436**(7052): 801-806.

Hargreaves E. L., Rao G., Lee I., Knierim J. J. (2005). "Major dissociation between medial and lateral entorhinal input to dorsal hippocampus."[J] *Science* **308**(5729): 1792-1794.

Hartzell A. L., Burke S. N., Hoang L. T., Lister J. P., Rodriguez C. N., Barnes C. A. (2013). "Transcription of the immediate-early gene Arc in CA1 of the hippocampus reveals activity differences along the proximodistal axis that are attenuated by advanced age."[J] *J Neurosci* **33**(8): 3424-3433.

Henriksen E. J., Colgin L. L., Barnes C. A., Witter M. P., Moser M. B., Moser E. I. (2010). "Spatial representation along the proximodistal axis of CA1."[J] *Neuron* **68**(1): 127-137.

Hoydal O. A., Skytoen E. R., Andersson S. O., Moser M. B., Moser E. I. (2019). "Object-vector coding in the medial entorhinal cortex."[J] *Nature* **568**(7752): 400-404.

Huang X., Schlesiger M. I., Barriuso-Ortega I., Leibold C., MacLaren D. A. A., Bieber N., Monyer H. (2023). "Distinct spatial maps and multiple object codes in the lateral entorhinal cortex."[J] *Neuron* **111**(19): 3068-3083 e3067.

Igarashi K. M., Lu L., Colgin L. L., Moser M. B., Moser E. I. (2014). "Coordination of entorhinal-hippocampal ensemble activity during associative learning."[J] *Nature* **510**(7503): 143-147.

Ismakov R., Barak O., Jeffery K., Derdikman D. (2017). "Grid Cells Encode Local Positional Information."[J] *Curr Biol* **27**(15): 2337-2343 e2333.

Ito H. T., Schuman E. M. (2012). "Functional division of hippocampal area CA1 via modulatory gating of entorhinal cortical inputs."[J] *Hippocampus* **22**(2): 372-387.

Kanter B. R., Lykken C. M., Avesar D., Weible A., Dickinson J., Dunn B., Borgesius N. Z., Roudi Y., Kentros C. G. (2017). "A Novel Mechanism for the Grid-to-Place Cell Transformation Revealed by Transgenic Depolarization of Medial Entorhinal Cortex Layer II."[J] *Neuron* **93**(6): 1480-1492 e1486.

Knierim J. J., Neunuebel J. P., Deshmukh S. S. (2014). "Functional correlates of the lateral and medial entorhinal cortex: objects, path integration and local-global reference frames."[J] *Philos Trans R Soc Lond B Biol Sci* **369**(1635): 20130369.

Kropff E., Carmichael J. E., Moser M. B., Moser E. I. (2015). "Speed cells in the medial entorhinal cortex."[J] *Nature* **523**(7561): 419-424.

Latuske P., Kornienko O., Kohler L., Allen K. (2017). "Hippocampal Remapping and Its Entorhinal Origin."[J] *Front Behav Neurosci* **11**: 253.

Lee H., Wang C., Deshmukh S. S., Knierim J. J. (2015). "Neural population evidence of functional heterogeneity along the CA3 transverse axis: pattern completion versus pattern separation."[J] *Neuron* **87**(5): 1093-1105.

Leitner F. C., Melzer S., Lutcke H., Pinna R., Seeburg P. H., Helmchen F., Monyer H. (2016). "Spatially segregated feedforward and feedback neurons support differential odor processing in the lateral entorhinal cortex."[J] *Nat Neurosci* **19**(7): 935-944.

Leutgeb S., Leutgeb J. K., Barnes C. A., Moser E. I., McNaughton B. L., Moser M. B. (2005). "Independent codes for spatial and episodic memory in hippocampal neuronal ensembles."[J] *Science* **309**(5734): 619-623.

Leutgeb S., Leutgeb J. K., Treves A., Moser M. B., Moser E. I. (2004). "Distinct ensemble codes in hippocampal areas CA3 and CA1."[J] *Science* **305**(5688): 1295-1298.

Li Y., Xu J., Liu Y., Zhu J., Liu N., Zeng W., Huang N., Rasch M. J., Jiang H., Gu X., Li X.,

Luo M., Li C., Teng J., Chen J., Zeng S., Lin L., Zhang X. (2017). "A distinct entorhinal cortex to hippocampal CA1 direct circuit for olfactory associative learning."[J] *Nat Neurosci* **20**(4): 559-570.

Long J. L., Lu L. (2022). "Dynamic coding in the hippocampus during navigation."[J] *Zool Res* **43**(6): 1023-1025.

Lu L., Igarashi K. M., Witter M. P., Moser E. I., Moser M. B. (2015). "Topography of place maps along the CA3-to-CA2 axis of the hippocampus."[J] *Neuron* **87**(5): 1078-1092.

Lu L., Leutgeb J. K., Tsao A., Henriksen E. J., Leutgeb S., Barnes C. A., Witter M. P., Moser M. B., Moser E. I. (2013). "Impaired hippocampal rate coding after lesions of the lateral entorhinal cortex."[J] *Nat Neurosci* **16**(8): 1085-1093.

Lu L., Popeney B., Dickman J. D., Angelaki D. E. (2018). "Construction of an Improved Multi-Tetrode Hyperdrive for Large-Scale Neural Recording in Behaving Rats."[J] *J Vis Exp*(135).

Marozzi E., Ginzberg L. L., Alenda A., Jeffery K. J. (2015). "Purely Translational Realignment in Grid Cell Firing Patterns Following Nonmetric Context Change."[J] *Cereb Cortex* **25**(11): 4619-4627.

Masurkar A. V., Srinivas K. V., Brann D. H., Warren R., Lowes D. C., Siegelbaum S. A. (2017). "Medial and lateral entorhinal cortex differentially excite deep versus superficial CA1 pyramidal neurons."[J] *Cell Rep* **18**(1): 148-160.

Masurkar A. V., Tian C., Warren R., Reyes I., Lowes D. C., Brann D. H., Siegelbaum S. A. (2020). "Postsynaptic integrative properties of dorsal CA1 pyramidal neuron subpopulations."[J] *J Neurophysiol* **123**(3): 980-992.

Miao C., Cao Q., Ito H. T., Yamahachi H., Witter M. P., Moser M. B., Moser E. I. (2015). "Hippocampal Remapping after Partial Inactivation of the Medial Entorhinal Cortex."[J] *Neuron* **88**(3): 590-603.

Nagelhus A., Andersson S. O., Cogno S. G., Moser E. I., Moser M. B. (2023). "Object-centered population coding in CA1 of the hippocampus."[J] *Neuron* **111**(13): 2091-2104 e2014.

Nakamura N. H., Flasbeck V., Maingret N., Kitsukawa T., Sauvage M. M. (2013). "Proximodistal segregation of nonspatial information in CA3: preferential recruitment of a proximal CA3-distal CA1 network in nonspatial recognition memory."[J] *J Neurosci* **33**(28): 11506-11514.

Nakazawa Y., Pevzner A., Tanaka K. Z., Wiltgen B. J. (2016). "Memory retrieval along the proximodistal axis of CA1."[J] *Hippocampus* **26**(9): 1140-1148.

Nilssen E. S., Doan T. P., Nigro M. J., Ohara S., Witter M. P. (2019). "Neurons and networks in the entorhinal cortex: A reappraisal of the lateral and medial entorhinal subdivisions mediating parallel cortical pathways."[J] *Hippocampus* **29**(12): 1238-1254.

Oliva A., Fernandez-Ruiz A., Buzsaki G., Berenyi A. (2016). "Spatial coding and physiological properties of hippocampal neurons in the Cornu Ammonis subregions."[J] *Hippocampus* **26**(12): 1593-1607.

Renno-Costa C., Lisman J. E., Verschure P. F. (2010). "The mechanism of rate remapping in the dentate gyrus."[J] *Neuron* **68**(6): 1051-1058.

Rueckemann J. W., DiMauro A. J., Rangel L. M., Han X., Boyden E. S., Eichenbaum H. (2016). "Transient optogenetic inactivation of the medial entorhinal cortex biases the active population of hippocampal neurons."[J] *Hippocampus* **26**(2): 246-260.

Sargolini F., Fyhn M., Hafting T., McNaughton B. L., Witter M. P., Moser M. B., Moser E. I. (2006). "Conjunctive representation of position, direction, and velocity in entorhinal cortex."[J] *Science* **312**(5774): 758-762.

Skaggs W. E., McNaughton B. L., Wilson M. A., Barnes C. A. (1996). "Theta phase precession in hippocampal neuronal populations and the compression of temporal sequences."[J] *Hippocampus* **6**(2): 149-172.

Solstad T., Boccara C. N., Kropff E., Moser M. B., Moser E. I. (2008). "Representation of geometric borders in the entorhinal cortex."[J] *Science* **322**(5909): 1865-1868.

Soltesz I., Losonczy A. (2018). "CA1 pyramidal cell diversity enabling parallel information processing in the hippocampus."[J] *Nat Neurosci* **21**(4): 484-493.

Sugar J., Moser M. B. (2019). "Episodic memory: Neuronal codes for what, where, and when."[J] *Hippocampus* **29**(12): 1190-1205.

Sun Y., Jin S., Lin X., Chen L., Qiao X., Jiang L., Zhou P., Johnston K. G., Golshani P., Nie Q., Holmes T. C., Nitz D. A., Xu X. (2019). "CA1-projecting subiculum neurons facilitate object-place learning."[J] *Nat Neurosci* **22**(11): 1857-1870.

Sun Y., Nitz D. A., Xu X., Giocomo L. M. (2024). "Subicular neurons encode concave and convex geometries."[J] *Nature* **627**(8005): 821-829.

Tsao A., Moser M. B., Moser E. I. (2013). "Traces of experience in the lateral entorhinal cortex."[J] *Curr Biol* **23**(5): 399-405.

Tsao A., Sugar J., Lu L., Wang C., Knierim J. J., Moser M. B., Moser E. I. (2018). "Integrating time from experience in the lateral entorhinal cortex."[J] *Nature* **561**(7721): 57-62.

Tukker J. J., Beed P., Brecht M., Kempter R., Moser E. I., Schmitz D. (2022). "Microcircuits for spatial coding in the medial entorhinal cortex."[J] *Physiol Rev* **102**(2): 653-688.

Vandrey B., Duncan S., Ainge J. A. (2021). "Object and object-memory representations across the proximodistal axis of CA1."[J] *Hippocampus* **31**(8): 881-896.

Wang C., Chen X., Lee H., Deshmukh S. S., Yoganarasimha D., Savelli F., Knierim J. J. (2018). "Egocentric coding of external items in the lateral entorhinal cortex."[J] *Science* **362**(6417): 945-949.

Zeng Y. F., Yang K. X., Cui Y. L., Zhu X. N., Li R., Zhang H. Q., Wu D. C., Stevens R. C., Hu J., Zhou N. (2024). "Conjunctive encoding of exploratory intentions and spatial information in the hippocampus."[J] *Nature Communications* **15**(1).

Figure 1

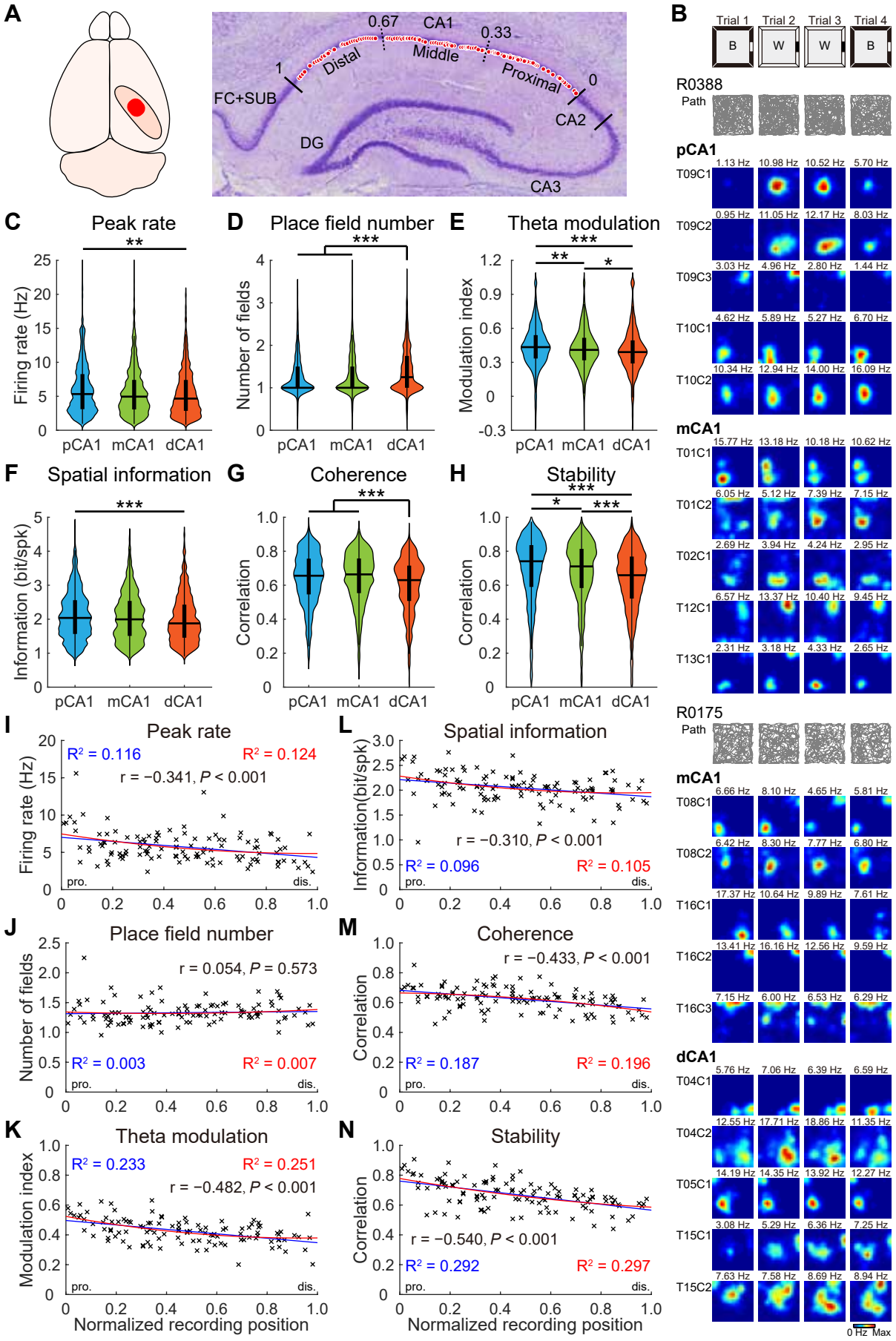
A
0.67
CA1
0.33
1
Distal
Middle
Proximal
0
FC+SUB
CA2
DG
CA3
B
Trial 1
Trial 2
Trial 3
Trial 4
B
W
W
B
R0388
Path
pCA1
T09C1
T09C2
T09C3
T10C1
T10C2
mCA1
T01C1
T01C2
T02C1
T12C1
T13C1
R0175
Path
mCA1
T08C1
T08C2
T16C1
T16C2
T16C3
dCA1
T04C1
T04C2
T05C1
T15C1
T15C2
0 Hz
Max
C
Peak rate
Firing rate (Hz)
pCA1
mCA1
dCA1
D
Place field number
Number of fields
E
Theta modulation
Modulation index
F
Spatial information
Information (bit/spk)
G
Coherence
Correlation
H
Stability
Correlation
I
Peak rate
Firing rate (Hz)
R² = 0.116
R² = 0.124
r = −0.341, P < 0.001
pro.
dis.
L
Spatial information
Information(bit/spk)
r = −0.310, P < 0.001
R² = 0.096
R² = 0.105
J
Place field number
Number of fields
r = 0.054, P = 0.573
R² = 0.003
R² = 0.007
M
Coherence
Correlation
r = −0.433, P < 0.001
R² = 0.187
R² = 0.196
K
Theta modulation
Modulation index
R² = 0.233
R² = 0.251
r = −0.482, P < 0.001
N
Stability
Correlation
r = −0.540, P < 0.001
R² = 0.292
R² = 0.297
Normalized recording position
Normalized recording position

Figure 2

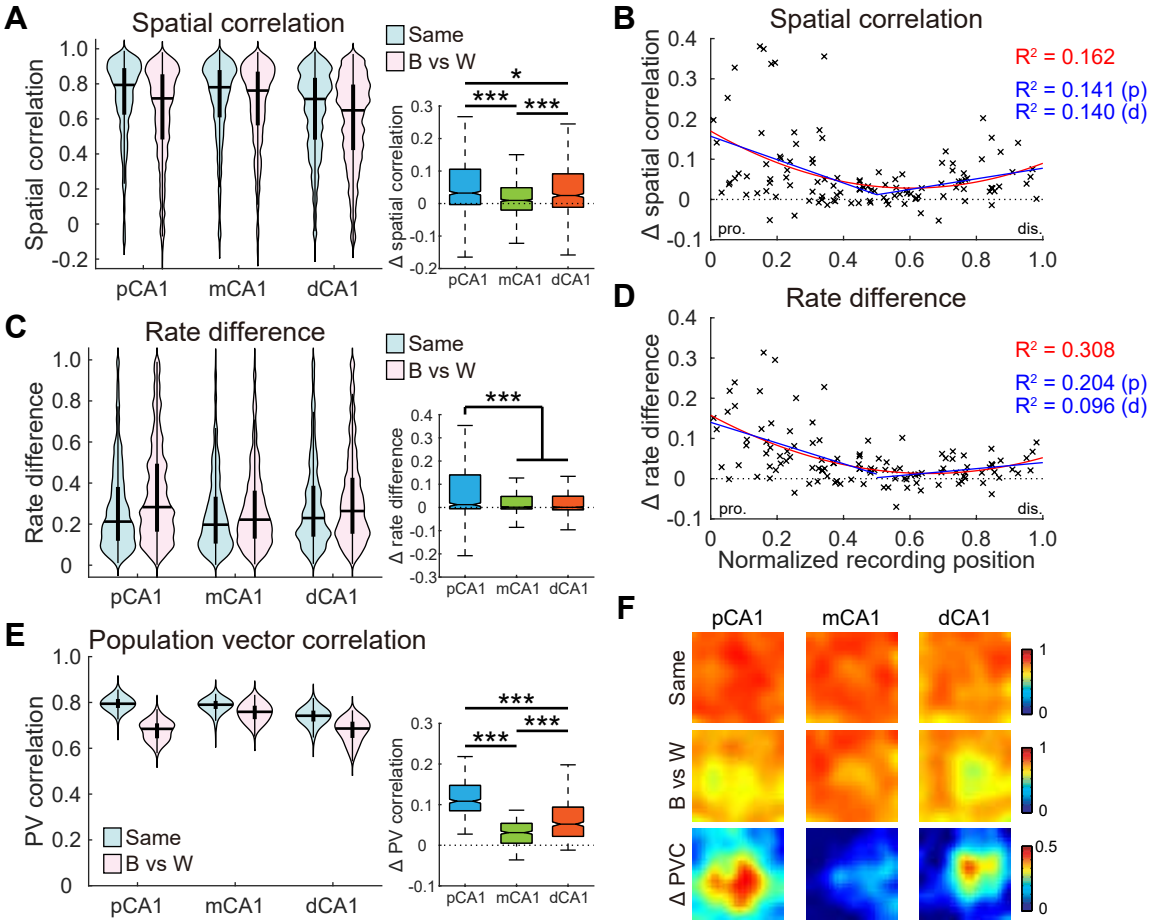
A
Spatial correlation
Spatial correlation
Same
B vs W
Δ spatial correlation
pCA1
mCA1
dCA1
B
Spatial correlation
Δ spatial correlation
R² = 0.162
R² = 0.141 (p)
R² = 0.140 (d)
pro.
dis.
C
Rate difference
Rate difference
Δ rate difference
D
Rate difference
Δ rate difference
R² = 0.308
R² = 0.204 (p)
R² = 0.096 (d)
Normalized recording position
E
Population vector correlation
PV correlation
Δ PV correlation
F
Same
B vs W
Δ PVC

Figure 3

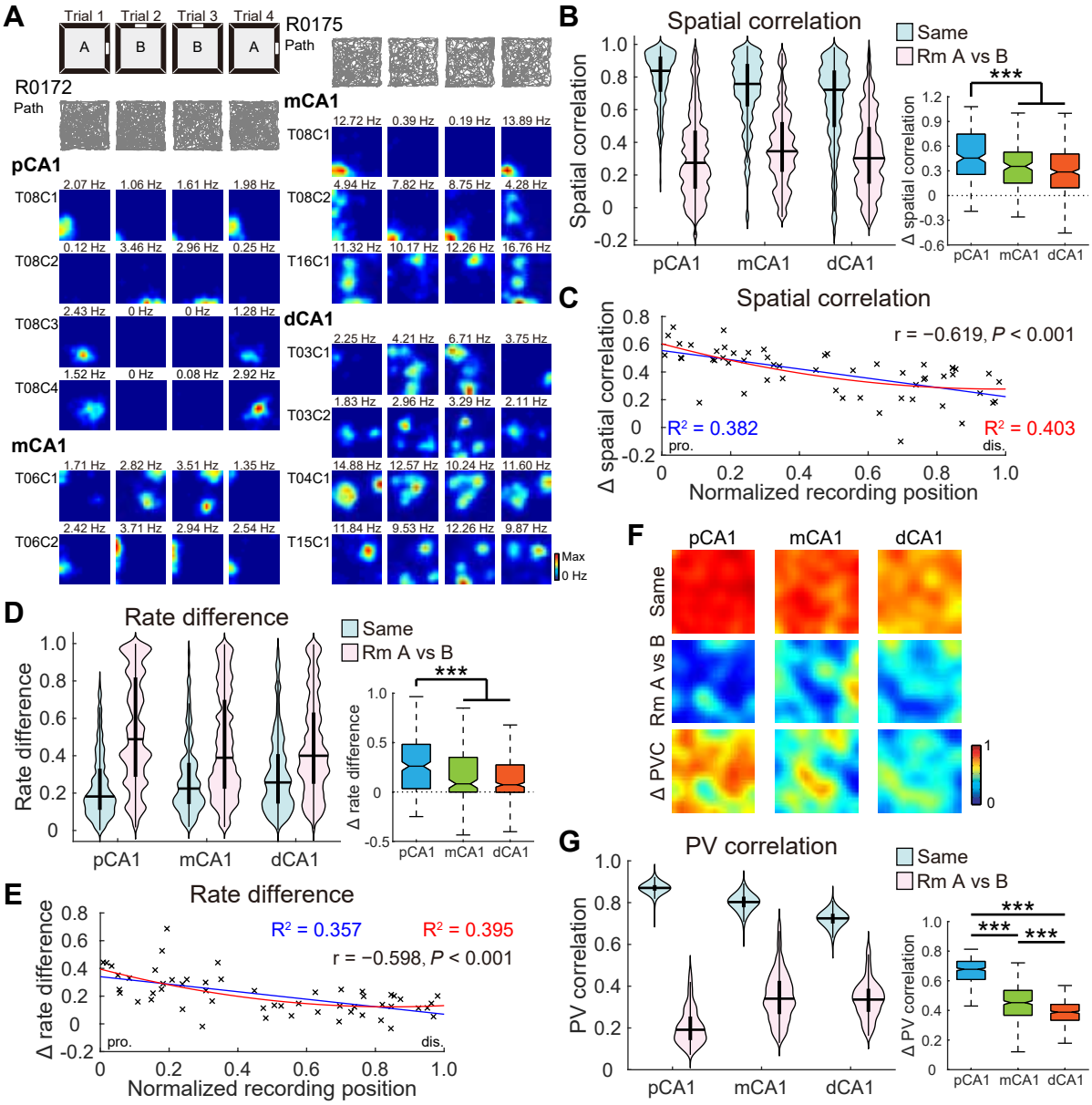
A
Trial 1
Trial 2
Trial 3
Trial 4
R0172
Path
R0175
Path
pCA1
mCA1
dCA1
T08C1
T08C2
T08C3
T08C4
T06C1
T06C2
T16C1
T03C1
T03C2
T04C1
T15C1
Max
0 Hz
B
Spatial correlation
Same
Rm A vs B
Δ spatial correlation
pCA1
mCA1
dCA1
C
Spatial correlation
r = −0.619, P < 0.001
R² = 0.382
R² = 0.403
pro.
dis.
Normalized recording position
D
Rate difference
Δ rate difference
E
Rate difference
R² = 0.357
R² = 0.395
r = −0.598, P < 0.001
F
Δ PVC
G
PV correlation
Δ PV correlation

Figure 4

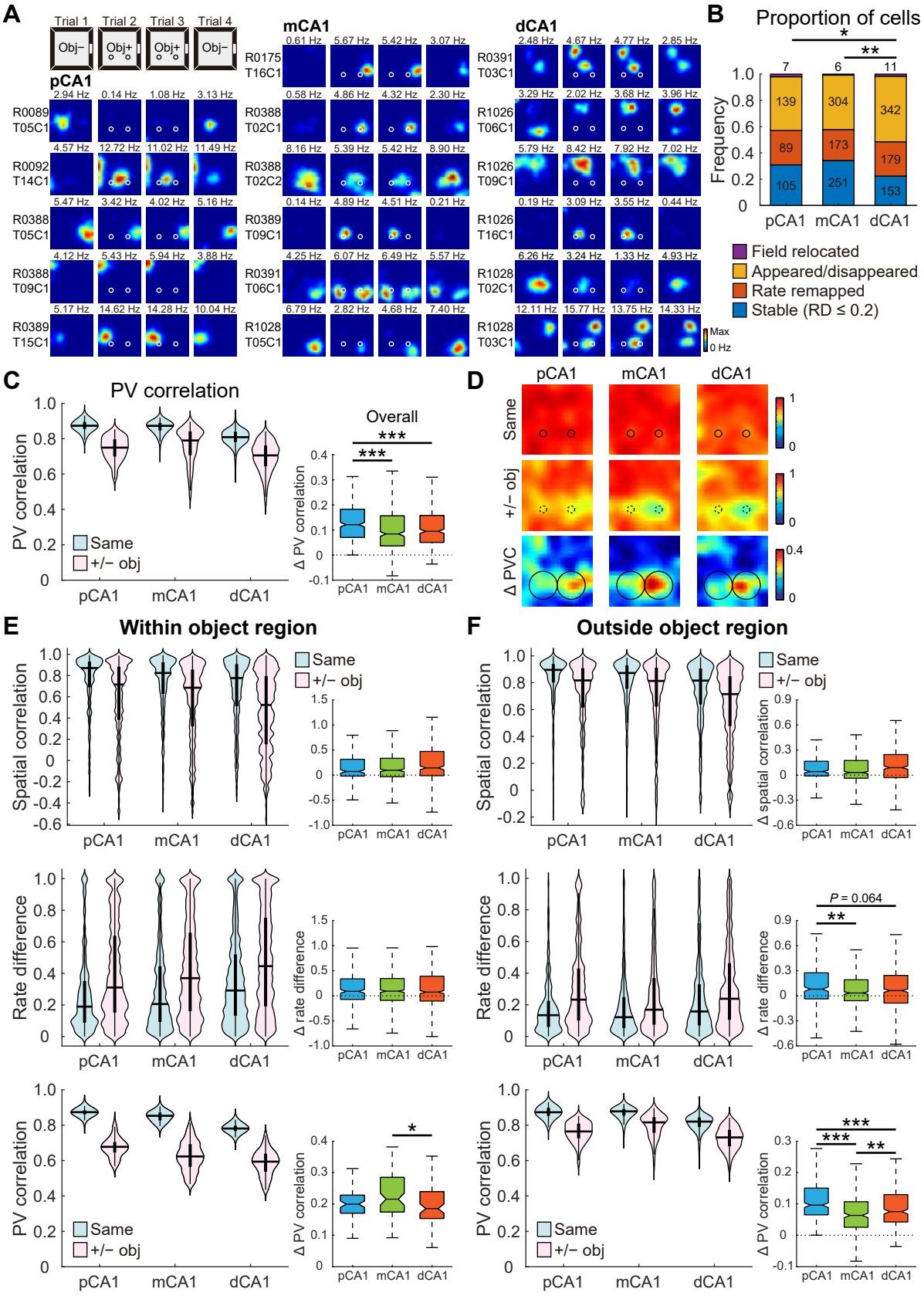
A
Trial 1
Trial 2
Trial 3
Trial 4
Obj−
Obj+
Obj+
Obj−
pCA1
mCA1
dCA1
R0089 T05C1
R0092 T14C1
R0388 T05C1
R0388 T09C1
R0389 T15C1
R0175 T16C1
R0388 T02C1
R0388 T02C2
R0389 T09C1
R0391 T06C1
R1028 T05C1
R0391 T03C1
R1026 T06C1
R1026 T09C1
R1026 T16C1
R1028 T02C1
R1028 T03C1
Max
0 Hz
B
Proportion of cells
Frequency
Field relocated
Appeared/disappeared
Rate remapped
Stable (RD ≤ 0.2)
C
PV correlation
Overall
Same
+/− obj
Δ PV correlation
D
Same
+/− obj
Δ PVC
E
Within object region
Spatial correlation
Rate difference
PV correlation
Δ spatial correlation
Δ rate difference
F
Outside object region
P = 0.064

Figure 5

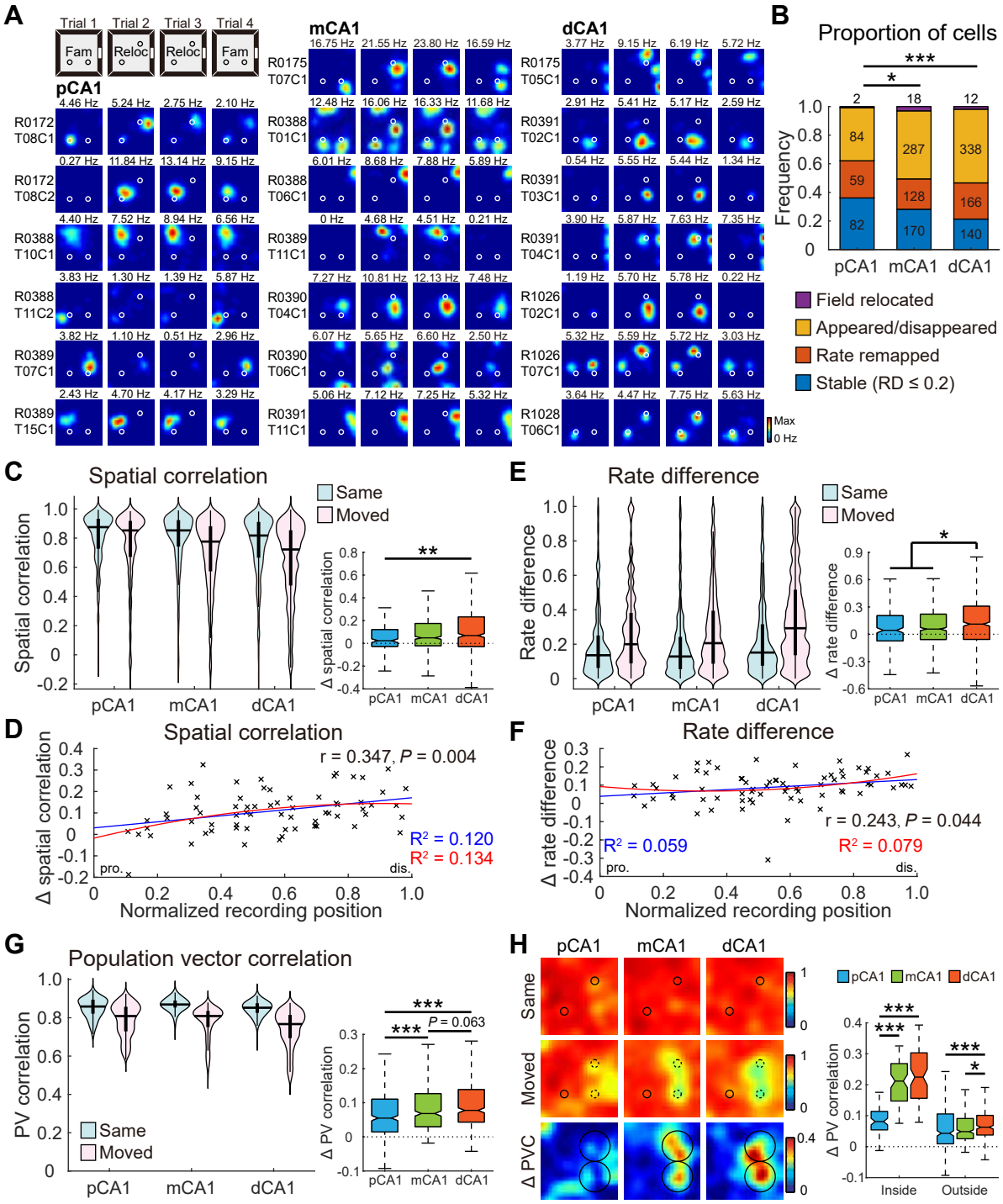
A
Trial 1
Trial 2
Trial 3
Trial 4
Fam
Reloc
Reloc
Fam
pCA1
mCA1
dCA1
R0172 T08C1
R0172 T08C2
R0388 T10C1
R0388 T11C2
R0389 T07C1
R0389 T15C1
R0175 T07C1
R0388 T01C1
R0388 T06C1
R0389 T11C1
R0390 T04C1
R0390 T06C1
R0391 T11C1
R0175 T05C1
R0391 T02C1
R0391 T03C1
R0391 T04C1
R1026 T02C1
R1026 T07C1
R1028 T06C1
Max
0 Hz
B
Proportion of cells
Frequency
Field relocated
Appeared/disappeared
Rate remapped
Stable (RD ≤ 0.2)
C
Spatial correlation
Same
Moved
Δ spatial correlation
D
r = 0.347, P = 0.004
R² = 0.120
R² = 0.134
pro.
dis.
Normalized recording position
E
Rate difference
Δ rate difference
F
r = 0.243, P = 0.044
R² = 0.059
R² = 0.079
G
Population vector correlation
PV correlation
Δ PV correlation
P = 0.063
H
Δ PVC
Inside
Outside

Figure 6

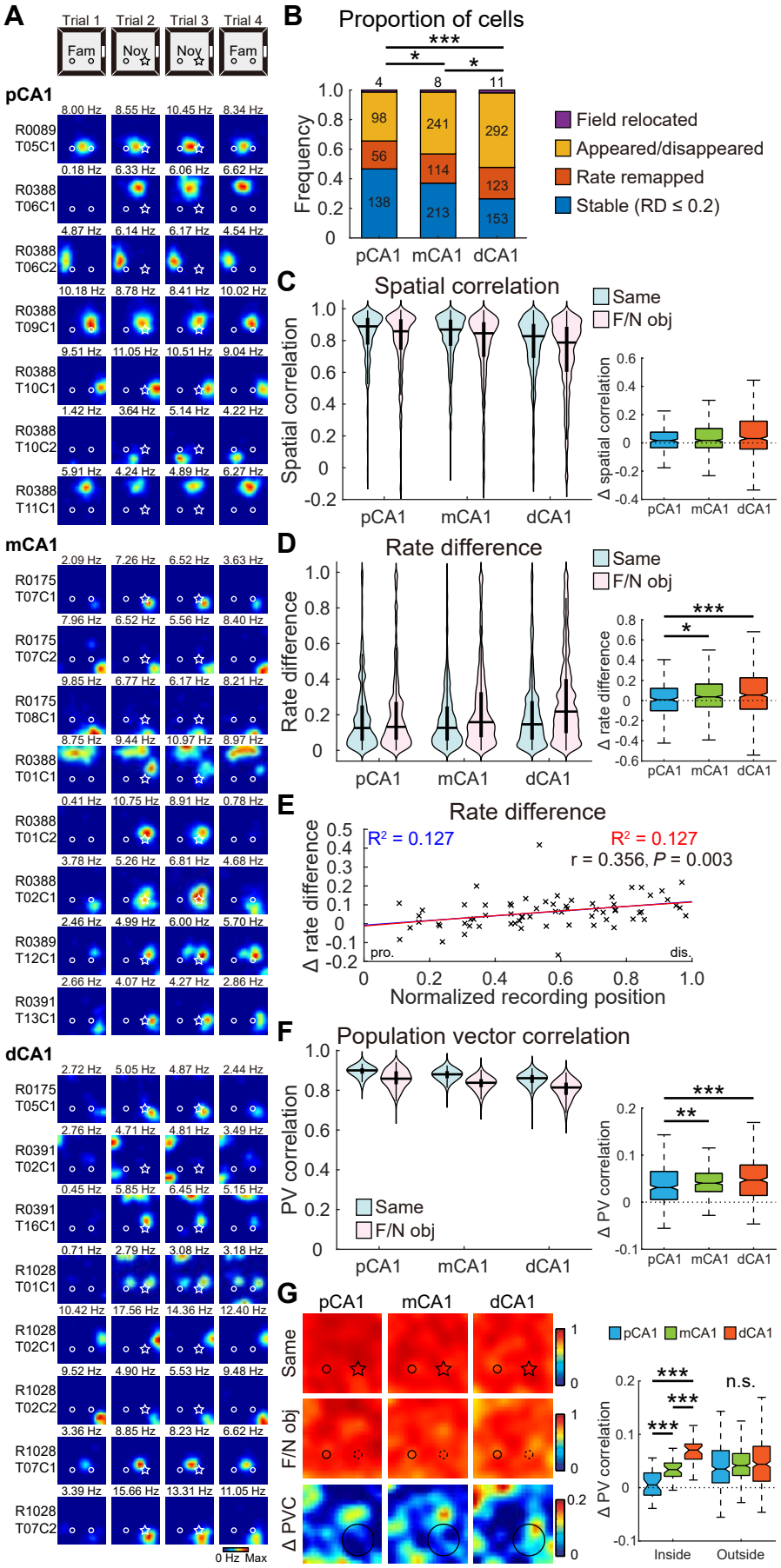
A
Trial 1
Trial 2
Trial 3
Trial 4
Fam
Nov
Nov
Fam
pCA1
mCA1
dCA1
0 Hz Max
B
Proportion of cells
Frequency
Field relocated
Appeared/disappeared
Rate remapped
Stable (RD ≤ 0.2)
pCA1 mCA1 dCA1
C
Spatial correlation
Same
F/N obj
Spatial correlation
Δ spatial correlation
D
Rate difference
Rate difference
Δ rate difference
E
Rate difference
R² = 0.127
R² = 0.127
r = 0.356, P = 0.003
Δ rate difference
pro.
dis.
Normalized recording position
F
Population vector correlation
PV correlation
Δ PV correlation
G
Same
F/N obj
Δ PVC
Δ PV correlation
Inside
Outside
n.s.

Supplementary Figure 1

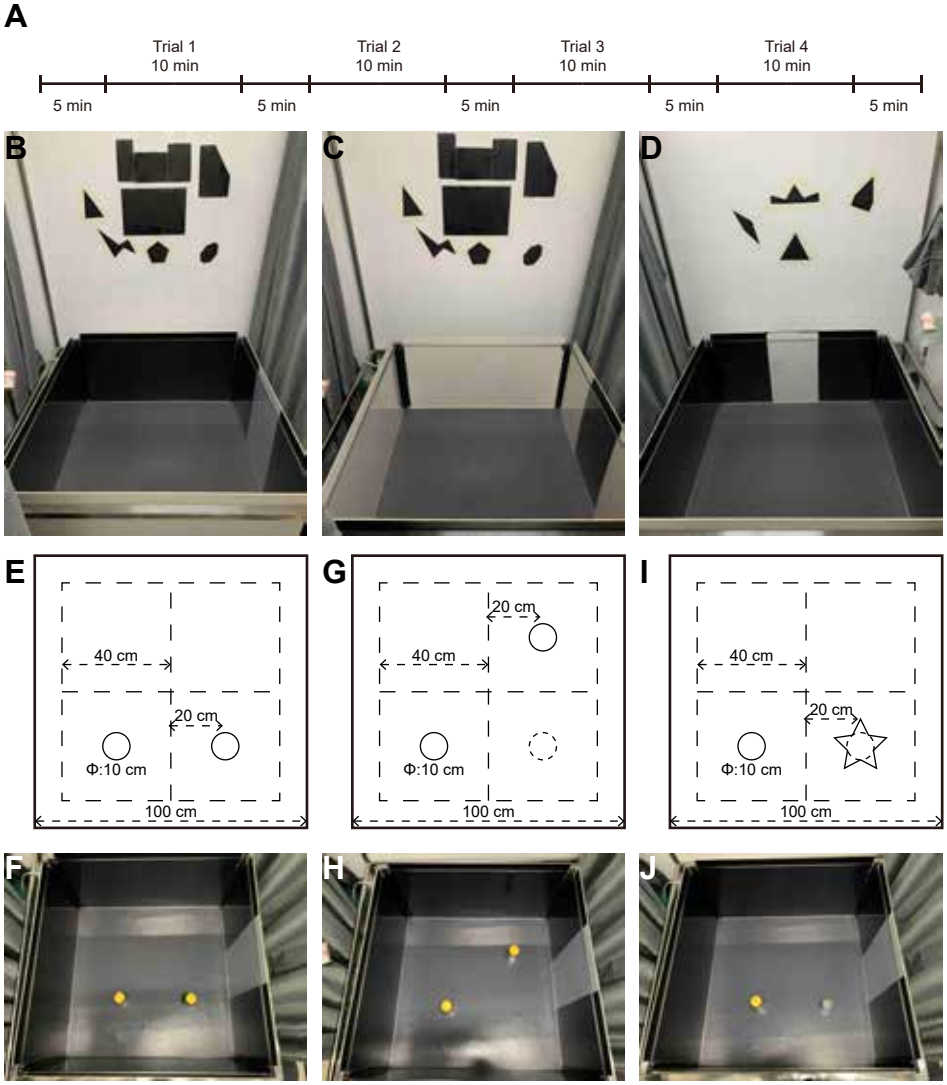

Supplementary Figure 2-1

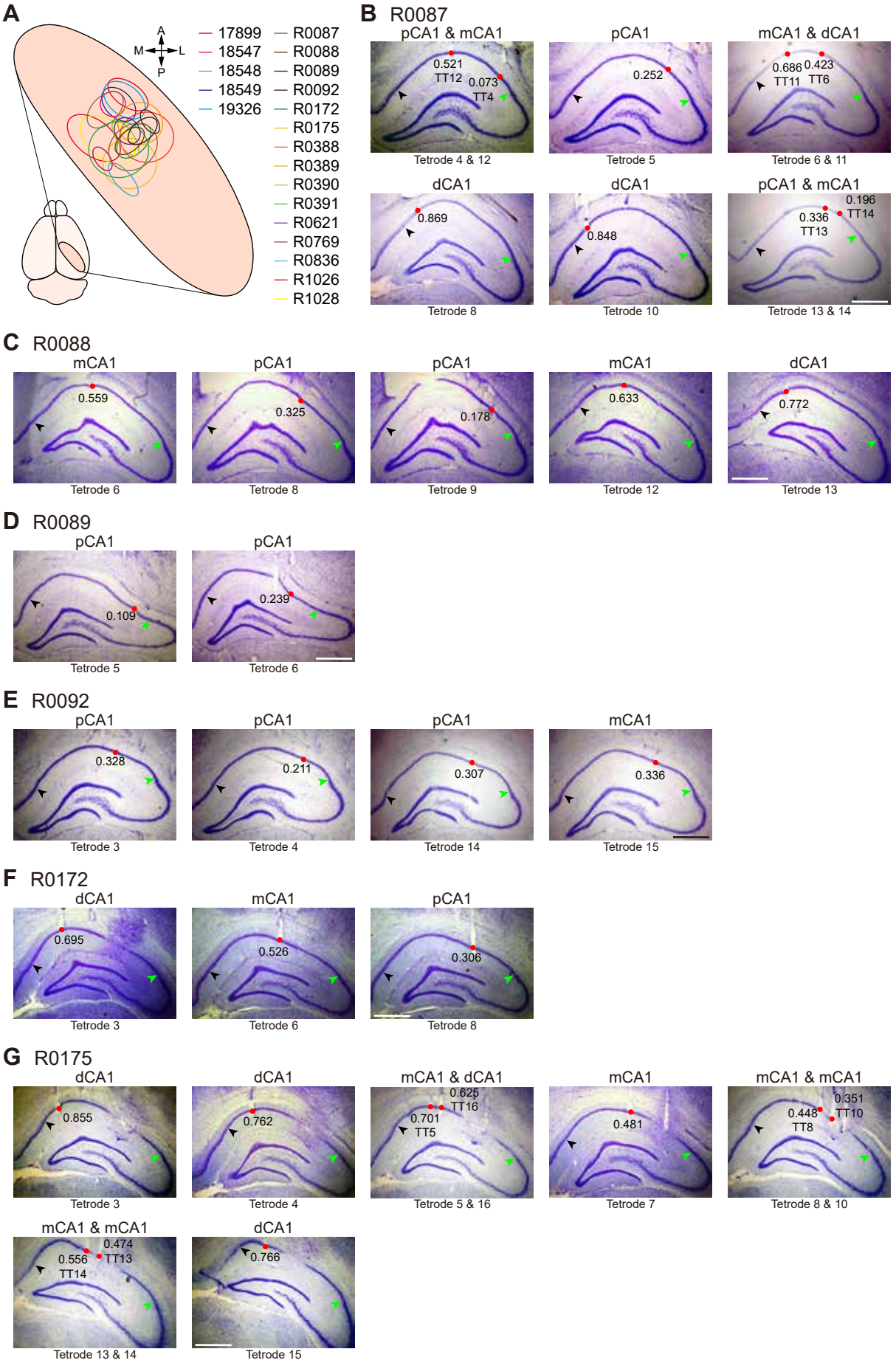

Supplementary Figure 2-2

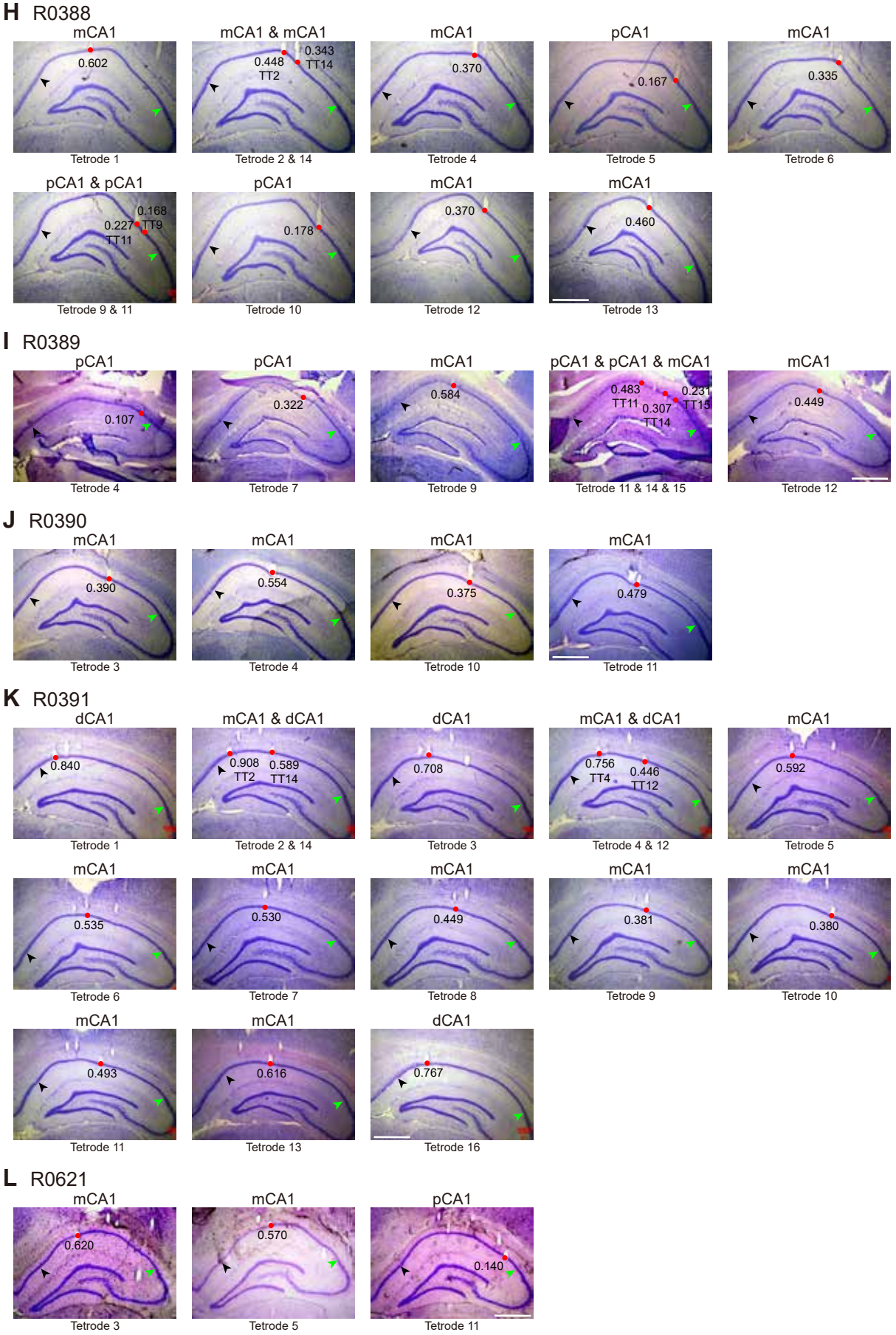

Supplementary Figure 2-3

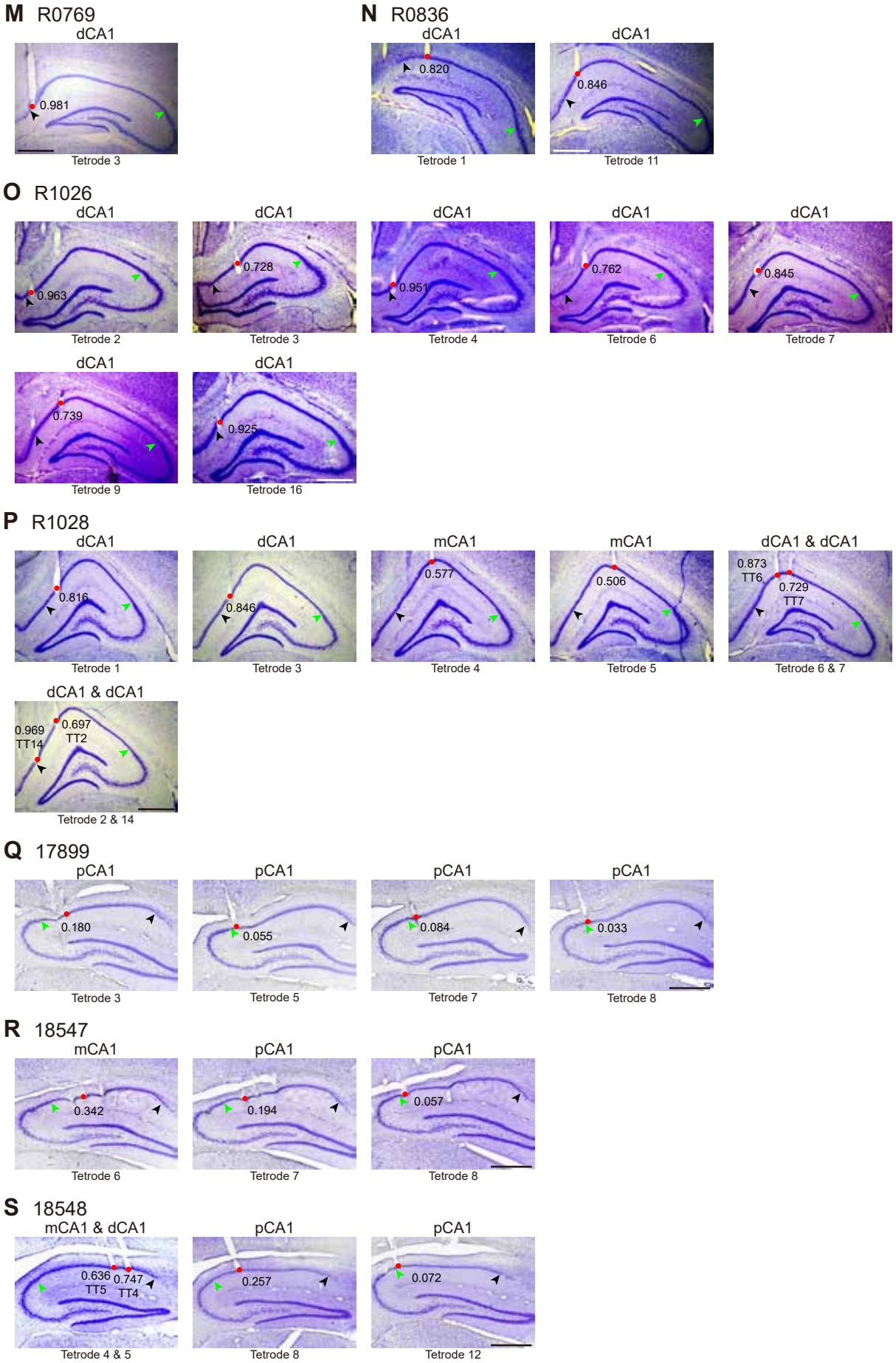

Supplementary Figure 2-4

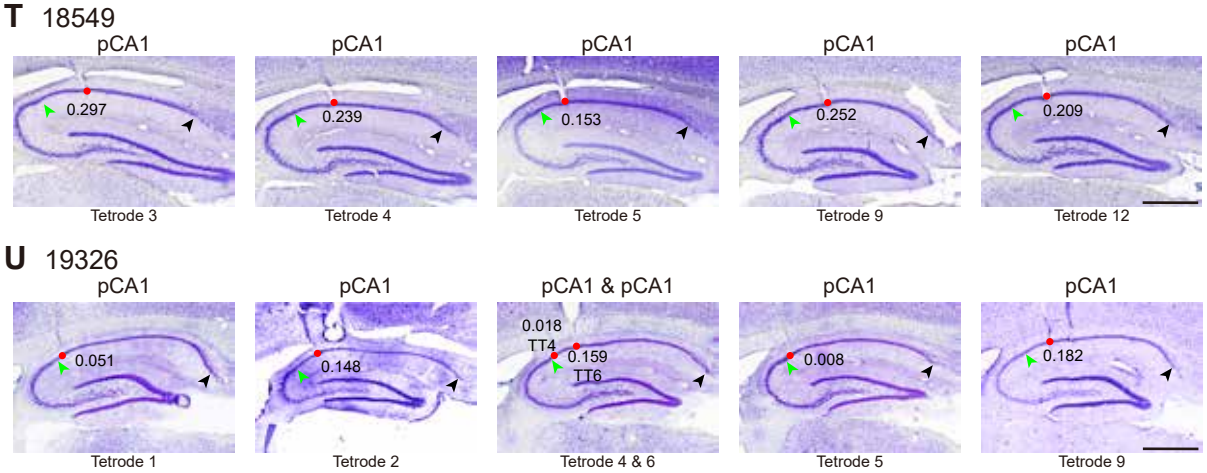

Supplementary Figure 3-1

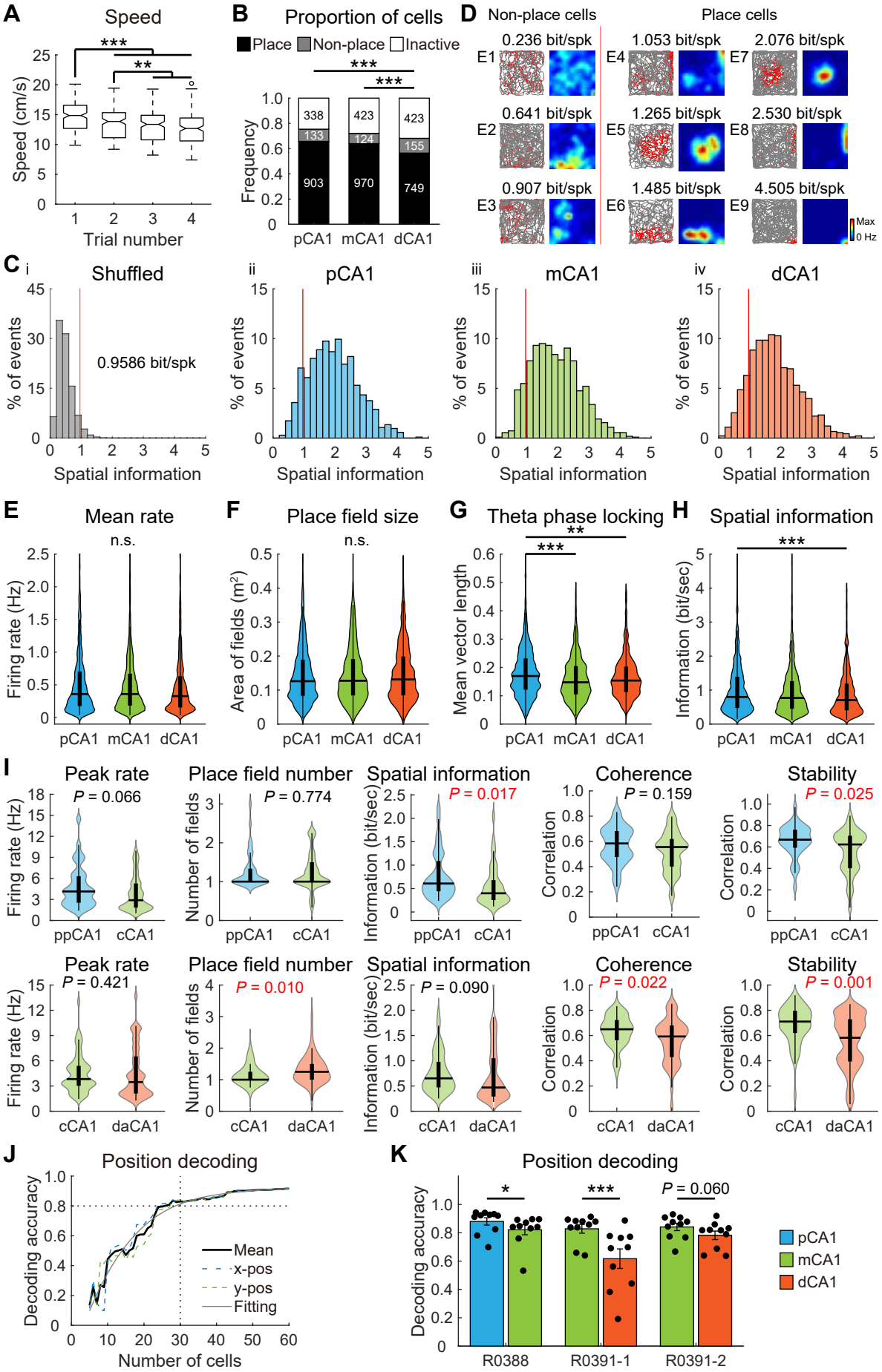

Supplementary Figure 3-2

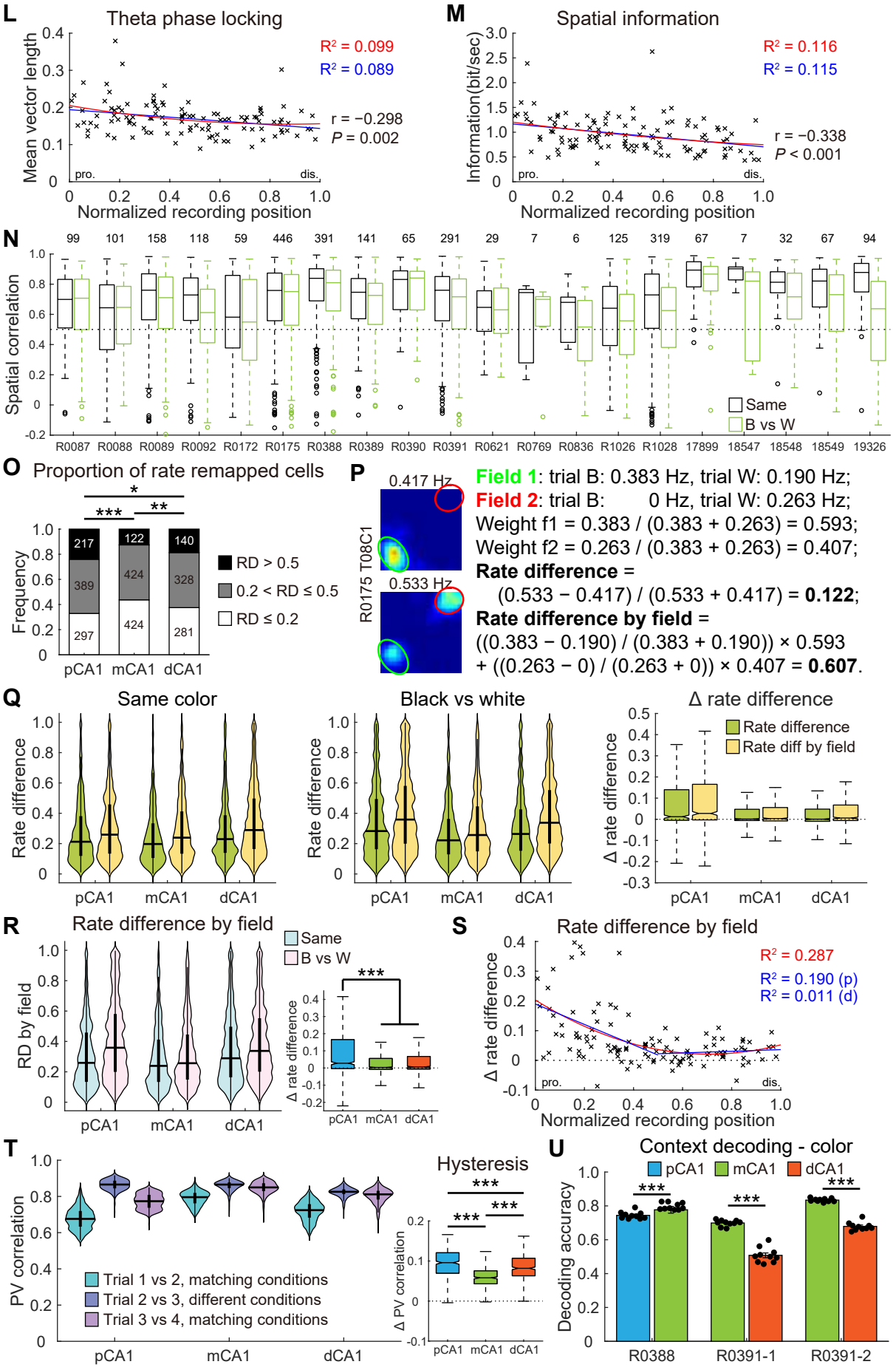

Supplementary Figure 4-1

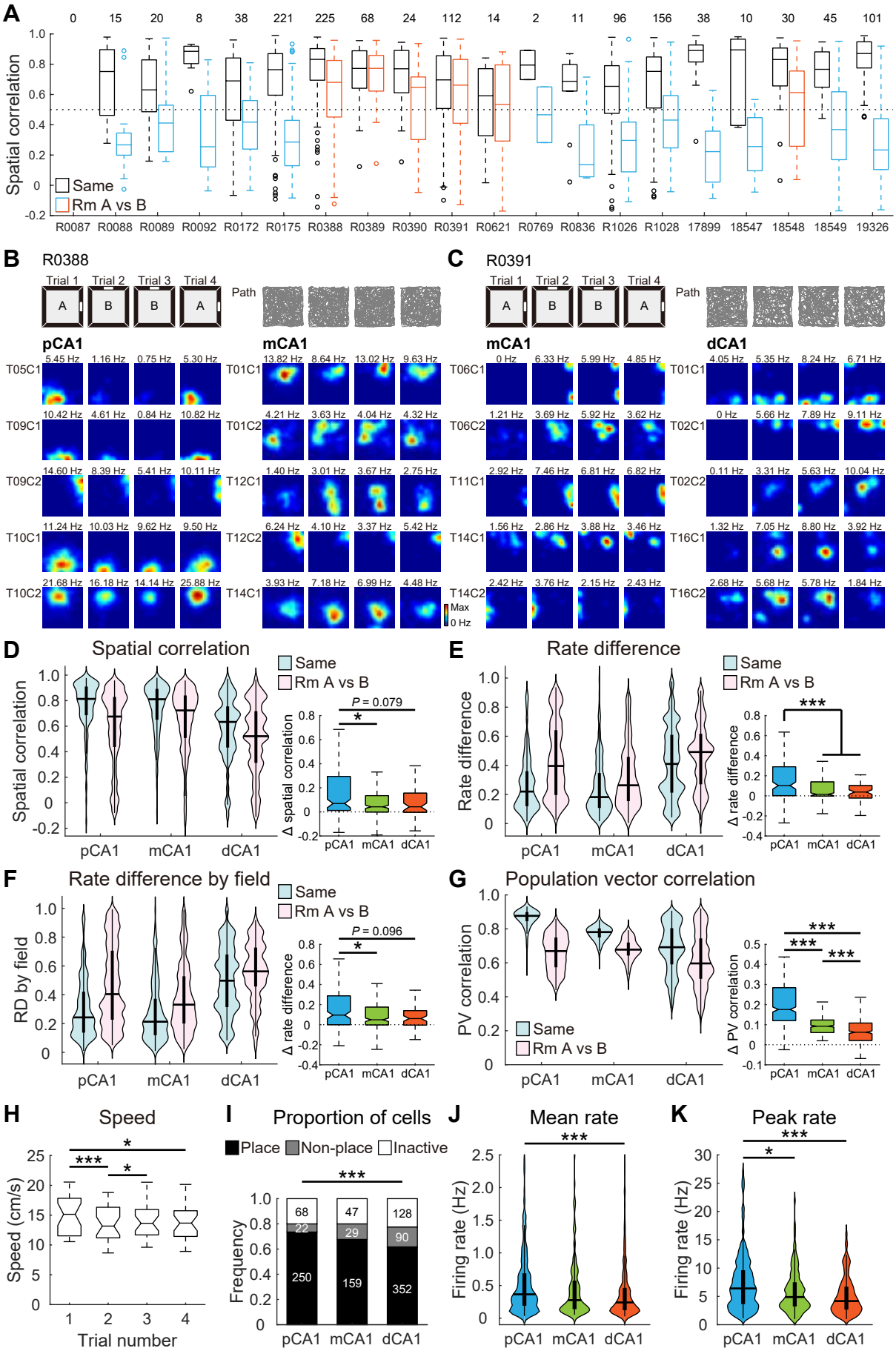

Supplementary Figure 4-2

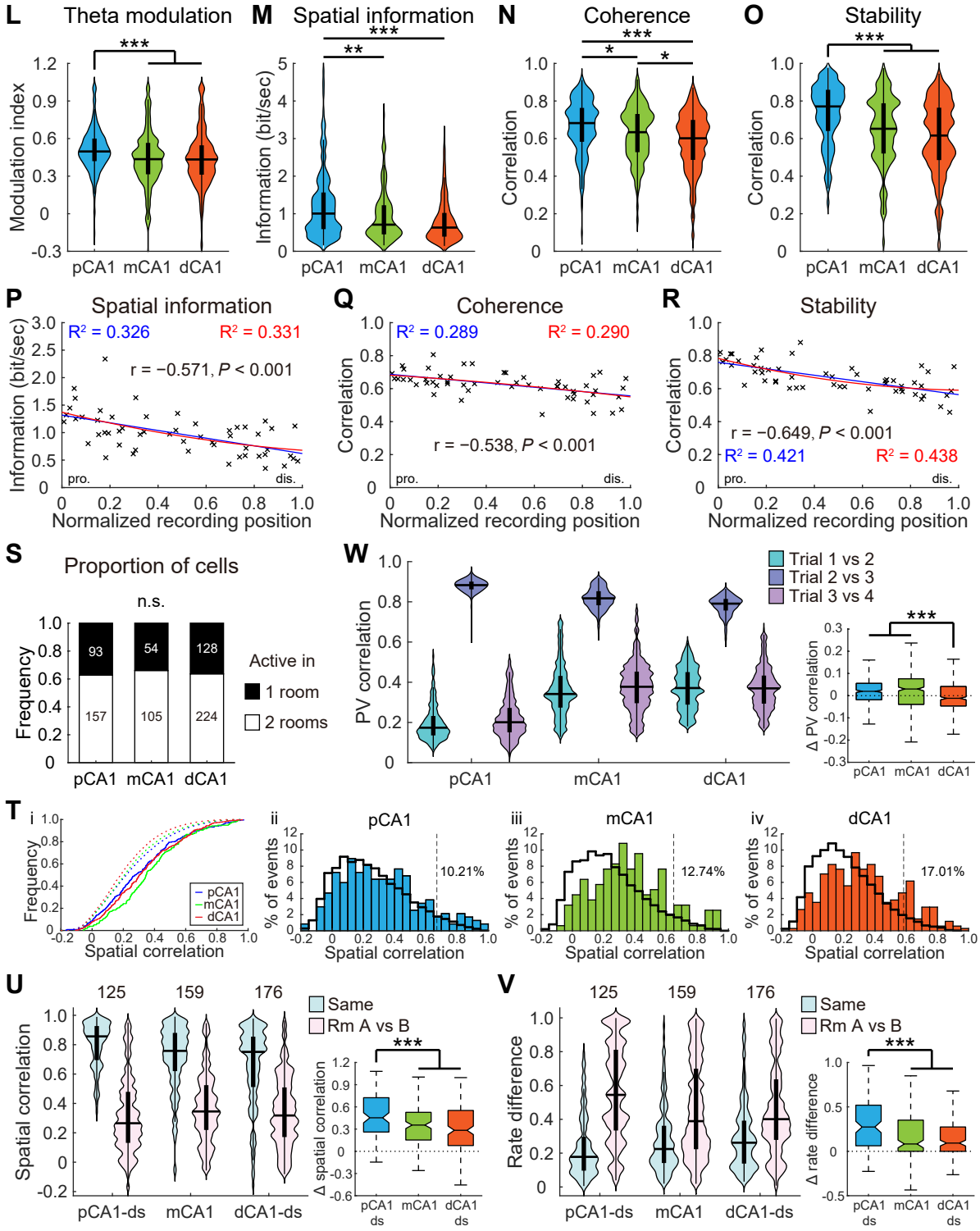

Supplementary Figure 5

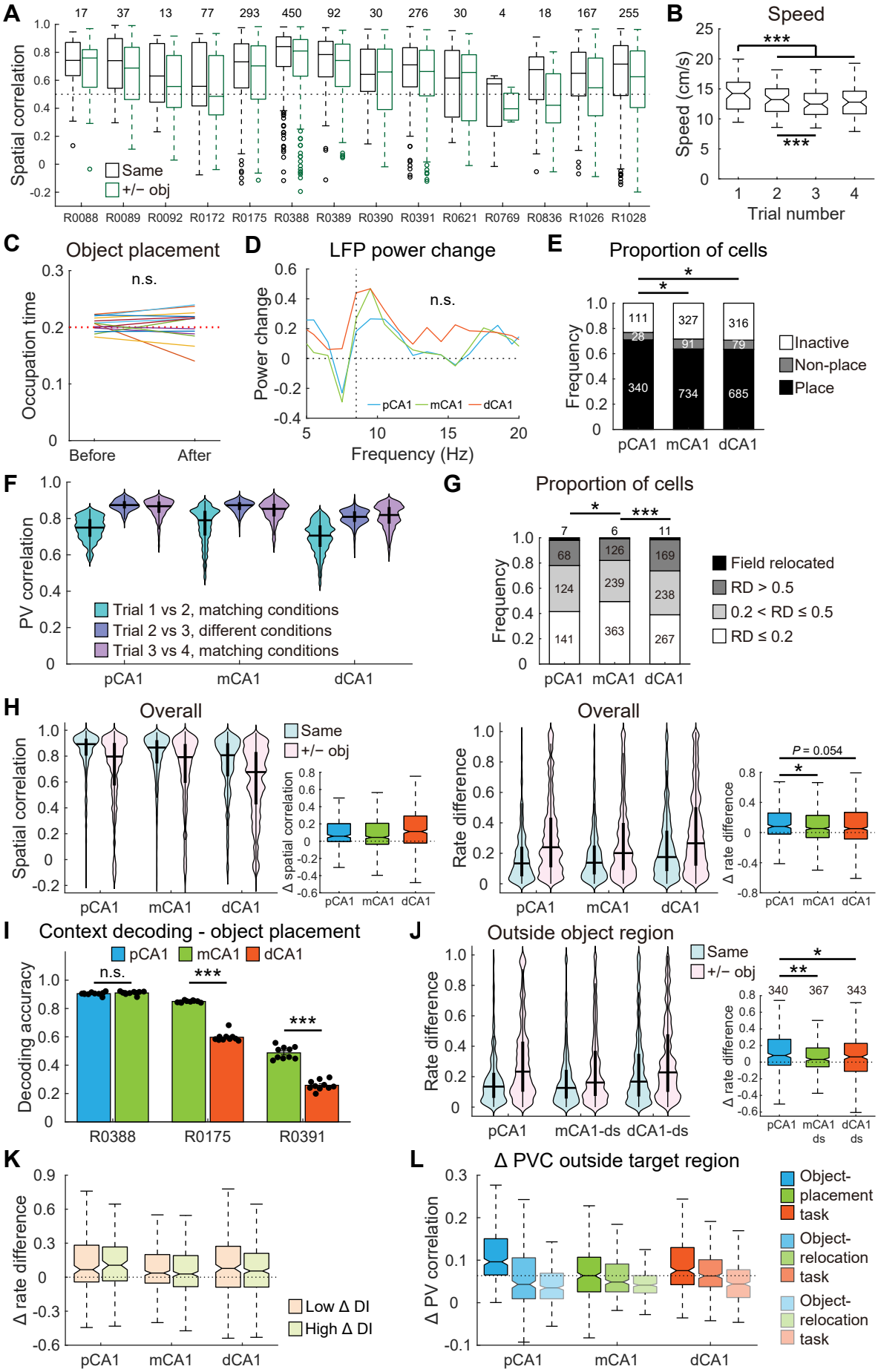

Supplementary Figure 6

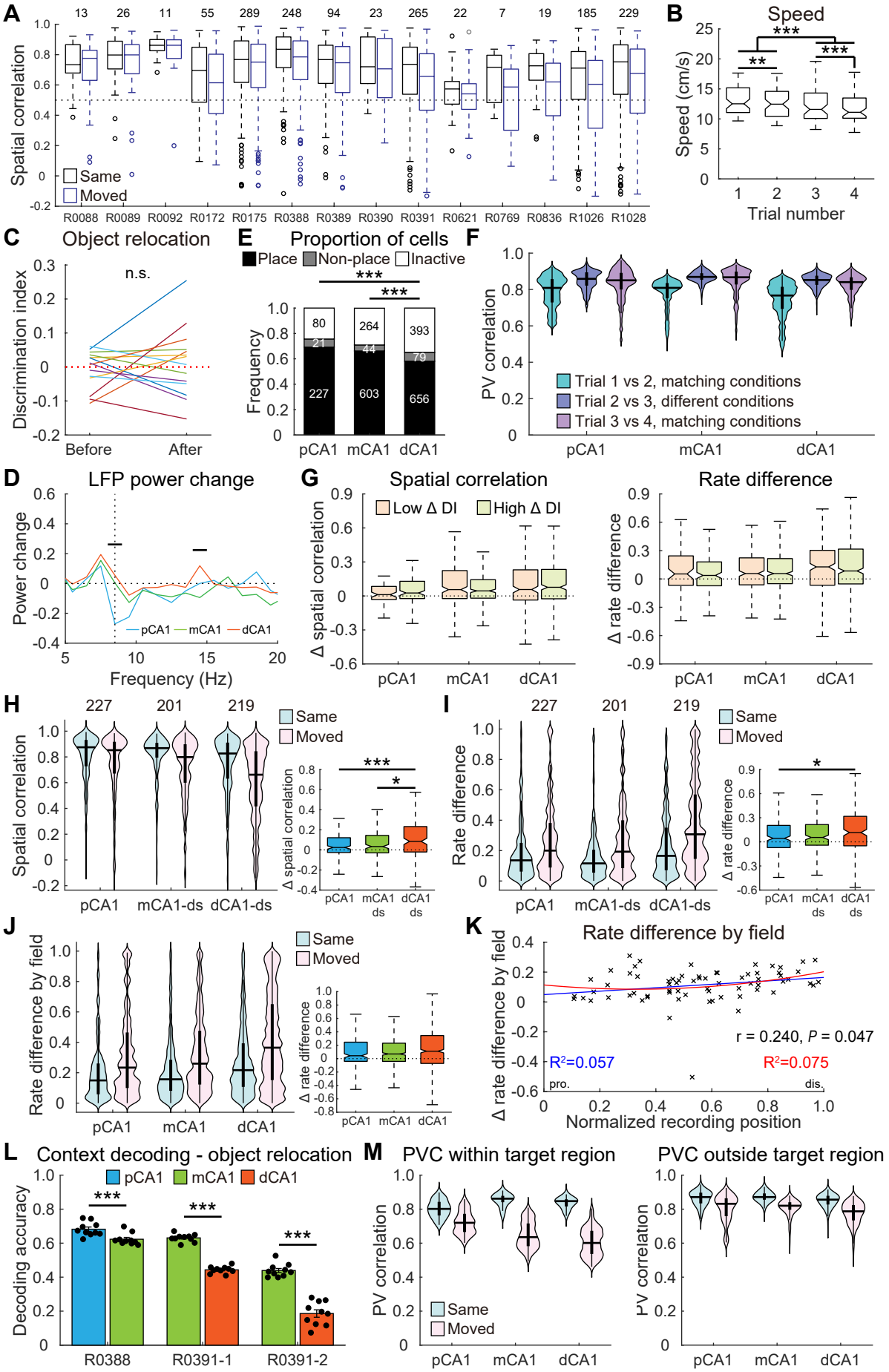

Supplementary Figure 7

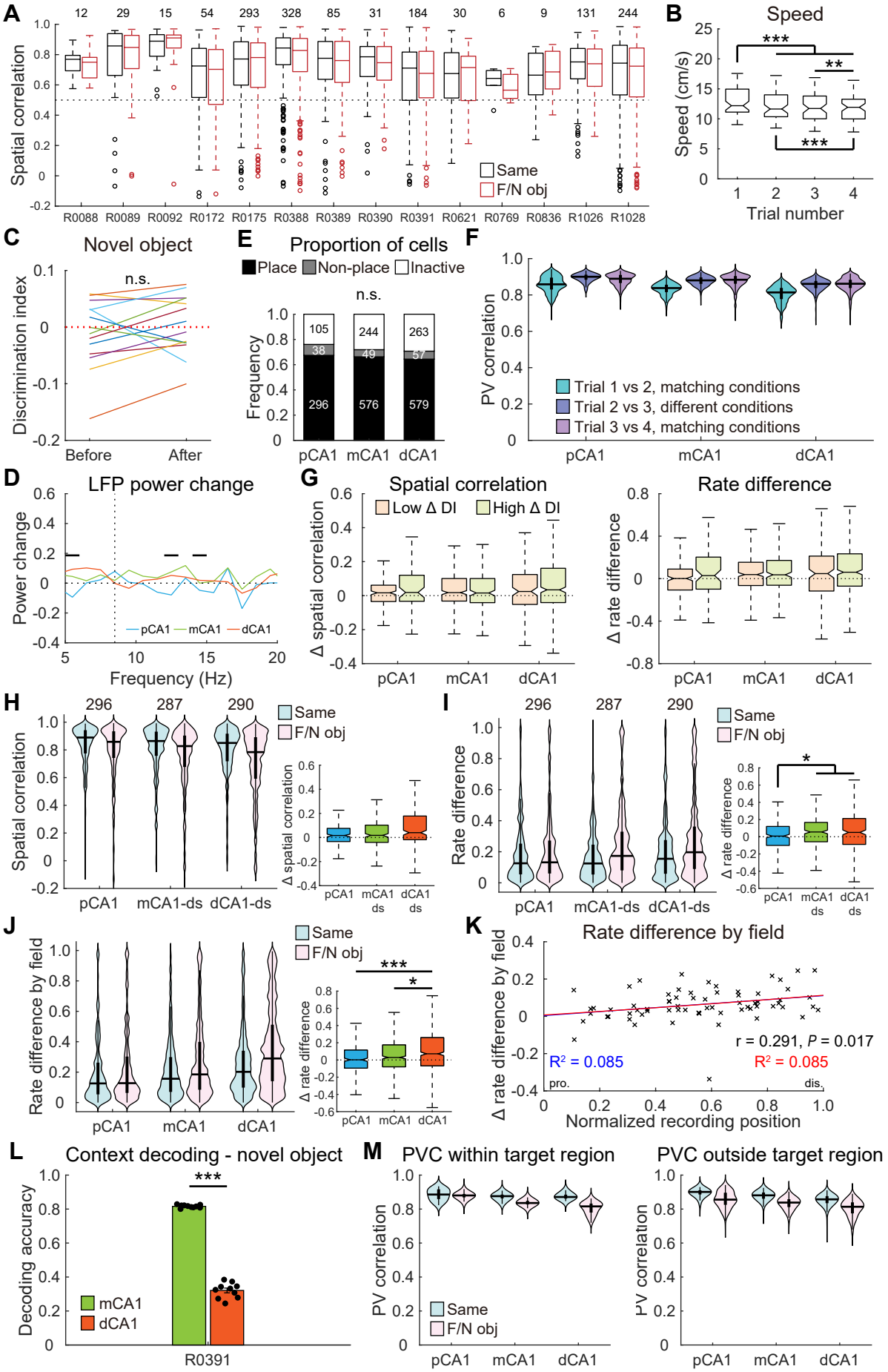

Supplementary Figure 8

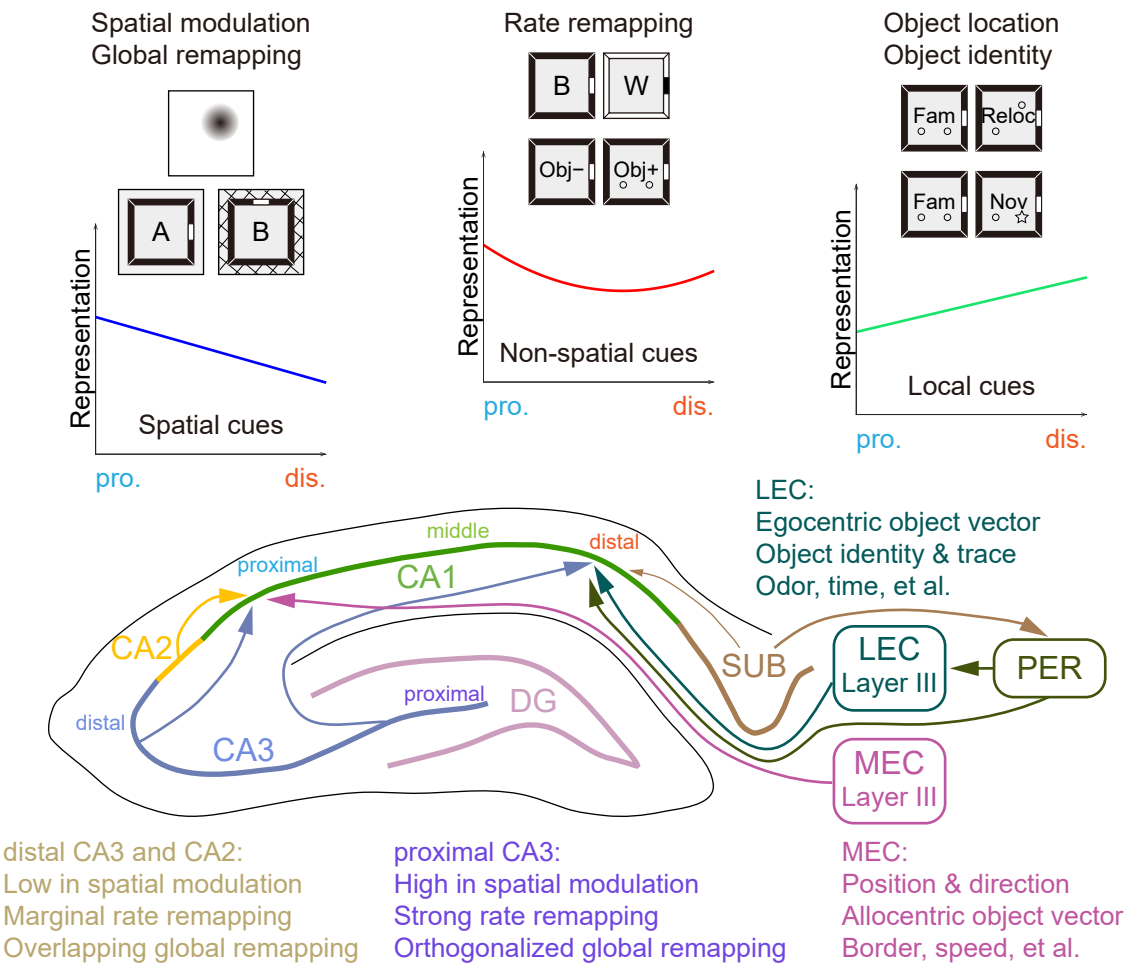

distal CA3 and CA2:
Low in spatial modulation
Marginal rate remapping
Overlapping global remapping

proximal CA3:
High in spatial modulation
Strong rate remapping
Orthogonalized global remapping

MEC:
Position & direction
Allocentric object vector
Border, speed, et al.